#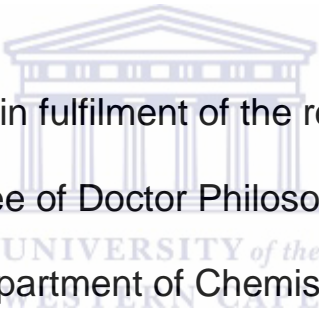 Development of Membrane Electrode Assemblies Based on Electrophoretic Deposition for High Temperature Polymer Electrolyte Membrane Fuel Cell Applications

by

Cecil Felix

A thesis submitted in fulfilment of the requirements for the

degree of Doctor Philosophiae

Department of Chemistry,

University of the Western Cape

Supervisor: Dr Sivakumar Pasupathi

Co supervisor: Prof Andriy Yaroshchuk

November 2013

Student number: 2363520

Declaration

I declare that "***Development of membrane electrode assemblies based on electrophoretic deposition for high temperature polymer electrolyte membrane fuel cell applications***" is my own work and that it has not been submitted for any degree or examination in any other university and that all the sources that I have used or quoted have been indicated and acknowledged by complete references.

Cecil Felix   November, 2013

Signed……………………………….

Acknowledgements

- ➢ I firstly thank God Almighty for His love and grace that I have experienced and for being the driving force in my life.

- ➢ Special thanks to my wife, Jolene, for her love, patience and support throughout the duration of this study.

- ➢ Special thanks to my parents who have given me so much and always supported me in my undertakings.

- ➢ I am thankful to Prof. Vladimir Linkov, director of the South African Institute for Advanced Materials Chemistry (SAIAMC) for affording me the opportunity to pursue my PhD studies.

- ➢ I am very thankful to Prof. Bruno G. Pollet, director of the Hydrogen South Africa (HySA) Systems Competence Centre (South Africa) for his support, guidance and motivation throughout the duration of this study.

- ➢ Special thanks to Dr. Sivakumar Pasupathi, a key program manager at HySA Systems Competence Centre (South Africa) for his supervision, support and motivation throughout the duration of this study. Dr. Sivakumar Pasupathi's expertise in HT-PEMFCs played a vital role in the fuel cell studies.

- ➢ Special thanks to Prof. Andriy Yaroshchuk (Polytechnic University of Catalonia, Spain) for his supervision and assistance throughout this project. Prof. Andriy Yaroshchuk's expert advice on colloidal science is very much appreciated. His expertise in colloidal science was vital to the modelling work done in this study.

- ➢ Special thanks to Dr. Emiliy Zholkovskyy and Dr. Mykola Bondarenko, both senior scientists at the Institute of Bio-Colloid Chemistry of the Ukranian Academy of

UNIVERSITY *of the*
WESTERN CAPE

Abstract

High Temperature Polymer Electrolyte Membrane Fuel Cells (HT-PEMFC) have received renewed interest in recent years due to its inherent advantages associated with the limitations faced by Low Temperature Polymer Electrolyte Membrane Fuel Cells (LT-PEMFC). The high *Pt* loadings required for PEMFCs have significantly hindered its commercialisation. Electrophoretic Deposition (EPD) is a promising route to reduce the noble metal loading. EPD is a method in which charged colloidal particles are deposited onto a target substrate under the force of an externally applied electric field. To effectively study the EPD method, the methodology of this study was divided into two parts: (i) the EPD method was studied *via* known empirical methods to fabricate, test and characterise MEAs suitable for HT-PEMFCs. The feasibility of the EPD method was determined by comparing the performance of the fabricated EPD MEAs to MEAs fabricated *via* spraying methods, and (ii) due to the promising results obtained in part (i) of the methodology, a theoretical model was developed to obtain a deep understanding about nature of the interactions between the *Pt/C* particles in a colloidal suspension. The theoretical model will serve as a foundation for future studies.

In part (i) of the methodology, the *Pt/C* particles were studied in organic solutions (i.e. Isopropyl Alcohol, IPA) *via* the Zetasizer Nano ZS instrument under various salt (*NaCl*) concentrations and pH conditions while introducing polymeric surfactants, i.e. Nafion® ionomer and Polytetrafluoroethylene (PTFE) to the suspension. The optimum catalyst suspensions were selected to fabricate GDEs *via* the EPD method. Physical characterisations revealed that the EPD GDEs exhibited cracked morphology with high porosity. Electrochemical characterisations revealed that the EPD MEA showed significantly better performance (i.e. 73% higher peak power) compared to the hand

sprayed MEA due to lower charge transfer and mass transport resistance at high current densities. Compared to the ultrasonically sprayed MEA, the EPD MEA exhibited a peak power increase of ~12% at a slightly lower *Pt* loading (i.e. ~4 wt%). A comparative study between the Nafion® ionomer and PTFE in the CLs of two EPD MEAs revealed superior performance for the EPD MEA with the PTFE in the CLs.

Part (ii) of the methodology deals with the electrical interfacial properties of the aqueous *Pt/C* suspension. The study consists of two sets of measurements (i.e. electrophoretic and coagulation dynamic studies) conducted for different electrolyte compositions. A theoretical background on determining the interfacial potential and charge from electrophoretic and coagulation dynamic measurements are provided. Detailed statements of the Standard Electrokinetic and Derjaguin, Landau, Vervey and Overbeek Models are given in the forms that are capable of addressing electrophoresis and the interaction of particles for an arbitrary ratio of the particle to Debye radius, interfacial potential and electrolyte composition. The obtained experimental data were processed by using numerical algorithms based on the formulated models for obtaining the interfacial potential and charge. While analysing the dependencies of interfacial potential and charge on the electrolyte compositions charge, conclusions were made regarding the mechanisms of charge formation. It was established that the behaviour of system stability is in qualitative agreement with the results computed from the electrophoretic data. The verification of quantitative applicability of the employed models was conducted by calculating the Hamaker constant from the experimental data. It was proposed how to explain the observed variations of the predicted Hamaker constant and its unusually high value.

List of figures

x

List of tables

List of abbreviations

PEMFC	Polymer Electrolyte Membrane Fuel Cell
LT-PEMFC	Low Temperature Polymer Electrolyte Membrane Fuel Cell
HT-PEMFC	High Temperature Polymer Electrolyte Membrane Fuel cell
EPD	Electrophoretic Deposition
MEA	Membrane Electrode Assembly
GDE	Gas Diffusion Electrode
GDL	Gas Diffusion Layer
CL	Catalyst Layer
PALS	Phase Analysis Light Scattering
DLS	Dynamic Light Scattering
LDV	Laser Doppler Velocimetry
CV	Cyclic Voltammetry
EIS	Electrochemical Impedance Spectroscopy
TPB	Triple Phase Boundary
HOR	Hydrogen Oxidation Reaction
ORR	Oxygen Reduction Reaction
PEM	Polymer Electrolyte Membrane
HR-SEM	High resolution Scanning Electron Microscopy
MIP	Mercury Intrusion Porosity
ECSA	Electrochemical Surface Area
HS	Hand Spray
UP	Ultra Pure
PA	Phosphoric Acid
CCC	Critical Coagulation Concentration

DLVO   Derjaguin, Landau, Verwey and Overbeek

EDL   Electrical Double Layer

SLC   Stagnant Layer Conductivity

List of symbols

E^0 Standard potential

i_0 Exchange current density

ΔG_f^0 Standard Gibbs free energy

ε Dielectric constant

ε_0 Permittivity of vacuum

ζ Electric potential at the interface in equilibrium state (zeta potential

E Electric field strength

η Viscosity

a Mean particle radius

τ Coagulation time

U_{eph} Electrophoretic velocity

ζ_{exp} Measured zeta potential

q Interfacial charge density

Du Dukhin number

F Faraday constant

R Gas constant

T Absolute temperature

κ Debye parameter (inverse Debye length)

c Concentration

Ψ Equilibrium electric potential

$\Psi(r)$ Electric potential special distribution

Φ Local electric potential

p Pressure

S Surface

u	Velocity
χ	Electrophoretic mobility
H	Hamaker constant
X(*h*)	Interaction force
σ	Stress tensor
Π	Effective pressure
τ_{Sm}	Smoluchowski time scale parameter
θ	Spherical polar coordinate
$M_k(r)$	Function describing radial dependency of perturbation of *k*th ion electrochemical potential
Ψ	$= \Psi F/RT$ - normalized equilibrium electric potential
μ_k	The *k*th ion electrochemical potential
η	Viscosity
G_{el}	Electrostatic free energy
$G_w(h)$	Van Der Waals free energy
H	Minimum distance between particle surfaces
r	Vector coordinate
r	Polar radius in the spherical coordinate system
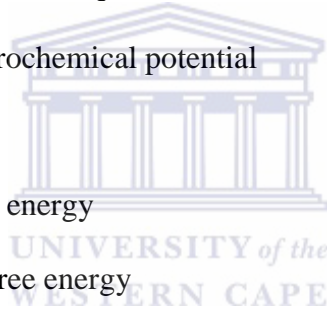
Table of contents

Contents

Chapter 1: Introduction

1.1 PEMFC overview

Fuel cell technology is expected to become a key technology in the 21st century because of the high power densities that it can achieve [1]. Research into fuel cell technology has gained significant attention due to energy shortages and environmental pollution being major global concerns [2]. Fuel cells are suitable for both stationary applications (such as block power stations and residential cogeneration power systems) as well as mobile applications which include all types of transportation (e.g. cars, buses, trucks and trains) and portable electronic devices (e.g. cellular phones and electronic notebooks) [3, 4].

Polymer Electrolyte Membrane Fuel Cells (PEMFCs) are especially important due to its high power densities, rapid start up, low operating temperatures and low greenhouse gas emissions [4-7]. Current experimental results and practical applications of PEMFCs revealed that these fuel cells performed best when very pure H_2 is used as an anode input gas [8]. Currently H_2 is mainly produced by reformation of hydrocarbon feed stocks. The reformate gas obtained from the reformer after partial oxidation contains ~3.0 vol% CO which is reduced to ~0.5 to 1 vol% by the water gas shift reaction [9] which is still too high for PEMFCs operating at low temperatures. Furthermore the Nafion® membrane cannot be operated at temperatures above 90°C (or typically 80°C) due to the dehydration and loss of proton conductivity of the membrane. A maximum temperature of 90°C is a serious impediment for the commercialisation of PEMFCs. Operating at 90°C leads to difficulty in heat rejection for automobile applications and easy poisoning of the Pt active sites by CO

adsorption which is present in the hydrogen fuel at concentration levels above 10 ppm [10-12]. Hence there is a need for pure H_2 which adds additional purification steps which add to the production cost of PEMFCs. These limitations can be overcome by operating fuel cells at temperatures above 90°C. At higher temperatures faster reaction rates are achieved, generated water is easily removed and the CO poisoning of the Pt catalyst is decreased [13-15]. Other advantages include reduced system weight, volume and complexity which results in an increased power density, specific power and functionality through system and component simplification [16]. In theory High Temperature (HT) PEMFCs have the potential to solve the inherent problems associated with Low Temperature (LT) PEMFCs. In practice however operating at an increased temperature (100 to 200°C) causes greater challenges for PEMFCs. Novel materials that have high performance and durability under these conditions are a prerequisite for HT-PEMFCs. Most importantly is an alternative electrolyte membrane that can operate at 100 to 200°C and low relative humidity (25 to 50%) [17]. From a thermodynamic analysis it is known that the adsorption of CO onto Pt is associated with negative entropy which indicates that adsorption is strongly favoured at low temperatures and not favoured at high temperatures [18]. In HT-PEMFCs, CO tolerance is dramatically increased (up to 30, 000 ppm at 200°C) [19] allowing HT-PEMFCs to use lower quality (i.e. high CO concentrations) reformed H_2 [3].

The Membrane Electrode Assembly (MEA) is core of the PEMFC and typically consists of the Polymer Electrolyte Membrane (PEM), Catalyst Layer (CL) and the Gas Diffusion Layers (GDL) [20]. Common methods of fabricating these MEAs include spraying the CL onto the GDL (known as Catalyst Coated Substrate, CCS) or spraying the CL directly onto the membrane (known as Catalyst Coated Membrane,

2

CCM) [21]. During the past few decades many efforts were made to decrease the noble metal catalyst loading. For LT-PEMFCs, it was reported that catalyst loadings can be decreased as low as 0.05 to 0.15 mg/cm^2 with fuel cell performances similar to that of higher catalyst loadings (i.e. 4 mg/cm) [1]. The performance of PEMFCs can be improved by increasing the overall catalyst utilisation per unit surface area of MEA to effectively make the gaseous fuel undergo desirable catalytic reaction [22]. The conventional spraying methods for MEA fabrication have reproducibility issues and result in high catalyst loadings.

1.2 Rationale of research

HT-PEMFCs offers a solution to the limitations faced by LT-PEMFCs however one of the main drawbacks of HT-PEMFCs is that it require significantly higher *Pt* loadings (i.e 0.6 to 1.2 mg/cm^2 *Pt* on each side) compared to LT-PEMFCs [23, 24]. The high cost of the *Pt* catalyst still imposes one of the most important hindrances for fuel cell commercialisation. Therefore it is important to minimise the amount of *Pt* required to lower the production cost of the fuel cell. The CL is a crucial component of PEMFCs as it contains the active catalyst material required for electrochemical reactions. The morphology of the CL can have a significant impact on the performance of the PEMFC therefore it is important to be able to control the micro-structure of the CL. A good dispersion of the active catalyst particles is also crucial to maximise *Pt* utilisation and reduce the overall requirement of the expensive noble metal catalyst. It is therefore necessary to identify a suitable fabrication method to form CLs that produces MEAs with high performance.

An ideal fabrication method should be reproducible, fast and up scaling should be possible [25] for it to be commercially viable. The fabrication method should also allow easy control of the micro-structure of the formed CL. Electrophoretic Deposition (EPD) is an electrochemical method attracting increasing interest for material processing [26]. During EPD, charged particles dispersed in a liquid are deposited onto a substrate under the force of an externally applied electric field. Advantages of EPD include short formation time, a simple and cost effective apparatus, little restriction on the shape of the substrate and can be easily modified for specific applications [27, 28]. After searching the open literature and to the best of our knowledge, the use of the EPD method to deposit CLs in MEAs are only reported for LT-PEMFCs [22, 29-32]. In these studies the researchers reported improvement in *Pt* utilisation and MEA performance. EPD is thus a promising route to deposit the CLs of MEAs suitable for HT-PEMFCs.
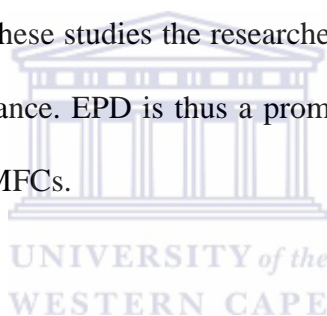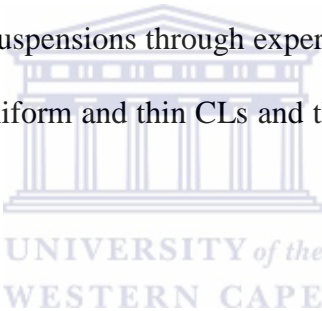
To optimise the design of the CL *via* EPD, it is essential to study and optimise the catalyst suspension (also called catalyst ink) from which the CL will be formed. For EPD, the catalyst suspension should be stable over the duration of EPD, i.e. the suspension should remain free from agglomerated catalyst particles. The catalyst particles should also have high surface potentials that facilitate rapid deposition under the force of the applied electric field. It is well known that the rate of electrophoresis of relatively "large" colloidal particles (defined as such whose size is much larger than the Debye screening length) can be described by the so-called Smoluchowski formula. In the case of nano-particles, the Smoluchowski formula is not applicable anymore, and the electrophoretic mobility becomes dependent, in particular, on the particle size and the solution ionic strength. It is therefore necessary to study the *Pt/C*

particles under conditions where the pH and solution ionic strength are controlled. From the experimentally obtained data, a theoretical model should be developed that can describe the nature of the interactions that occur between the particles in the suspension. No theoretical model on the stability behaviour of the *Pt/C* particles in a colloidal suspension is available in the open literature. A deep understanding about the nature of the catalyst particle interactions will facilitate obtaining optimally designed CLs that lead to high cell performance.

1.3 Objectives

The main objectives of this study were:

(i)   To optimise the catalyst suspensions through experimental and theoretical studies to develop MEAs with uniform and thin CLs and thereby maximise *Pt* utilisation and MEA performance.

(ii) To adapt the EPD method to fabricate Gas Diffusion Electrodes (GDE) and to test and characterise it under HT-PEMFC conditions. To determine the feasibility of the EPD method, the fabricated GDEs had to facilitate lower *Pt* loadings and/or yield MEAs with performances that were on par or better than MEAs fabricated by available spraying methods.

(iii) To develop a theoretical model that provides a deep understanding of the nature of interactions of the *Pt/C* particles in aqueous suspensions. The developed model should serve as a foundation for future studies based on a novel method where the *Pt/C* particles in aqueous solutions are deposited without the influence of an externally applied electric field.

5

Chapter 2: Literature survey

2.1 Fuel cell overview

2.1.1 Background

Fuel cells are electrochemical devices that directly convert chemical energy into electricity, water and heat with high efficiency and low environmental impact [33, 34]. Fuel cells operate similar to batteries but do not require any recharging and will operate continuously as long as a fuel and oxidant is supplied. This is a key advantage that fuel cells have over batteries since the power generation components are separated from the energy storage components of the system. If more power is required, a fuel cell module with a greater cell area is used and if more energy is required, more fuel storage can be supplied [35].
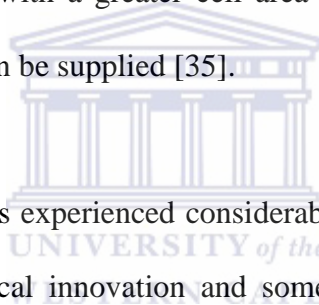
Fuel cells have in recent years experienced considerable growth in terms of research and development, technological innovation and some applications are almost at a commercial level (e.g. the automotive industry). Fuel cell technology is not new since the first working fuel cell was already built in 1839 by Sir William Grove. It is only in the past few decades that fuel cells found practical applications in the space and military sector [36, 37]. In the mid 1960's, research work was focused on the further development of various fuel cells for applications such as stationary power and transportation. The delay in the commercialisation of fuel cells is primarily due to technical and economic limitations. The fuels used in certain fuel cells (such as PEMFC) are H_2 or H_2 rich hydrocarbons which contain significant chemical energy compared to conventional battery materials. The efficiency of fuel cells can reach as high as 60 % in electrical energy generation and 80% in co-generation of electrical

and thermal energy with > 90% reduction in major pollutants [38]. High efficiencies can be achieved because unlike steam or gas turbines and internal combustion engines which are based on certain thermal cycles, the maximum efficiency of fuel cells are not limited by the Carnot cycle [35]. Fuel cells are also promising to provide energy in rural areas where access to the public grid is not possible due to the high cost involved with electrical wiring and equipment [39]. Today the main driving force for fuel cell research, development and commercialisation is the concerns about global pollution caused by the energy emissions from current technologies, especially transportation and stationary applications [40]. Fuel cells are already seen as an alternative to the internal combustion engine in automobile applications as well as alternatives to batteries in many portable electronic devices [41].

2.1.2 Operating principle of fuel cells

Fuels cells are galvanic cells in which the free energy of a chemical reaction is converted to electrical energy (i.e. electrical current). The Gibbs free energy change (*ΔG*) of a chemical reaction is related to the cell voltage as follows:

$$\Delta G = -nF\Delta U_0 \tag{2.1}$$

Where *n* is the number of electrons involved in the reaction, *F* is the Faraday constant and ΔU_0 is the voltage of the cell for thermodynamic equilibrium in the absence of current flow [42]. Fuel cells are basically open thermodynamic systems; the maximum work that a fuel cell can obtain from a given fuel is determined by the second law of thermodynamics. The total work is equal to the negative value of the effective Gibbs (*G*) energy of the reaction under real operating conditions [43]. At

7

standard conditions (i.e., 25°C and 1 atm) for pure H_2 and O_2, the equilibrium cell voltage (ΔU_0) is 1.223 V for liquid water product and 1.164 V for gaseous water product [39]. Fuel cells are capable of processing a variety of fuels and oxidants however, those that process H_2 or H_2 rich media (such as organic alcohols) and air or O_2 as the oxidant are of more importance due to their high efficiency and low emissions [34]. In a typical fuel cell, the fuel is continuously fed to the anode and an oxidant to the cathode to produce electrical energy *via* electrochemical reactions at the electrode surface. **Fig. 2.1** shows a schematic diagram of the working principle of the PEMFC.
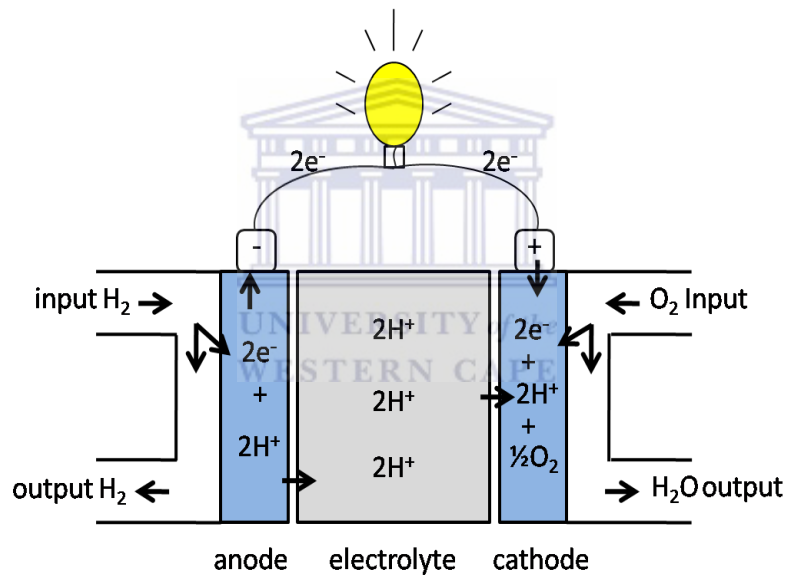
Fig. 2.1: Schematic diagram of the PEMFC [39].

In simplified terms, a fuel cell consists of an electrolyte region with two electrodes contacted on both sides. At the anode, the H_2 rich fuel is oxidised into positive and negative ions; i.e. protons (H^+) and electrons (e^-) for the case of pure H_2. Space separation is achieved by the special properties of the electrolyte membrane. The electrolyte membrane only permits the conduction of protons from the anode to the cathode and acts as an insulator for the electrons. Electrons are forced to take an

8

external circuit where it powers a given load before it reaches the cathode to combine with the protons and O_2 to form water [36, 39]. In the case of pure H_2 and pure O_2, water and heat would be the only by-products of the reaction. The electrode reactions can be represented as follows:

Anode reaction: $H_2 \rightarrow 2H^+ + 2e^-$ (2.2)

Cathode reaction: $\frac{1}{2}O_2 + 2\,H^+ + 2e^- \rightarrow H_2O$ (2.3)

Overall reaction: $H_2 + \frac{1}{2}O_2 \rightarrow H_2O$ $\Delta G = -237\ \text{kJmol}^{-1}$ (2.4)
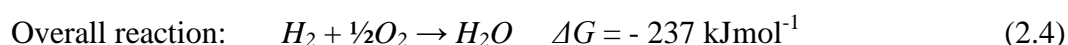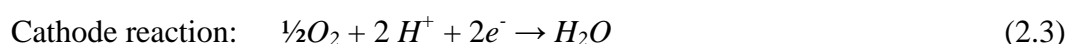
2.1.3 Fuel cell types

Fuel cells are classified according to the type of electrolyte and fuel it employs which determines the electrode kinetics and type of ions that carries the current across the electrolyte [34, 36]. Five categories of fuel cells have received major research attention; i.e. (i) PEMFC, (ii) solid oxide fuel cells (SOFC), (iii) alkaline fuel cells (AFC), (iv) phosphoric acid fuel cells (PAFC) and (v) molten carbonate fuel cells (MCFC) [36, 38]. PEMFCs, AFCs and PAFCs are considered low temperature fuel cells as it operate between 50 to 200°C. MCFCs and SOFCs are considered high temperature fuel cells as it operate between 650 to 1000°C [43]. **Table 2.1** provides important characteristics of each of these fuel cell types.

Type of fuel cell	Operating temperature, °C	Efficiency, % Cell	Output, kW	Electrolyte	Conduct-ing ion	Fuel
Alkaline (AFC)	60 to 120	60 to 70	0.3 to 5	35 to 50% KOH	OH^-	H_2
Molten carbonate (MCFC)	620 to 660	60 to 80	0.10	Molten carbonate melts (Li_2CO_3/Na_2CO_3)	CO_3^{2-}	Hydrocarbons, CO
Phosphoric acid (PAFC)	160 to 220	40 to 80	50 to 200	Concentrated H_3PO_4	H^+	H_2
Proton exchange membrane (PEMFC	50 to 80	40 to 50	50 to 200	Polymer membrane	H^+	H_2
Solid oxide	800 to 1000	50 to 60	50 to 100	Yttrium-Stabilised ZrO_2	O^{2-}	Hydrocarbons, CO

Table 2.1: Characteristics of the major fuel cell types [44].

2.2 From LT-PEMFCs to HT-PEMFCs

LT-PEMFC systems are very complex and expensive due to the requirement of humidification since proton conduction occurs *via* water. Operating at temperatures below 100°C results in low system efficiency and requires a *CO* selective oxidiser due to the low *CO* (< 10 ppm) tolerance of the *Pt* catalyst [45]. Catalyst poisoning by *CO* is a serious obstacle and needs to be addressed in order to make reformate gas a viable fuel for PEMFCs. Even after preferential oxidation, the outlet *CO* concentration is about 50 ppm [11].

At temperatures above ~80°C, the Nafion® membrane becomes unstable. Current research efforts are aimed at developing alternative electrolyte membranes [46] which include non-fluorinated hydrocarbon polymers [17], inorganic-polymer composites [47] and anhydrous proton conducting polymers [48] which can operate at temperatures above ~80°C without significant performance degradation. At 80°C and

lower temperatures, too much humidification can cause water to condense and flood the electrodes which makes water management difficult [17].

At temperatures above 100°C, water is only present in the vapour phase preventing the electrodes from flooding, thereby simplifying water management. The under-saturated operating environment alleviates mechanical stress imparted by water expansion upon freezing and facilitates rapid start-up in freezing conditions because melting ice becomes unnecessary [16]. The pressure loss in the fuel cell stack can be reduced since no liquid water has to be forced out of the cells thereby reducing the parasitic need for driving the air blower [49]. High temperature operation enables more effective cooling of the cell stacks and provides a means for combined electrical energy and heat generation. Utilisation of the high quality waste heat increases system efficiency *via* cogeneration [50]. At higher temperatures, faster reaction rates are achieved and the *CO* poisoning of the *Pt* catalyst is decreased [13] eliminating the requirement for high purity H_2. *CO* adsorption onto *Pt* exhibits negative value entropy thus being disfavoured at high temperatures [51]. H_2 produced from reforming of natural gas, coal and oil contains large amounts of *CO* and is a more viable option for HT-PEMFC operation [52]. At 130°C, *CO* tolerance will be increased up to 1, 000 ppm and at 200°C, *CO* tolerance will be increased up to 30, 000 ppm making the use of H_2 directly obtained from a simple reformer possible [53]. Reformate can thus be produced from a simplified gas processor in which the final *CO* purification step can be eliminated [54].

Real world tests of PEMFCs reveal that pure H_2 as anode inlet gas, yields best performance. For many applications pure H_2 is not yet a viable option due to a lack of

11

refuelling infrastructure and impractical storage techniques. The use of pure H_2 as anode inlet gas presents challenges, e.g. onboard H_2 storage. Refuelling for such systems would be slow and the major storage technologies (i.e. compression, liquefaction and metal hydrides) still has major disadvantages [3]. Other advantages of HT-PEMFCs include reduced system weight, volume and complexity which results in increased power density, specific power and functionality through system and component simplification [16]. In theory HT-PEMFCs have the potential to solve the inherent problems associated with LT-PEMFC. In practice however operating at higher temperatures (100 to 200°C) causes greater challenges for PEMFCs. An important requirement for high temperature operation is materials that give high performance and high durability.
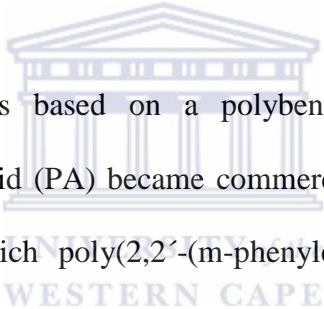
2.3 PEMFC components

For the commercialisation of PEMFCs, the lifetime of PEMFCs is of utmost importance. The operation requirement ranges from 5, 000 operating hours for cars, to 20, 000 operating hours for buses and up to 40, 000 to 90, 000 operating hours for stationary co-generation systems [55, 56]. To reach such targets the materials used to manufacture the PEMFC components should be durable, reliable and the lowest cost possible. The main components of the PEMFC structure are the MEA and bipolar plates. The MEA consists of the PEM, GDL and the CL. The reduced life time of HT-PEMFCs is considered to be mainly due to the degradation of the electrodes and the membrane [57].

12

2.3.1 Polymer Electrolyte Membrane

The PEM serves as the conductor of protons from the anode to the cathode, an electronic insulator and a separator of gases. It is important for these membrane functions to remain unimpeded during the lifetime of the fuel cell. Operation at high temperature requires materials with high thermal, mechanical and chemical stability. Novel materials that have high performance and durability are a prerequisite for HT-PEMFCs. Most important is an electrolyte membrane that can operate between 100 to 200°C and low relative humidity (25 to 50%) [17, 58]. Membranes should exhibit low fuel permeability, high proton conductivity, good mechanical strength, and good thermal and oxidative stability.

Recently HT-PEMFC MEAs based on a polybenzimidazole (PBI) membrane saturated with Phosphoric Acid (PA) became commercially available. Different PBI membranes are used of which poly(2,2´-(m-phenylene)-5,5´-benzimidazole) also known as meta-PBI **(Fig. 2.2 a)** are the most common. PBI and its derivatives are most promising for membrane materials in HT-PEMFCs since proton conduction occurs not only *via* the vehicle mechanism but also *via* the hopping mechanism [13]. Pure PBI membranes are electric and ionic insulators but with the impregnation with a strong acid it becomes good proton conductors. PA is most suitable as it is not aggressive towards the polymer structure, has a low vapour pressure and high chemical stability making it suitable for high temperatures [51]. PBI membranes doped with PA do not rely on hydration for conductivity therefore significantly lower water content compared to Nafion® membranes is required for proton conduction. PBI membranes are cheaper than Nafion® membranes however attention has recently been given to another PBI membrane i.e. poly(2,5-benzimidazole) also known as

ABPBI. The chemical structure of ABPBI is shown in **Fig. 2.2 b**. ABPBI is a simpler monomer than PBI [59] and can be prepared at a lower cost [60]. Both PBI and ABPBI membranes are promising for HT-PEMFCs because it shows good proton conductivity at temperatures up to 200°C, have low gas permeability, low methanol crossover and have excellent oxidative and thermal stability [61, 62].
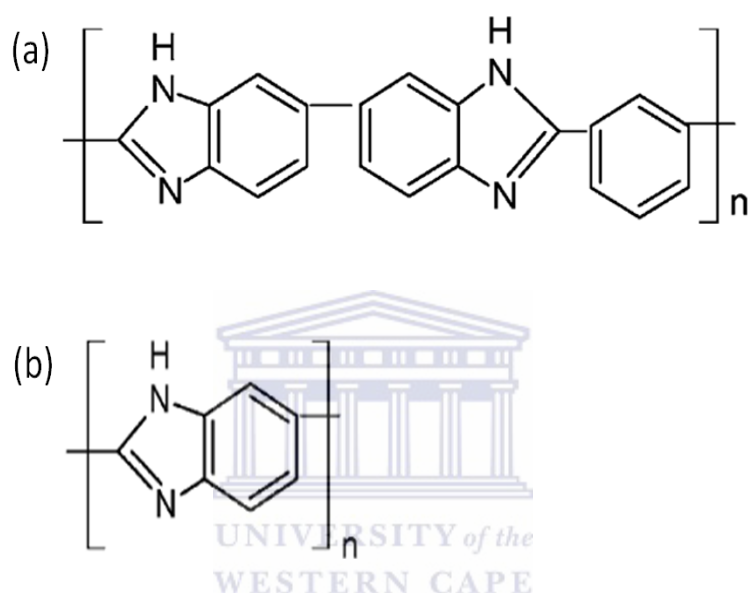
Fig. 2.2: Chemical structures of (a) Poly(2,2´-*m*-(phenylene)-5,5´-bibenzimidazole) and (b) Poly(2,5-benzimidazole) [24].

ABPBI is the simplest benzimidazole polymer since it can be prepared from a single, inexpensive and commercially available monomer (i.e. 3,4-diaminobenzoic acid) by condensation in polyphosphoric acid. Compared to PBI, ABPBI does not have the phenylene rings in the polymer backbone thus giving ABPBI a higher affinity towards PA [63]. ABPBI membranes yield higher uptakes of PA than commercial PBI membranes [64]. In these membranes, proton transport occurs in the PA groups. PA undergoes hydrogen bonding or proton transfer reactions with the *N-H* groups of the basic polymer [65]. Various methods were developed for introducing the PA into the MEA and are described in the open literature [23, 64, 66, 67]. Wannek *et al*. [67]

14

found that the performance of the HT-PEMFC was almost independent of the way that the PA was introduced into the MEA.

The overall performance of the PEM depends not only on the proton conductivity but also on its durability. Mechanisms of membrane degradation include chemical degradation, mechanical degradation and contamination by ionic species [68]. The durability of the PEM is closely associated with the chemical stability of the membrane. Polymeric membranes are prone to chemical attack by the peroxide radical ($OH^{\bullet}$) which is formed by the decomposition of H_2O_2 at the anode [2]. Compressive stress on the membrane during normal fuel cell operation leads to membrane thinning known as polymer creep which eventually leads to MEA degradation [69].
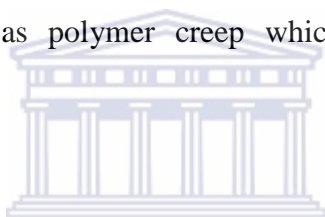
2.3.2 Gas Diffusion Layer

The GDL is sandwiched between the CL and the gas flow channels and its structure controls catalyst utilisation and overall cell performance. It allows gas transport to the CL, provides physical support for the CL and facilitates water product removal [70-72]. Gas transport through the porous gas diffuser occurs *via* momentum transport, concentration and pressure gradients [73]. The GDL can consist only of a microporous substrate known as a single layer GDL or consist of a carbon layer (known as a microporous layer, MPL) coated on a sheet of microporous carbon cloth or carbon paper known as a dual layer GDL. Carbon based GDLs are commonly used due to its stability in acidic environments, it provides high gas permeability, has good electronic conductivity, is elastic upon expansion and controls porous structures. Hydrophobic treatment of the GDLs are required to prevent water flooding and

15

facilitate oxygen transport at the cathode [72]. At higher operating temperatures, gas transport in the GDL is expected to be enhanced since no liquid water is present in the cell.

At higher temperatures faster degradation of the GDL structure due to carbon corrosion is expected. Carbon corrosion degrades fuel cell performance since the noble metal catalyst may be lost from the electrode or the noble metal catalyst particles may aggregate into larger particles. Oxidation of the carbon support can lead to changes in the surface hydrophobicity that may lead to gas transport difficulties [74]. Research into carbon corrosion has in recent years received considerable attention. The suggested mechanism for carbon corrosion involves the reaction between carbon and water as shown in Eq. (2.5) [57, 75]:

$$C + 2H_2O \rightarrow CO_2 + 4H^+ + 4e^- \qquad E^0 = 0.207 \text{ V vs NHE} \qquad (2.5)$$

The equilibrium potential of carbon corrosion is 0.207 V versus a normal hydrogen electrode (NHE) at 25°C which implies that carbon is thermodynamically unstable to electrochemical carbon corrosion. However due to the slow reaction kinetics it is still possible to use carbon in PEMFCs. Oh *et al.* [57] showed that more carbon corrosion occurs in HT-PEMFCs compared to LT-PEMFCs which they attributed to the enhanced kinetics of carbon corrosion at higher temperatures. They observed a strong dependence on the water content therefore it is important to remove the water content in the gas supply to reduce electrochemical carbon corrosion. They also attributed the reduced life time of HT-PEMFCs to the degradation of the electrodes due to factors such as *Pt* agglomeration. To reduce PEMFC degradation due to carbon corrosion,

16

carbon materials containing a graphite component are recommended. Carbon nanotubes are also investigated as a promising catalyst support due to its high electron conductivity and enhanced transport capability [74].

2.3.3 Catalyst Layer

The CL is a thin and porous (30 to 60% porosity) layer that is coated onto the GDL and contains the active catalyst material. The CL is where all electrochemical reactions take place. The pores in the CL allow the transport of reactant gases to the active catalyst sites and the removal of the water vapour product out of the CL [76]. *Pt* is known to be the most active catalyst for the Oxygen Reduction Reaction (ORR) in PEMFCs and is most commonly employed in the CL for both the ORR and Hydrogen Oxidation Reaction (HOR). The high cost of the *Pt* material still imposes one of the most important hindrances for fuel cell commercialisation. Therefore it is important to minimise the amount of *Pt* required to lower the production cost of the fuel cell. Significant research efforts are dedicated to lowering the *Pt* requirement for PEMFCs without compromising the overall cell performance. The dispersion of the *Pt* nano-particles on a high surface area carbon support (i.e. *Pt/C*) has been quite successful at achieving such reductions in the *Pt* requirement. *Pt/C* is currently the most commonly used catalyst material [77, 78] and has become one of the most efficient catalysts for LT-PEMFCs. **Fig. 2.3** shows a HR-TEM image of the *Pt/C* catalyst.
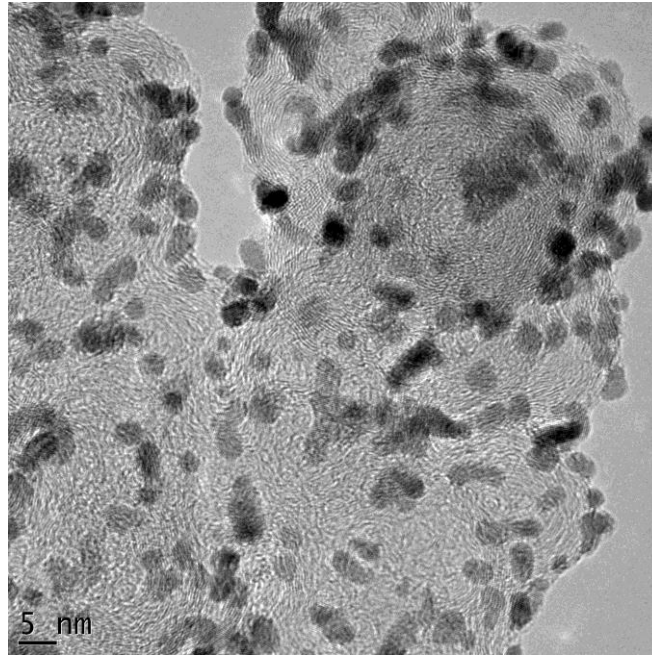
Fig 2.3: HR-TEM image of 40 wt% *Pt/C* **(Johnson Matthey, HiSpec 4000).**

High cell performances can be achieved with well dispersed *Pt* catalysts and if the cathode catalyst is well designed to maximise catalyst utilisation [16]. *Pt/C* catalysts contains *Pt* clusters less than 5 nm and is usually prepared *via* a chemical method [79].

Another method of reducing the *Pt* requirement or improving catalyst activity is by substituting some of the *Pt* with non-noble metals or other noble metals. Olson *et al.* [80] studied a non *Pt* catalyst based on cobalt for LT-PEMFCs cathodes however they observed that even at low current densities, transport processes limited the overall performance. Parrondo *et al*. [81] added tin oxide to produce a *Pt/SnO$_x$/C* catalyst and tested its performance and stability under high temperature conditions. They observed that the addition of tin oxide yielded a catalyst that was stable under HT-PEMFC conditions and showed a better performance (i.e. 0.58 V at 200 mA/cm^2) compared to their *in-house Pt/C* catalyst (i.e. 0.4 V at 200 mA/cm^2). However the addition of tin

18

oxide was limited to 7 wt% since at higher concentrations of tin oxide the performance decreased due to mass transport limitations in the electrode.

Another important aspect of the catalyst material is that it should be stable under the operating conditions to ensure a long life time of the PEMFC. Two main mechanisms are identified for *Pt* surface area loss: (i) a dissolution-reprecipitation mechanism also referred to as Oswald ripening where *Pt* dissolves and forms ions in the electrolyte and re-deposits onto larger crystallites and (ii) a particle migration-coalescence mechanism or particle diffusion where *Pt* crystallites migrate on the support surface, impinge and merge to form larger particles [82]. Lobato *et al.* [83] observed that although higher temperatures increased the electrochemical activity of the *Pt/C* catalyst, the higher temperatures also increased *Pt* agglomeration causing a lowering in the electrochemically active surface area over time. The CL is in direct contact with the membrane doped with 15M PA, an extremely acidic environment which may accelerate catalyst degradation. Zhai *et al.* [84] similarly observed serious agglomeration of the *Pt* particles during the first 300 hours of cell testing which resulted in a significant loss in the active surface area of the *Pt/C* cathode catalyst. They did not observe any *Pt* particles in the membrane which suggested that *Pt* dissolution did not occur. **Fig. 2.4** shows a list of materials that is commonly considered for MEA components.

```
                    Membrane Electrode Assembly
                                  |
        ┌─────────────────────────┼─────────────────────────┐
    Membrane                 Catalyst Layer          Gas Diffusion Layer
```

Membrane

Perfluorinated:
* Perflurosulfonic acid
* Perfluorocarboxylic acid
* Bis(perfluoroalkylsulfonyl)imide
* Gore-Select™

Partially Fluorinated:
* a, ß, ß-trifluorostyrene grafted onto poly (tetrafluoroethylene-ethylene) with post sulfonation
* Styrene grafted and sulfonated poly (vinylidenefluoride)[PVDF-g-PSSA]

Non-Fluorinated:
* Naphthalenicpolyimide
* BAM3G membrane (Ballard Advance Material of 3rd Generation Membrane)
* Crosslinked or noncrosslinked Sulfonatedpolyetheretherketone
* Sulfonated poly (4-phenoxy benzoyl-1, 4-phenylene)[S-PPBP]
* Methylbenzensulfonated Polybenzimidazoles[MBS-PBI]
* Methylbenzensulfonated-Poly (p-phenyleneterephthalamide)[MBS-PPTA]
* Imidazole doped Sulfonated polyetherketone[S-PEK]

Non-Fluorinated Composite:
* Acid-doped Polybenzimidazoles
* Base-doped S-Polybenzimidazoles

Others:
* Poly (2-acrylamido-2-methylpropanesulfonic acid (Poly-AMPS)
* Supported composite membrane

Catalyst Layer

Single Metal Catalysts
* Pt/C

Binary Catalysts:
* Pt-Ru/C
* Pt-Mo/C
* Au-Pd/C

Tertiary Catalysts:
* Pt-Ru-Mo/C
* Pt-Ru-W
* Pt-Ru-Al$_4$
* Pt-Re-(MgH$_2$)

Gas Diffusion Layer

* Graphite paper wet-proofed with polytetrafluoroethylene
* Graphite cloth wet-proofed with polytetrafluoroethylene

Fig. 2.4: Classification of MEA materials [21].

2.3.4 Bipolar plates

Bipolar plates play important functions in the fuel cell stack such as separating individual cells, providing mechanical support for the cells, carrying electrical current away from the cells, distributing fuel and oxidant homogeneously within individual cells and facilitates water management in the cells [5, 85]. A variety of materials are proposed for manufacturing bipolar plates. At the laboratory scale, graphite is commonly used as material for the bipolar plates. Graphite has high electrical conductivity and high chemical stability however it is brittle and lack mechanical

20

resistance. Machining of the flow field channels into pure graphite is a complicated and time intensive step and cannot be mass produced, hence the high cost [5, 86].

An alternative to using pure graphite plates are composite bipolar plates based on graphite particles and a mixture of polymers [5]. Metallic bipolar plates have higher material strength, are more durable to shock and vibration, have superior manufacturability and are more cost effective. The main disadvantage of using metallic materials for bipolar plates is its susceptibility to corrosion in the acidic PEMFC environment causing metallic impurities that would contaminate and degrade MEA performance [87].

The requirements for bipolar plates are ultimately determined by the application and operating temperature of the fuel cell. For mobile and transportation applications, the bipolar plates should be thin, light weight and be able to withstand the harsh and changing environments where operating temperature, humidity and loads continuously change to meet demands. For stationary applications the durability of the bipolar plates become more crucial than the size and volume, however, the cost should always be considered [88]. **Table 2.2** shows the performance requirements as specified by the United States Department of Energy that a material should meet to be considered suitable for bipolar plate manufacturing.

Property	Unit	Value
Tensile strength – ASTM D638	MPa	> 41
Flexural strength – ASTM D790	MPa	> 59
Electrical conductivity	S/cm	> 100
Corrosion rate	$\mu A/cm^2$	< 1
Contact resistance	$m\Omega cm^2$	< 20
Hydrogen permeability	$cm^3/(cm^2\ s)$	$< 2.10^{-6}$
Mass	Kg/kW	< 1
Density – ASTM D792	g/cm^3	< 5
Thermal conductivity	W/(m K)	> 10
Impact resistance (unnotched ASTM D256	J/m	> 40,5

Table 2.2: Performance requirements of materials for PEMFC bipolar plates [5].

2.4 Catalyst suspensions

The CL is commonly formed from colloidal catalyst suspensions (also called catalyst ink) which comprises of the active catalyst material on a suitable support (e.g. *Pt/C*), an ionomer (such as the Nafion® ionomer) or polymer binder (such as PTFE) and a dispersing solvent. **Fig 2.5** shows the chemical structures of the Nafion® ionomer and PTFE.
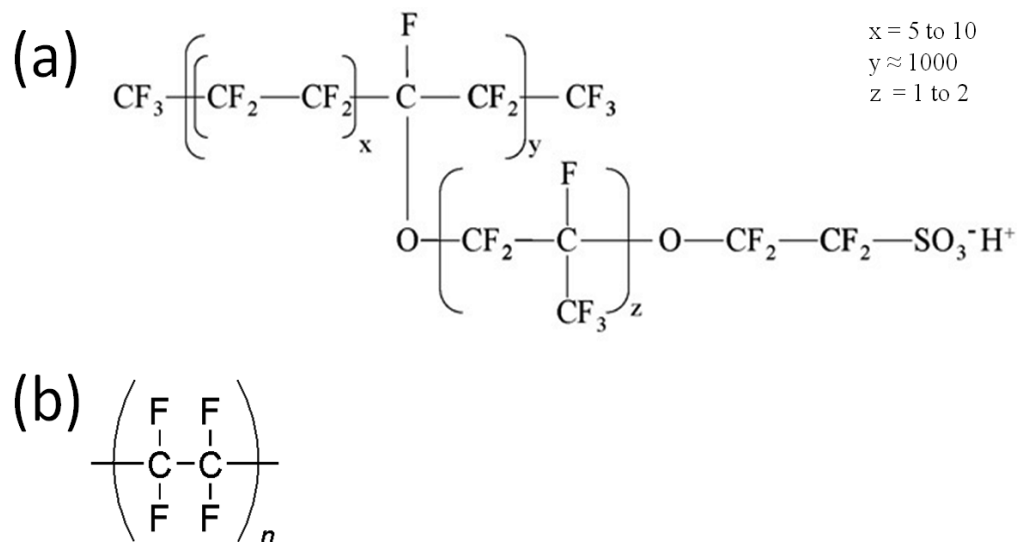
Figure 2.5: Chemical structures of (a) Nafion® ionomer and (b) PTFE.

A well-mixed catalyst suspension is usually obtained *via* ultrasonic mixing. It is important to be able to control the micro-structure of the CL which has a direct impact on the performance of the PEMFC. The dispersion state of the ionomer/polymer and the active catalyst particles in the CL has a significant impact on the MEA performance and catalyst utilisation. The solvent dielectric constant (ε) and viscosity is commonly studied to increase the electrochemical surface area and to reduce the mass transport resistance of the formed CL. The solvent can affect the CL morphology, size of the catalyst particles and the pore size distribution of the CL [89].

The substrate supported catalyst particles (e.g. *Pt/C*) are insoluble in the solvent and forms heterogeneous aggregates [90]. The solubility of the ionomer/polymer binder depends on the solvent. The Nafion® ionomer forms a solution with a solvent with $\varepsilon > 10$, a colloidal system with solvents with ε between 3 and 10 and a precipitate with solvents with $\varepsilon < 3$. When the Nafion® ionomer is mixed with IPA ($\varepsilon = 18.3$), the Nafion ionomer completely dissolves to form a solution state while in normal-butyl acetate (NBA, $\varepsilon = 5.01$), the Nafion® ionomer forms a colloidal suspension. The Nafion® ionomer in the colloidal state yields improved MEA performance compared to the Nafion® ionomer in the solution state. In the colloidal state, the Nafion® ionomer increased porosity and lowered mass transport resistance of the CL while in the solution state, the Nafion® ionomer blocks electron conduction by covering the carbon particle as well as the active *Pt* sites needed for electrochemical reactions [91].

Huang *et al*. [92] studied various solvents to determine its effect on MEA performance. The solvents they studied were water, ethylene glycol, glycerin, propylene glycol and methanol. The best MEA performance was obtained when

ethylene glycol was used as the solvent due to a better dispersion of the catalyst particles and higher active surface area. The electrodes obtained from ethylene glycol suspensions exhibited less cracks compared to the electrodes obtained from the methanol suspensions. Chun *et al*. [93] studied the effect of glycerol in the catalyst suspension and observed a significant decrease in MEA performance at high current densities (i.e. > 350 mA/cm^2) for high glycerol contents (i.e. 3:1 glycerol to 5 wt% Nafion® ionomer solution). They suggested that high glycerol contents reduced the contact area between the catalyst particles and the Nafion® ionomer and limited charge transfer. Millington *et al*. [94] also studied various solvents namely tetrahydrofuran (THF), IPA, ethylene glycol and glycerol. They obtained the best MEA performance from THF (i.e. 0.52 Wcm^{-2}), second best performance from IPA (i.e. 0.49 Wcm^{-2}), third best performance from ethylene glycol (i.e. 0.31 Wcm^{-2}) and poor performance from glycerol (i.e. 0.01 Wcm^{-2}). They explained their observations on the basis of solvent dielectric constant; THF had $\varepsilon = 7$ while the other solvents had $\varepsilon > 10$. The Nafion® ionomer formed a colloidal suspension in THF while forming solutions in the IPA, ethylene glycol and glycerol. Song *et al.* [95] combined polytetrafluoroethylene (PTFE) with the Nafion® ionomer to form a hydrophobic thin film CL. They observed that presence of the Nafion® ionomer reduced the aggregation of PTFE in a mixture of distilled water and IPA.

For EPD it is important to prepare stable catalyst suspensions of individual particles and low ionic conductivity. Water as a solvent for EPD imposes challenges such as the electrolysis of water and gas evolution at the electrodes at high voltages as well as joule-heating that may destabilise the suspension. The use of organic solvents which have significantly lower dielectric constants compared to water greatly reduces the

occurrence of electrolysis and joule-heating. Alcohols such as methanol and ethanol are similar to water and is susceptible to ohmic heating [96]. Louh *et al.* [31] studied various solvents such as acetyl acetone, IPA, deionised water and ethanol for the EPD method. They observed that IPA was the most suitable solvent to prepare the suspensions as the least precipitation of the catalyst particles was observed.

The choice of solvent for catalyst suspension preparation ultimately depends on the fabrication method as well as the ionomer/binder that will be incorporated in the CLs.

2.5 MEA fabrication methods

The fabrication method affects the structural properties of the MEA which affects its performance characteristics. The MEA should have a long life time, a high power output and be cost effective to become commercially available. During the past few decades many efforts was made to decrease the noble metal catalyst loading without compromising the MEA performance. In the early stages of MEA development, PTFE was used as a binder in the CL and *Pt* loadings as high as 10 mg/cm^2 were incorporated in the CL. These high *Pt* loadings were significantly reduced to below 1 mg/cm^2 without sacrificing cell performance. This was achieved by incorporating the Nafion® ionomer into the CLs which led to increased *Pt* utilisation [92]. Fuel cell performance can be improved by increasing the overall catalyst utilisation per unit surface area of the MEA to effectively make gaseous fuel undergo desirable catalytic reaction [22]. Litster et *al.* [97], after carefully studying the literature on PEMFC electrode design, observed that the main resistance in the CL was the membrane-CL interface contact resistance. The ability of the interface to conduct protons from the membrane to the CL is crucial.

Various MEA fabrication methods are currently investigated and most are summarised in **Fig. 2.6**. Common catalyst deposition methods include spraying (hand or automated), hand brushing, direct printing, screen printing and decal transfer. Less common methods include electrodeposition, DC magnetic sputtering, EPD and even combinations of these methods [6].
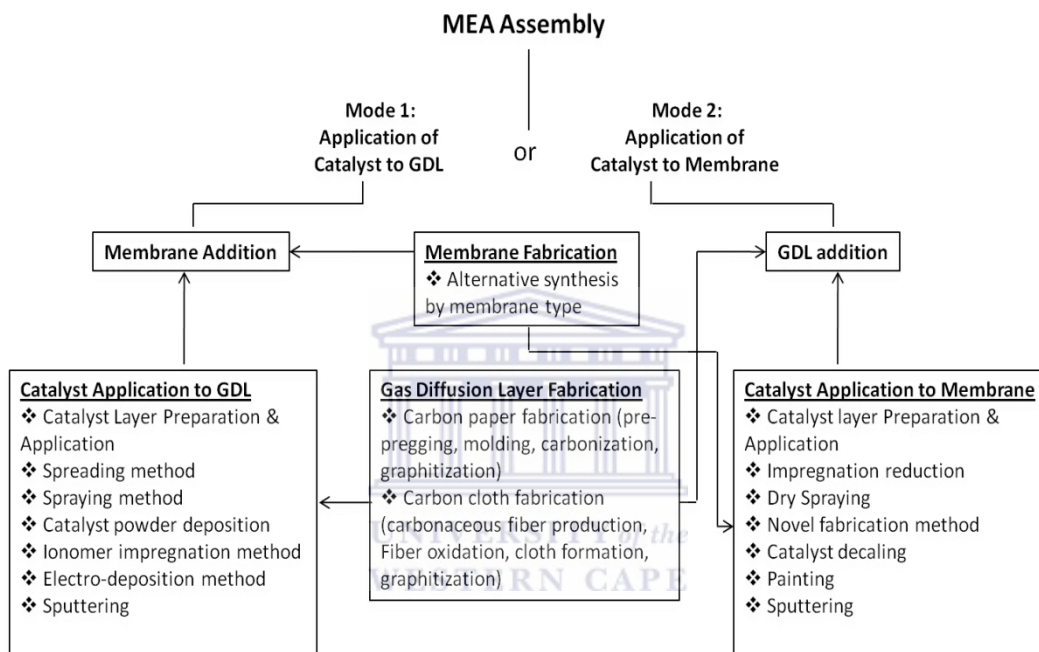
Fig. 2.6: Classification of MEA fabrication methods [21].

An ideal MEA fabrication method should be reproducible, fast and up scaling should be possible [7]. Spraying methods for MEA fabrication have reproducibility issues as well as result in high catalyst loadings. Thin sputtered CLs were found to be promising for low catalyst loadings with adequate performance. A key advantage for electrodeposition methods was the ability to mass-produce electrodes in a commercial plating bath [97].

More recently attention was given to EPD for MEA fabrication and was successfully demonstrated for the deposition of CLs in MEAs. Deposition was achieved both on electron-conducting substrates (i.e. GDLs) which simultaneously served as one of the electrodes as well ion-conducting substrates (i.e. Nafion® membrane) where the membrane was placed between two external electrodes [22, 29-32]. Louh *et al.* [22] used EPD to deposit the MPL onto the carbon textile to form GDLs, followed by the deposition of the CL to form GDEs. The deposited MPL and CL formed a continuous porous structure with the carbon textile which reduced the impedance between the electrodes in the fuel cell and resulted in improved electrical conductivity of the MEA. Morikawa *et al.* [32] showed that the EPD method has selectivity for particle size since they only observed fine carbon particles in the deposited layer. Such selectivity for particle size should produce deposits of high uniformity and thereby increase *Pt* utilisation. Using Cyclic Voltammetry (CV) and *CO* adsorption experiments they calculated a *Pt* utilisation of 56%. Munakata *et al.* [30] used the EPD method to deposit the catalyst particles directly onto a Nafion® membrane to form the MEA. They observed CLs that were well attached to the membrane and also the EPD method was selective towards particle size. Their EPD MEAs showed better performance than the hot press MEA with a maximum of 76% *Pt* utilisation compared to 28% *Pt* utilisation obtained by the hot pressing method. Jeng *et al.* [29] used a low voltage (i.e. 0 to 5 V) EPD method from a semi-aqueous (i.e. containing water and alcohols) solution to fabricate GDE/MEAs for Direct Methanol Fuel Cell (DMFC) applications. The deposited CL was thin and uniform however the impedance of the CLs was high which they attributed to the preferential deposition of the Nafion® ionomer instead of the catalyst particles.

2.6 Electrode reactions in PEMFCs

2.6.1 Oxygen Reduction Reaction

The overall electrochemical kinetics of the PEMFC is determined by the slow ORR [46]. Due to the sluggish ORR kinetics, the over-potential at the cathode accounts for the major voltage (> 50%) loss during PEMFC operation. Even on *Pt*, which is the most active catalyst for the ORR in PEMFCs, the ORR over-potential is on the order of 300 to 400 mV [98]. In aqueous electrolyte, the ORR can proceed by two overall pathways, i.e. a direct four electron pathway and an indirect two electron pathway. The direct four electron pathway is preferable as it does not involve peroxide species in the solution and the Faradaic efficiency of the reaction is greater. The direct four electron pathway consist of different steps in which O_2 has to be dissociated at the surface and recombine with H^+ to form water [42]. For a non-polar species like O_2, direct adsorption is likely to be inhibited relative to for example, the adsorption of charged superoxide radical anion ($O_2^{\bullet-}$), unless the free energy of adsorption of O_2 is very exothermic on a specific catalyst surface. In fuel cells this is especially true because the cathodic reaction in fuel cells typically occurs at potentials well positive to the point of zero charge (pzc) [99]. At higher temperatures, ORR kinetics is significantly increased which should result in improved PEMFC performance [100].

2.6.2 Hydrogen Oxidation Reaction

The oxidation of hydrogen occurs readily on the *Pt* based catalyst. The exchange current density for the electrochemical ORR (i.e. ~10^{-8} to 10^{-9} A/cm^2) is much smaller than the HOR (i.e. $\approx 10^{-3}$ to 10^{-4} A/cm^2). Since the HOR at the *Pt*-PEM interface is quite fast and reversible, it is negligible even at very low *Pt* loadings (i.e. < 5 mV at the anode for a *Pt* loading of 0.05 mg/cm^2) when the anode is adequately hydrated

[46, 98]. At higher temperatures (i.e. > 100°C), anode dehydration may become a significant challenge. The mechanism of hydrogen electro-oxidation on *Pt* in acid electrolytes is thought to proceed by the rate determining dissociative chemisorption of H_2 as shown by Eq. (2.6) followed by electrochemical oxidation as shown by Eq. (2.7) [3, 42, 101]:

$$H_2 + 2\ Pt_s \leftrightarrow 2Pt\text{-}H_{ads} \tag{2.6}$$

$$2Pt\text{-}H_{ads} \leftrightarrow 2Pt_s + 2H^+ + 2e^- \tag{2.7}$$
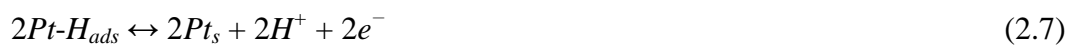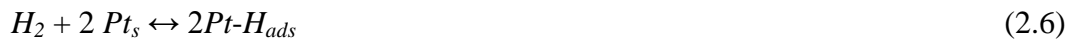
Where Pt_s is a free surface site and $Pt\text{-}H_{ads}$ is an adsorbed hydrogen atom on the *Pt* active site. The dissociative chemisorption of H_2 requires two adjacent *Pt* surface atoms while the electrochemical oxidation of the chemically adsorbed hydrogen atoms produce two free *Pt* sites, two protons and two electrons [3]. The overall reaction for hydrogen oxidation is:

$$H_2 \rightarrow 2H^+ + 2e^- \qquad\qquad U_0 = 0\text{V} \tag{2.8}$$
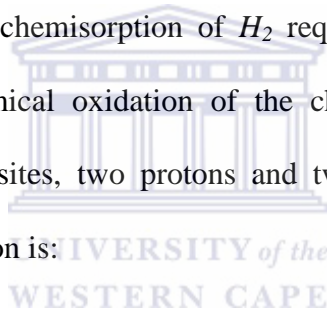
2.6.3 HT-PEMFC performance

Most fuel cell systems produce electrical energy at high efficiency that may range from 40 to 60% based on the lower heating value (LHV) of hydrogen and the remainder will be generated as waste heat. The fuel conversion efficiency is higher than that of generators powered by internal combustion engines such as piston engines and gas turbines. The efficiency advantage becomes more significant at smaller scales since the efficiency of fuel cells is nearly constant with size. A higher operating temperature corresponds to lower theoretical voltages and lower theoretical

29

efficiency. A higher operating temperature also leads to higher electrochemical activity at the electrodes, a higher efficiency and a higher quality waste heat [35]. The performance of a PEMFC in a kinetically controlled system can be represented by the Tafel equation [46]:

$$E = E_{rev} + b \log i_0 - b \log i \tag{2.9}$$

$$b = -2.3\, RT/\alpha nF \tag{2.10}$$

Where E is the electrode potential, E_{rev} is the reversible potential, b is the Tafel slope, i is the current density, i_0 is the exchange current density, n is the number of electrons transferred in the rate determining step, and α is the transfer coefficient. It was experimentally observed that the Tafel slope corresponding to the ORR increased with temperature at low current density while it was independent on temperature at high current density. Therefore at higher temperatures, the kinetics of the ORR will be improved [102].

In HT-PEMFCs, PA also plays a role as an ion conductor in the CL and influences electrode kinetics. Two challenges associated with PA in PBI based systems is a lowering in activity of the catalysts and loss of PA in the fuel cell gas/vapor exhaust streams [52]. Concentrated PA imposes slow kinetics for oxygen reduction on the cathode due to a strong adsorption effect of phosphate anions (PO^{4-}) onto the active catalyst sites as well as the low solubility and diffusivity of oxygen [24]. Neyerlin *et al.* [103] observed an overall voltage loss of > 200 mV regardless of the current density for a *Pt-Ni/C* cathode catalyst. This was about two orders of magnitude decrease in the exchange current density for the ORR which was attributed to the

adsorption of ions, specifically PO_4^-. Kwon *et al.* [104] also observed a lowering in the cell performance when the electrodes contained excessive amounts of PA. It is therefore necessary to optimise the PA content in the electrodes to avoid or minimise cell performance losses.

2.7 EPD overview

2.7.1 Electrical Double Layer

In a colloidal system, forces between neighbouring particles consist of intrinsic Van der Waals attraction and electrostatic repulsion due to particle surface charges. In some systems other effects may also exist such as steric repulsion due to the presence of surfactants or polymers, structural forces due to the molecules of the solution and a hydrophobic force due to the presence of hydrophobic surfaces of solids [105, 106]. Electrical charge of colloids in aqueous solutions can be due to the following: (i) surface group ionisation which is controlled by the pH of the suspension, (ii) differential solubility of ions, (iii) isomorphous replacement or lattice substitution, (iv) charged crystal surface fracturing due to crystal revealing surfaces with different properties and (v) specific ion adsorption. The surface charge are established by potential determining ions (DPI) which normally include the ions of the solid such as hydrogen, hydroxyl ions and ions capable of forming complex or insoluble salts with the solid. Ions of opposite charge (i.e. counter ions) are attracted toward the surface and ions of like charge (i.e. co-ions) are repelled away from the surface. A net electrical charge of one sign is formed on one side of the interface and a charge of opposite sign are formed on the other side giving rise to the electrical double layer (EDL) [107]. The formation of an EDL is a fundamental characteristic of a two phase system and is largely responsible for macroscopic properties of colloidal dispersions

31

such as stability, rheology, turbidity, etc. The electrical properties of the particles can be characterised by the zeta potential which represents the hydrodynamic shear plane [108]. **Fig. 2.7** shows a schematic representation of the EDL.
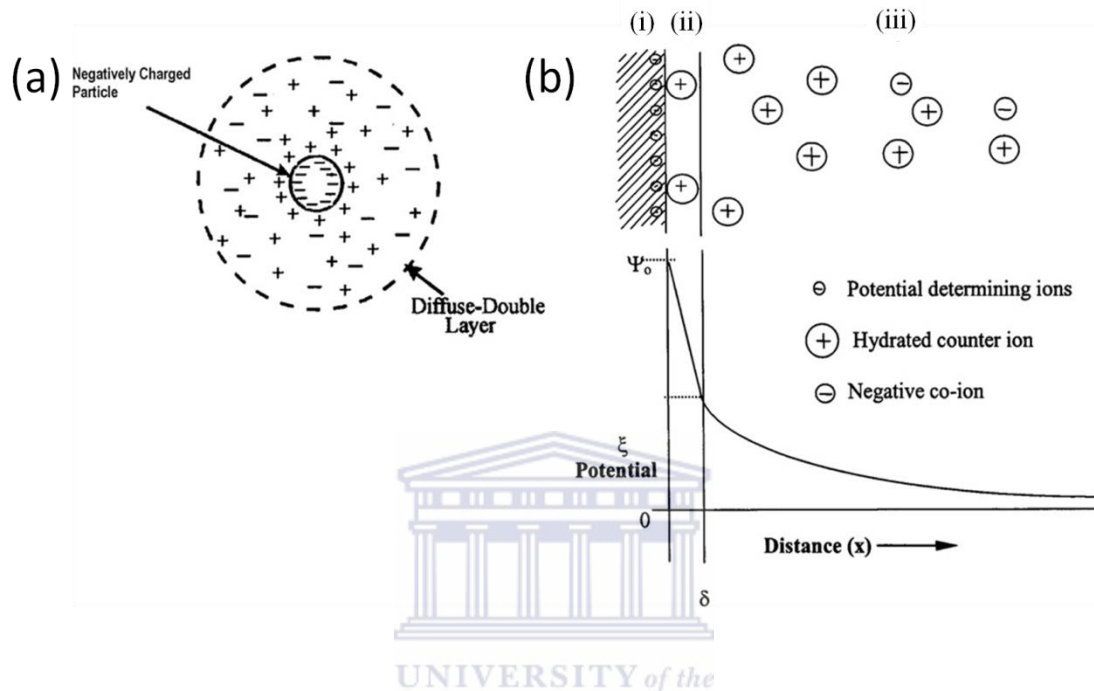
Fig. 2.7: Schematic representation of (a) double layer and (b) potential drop across the double layer (i) surface charge, (ii) Stern layer, (iii) diffuse layers of counter-ions [107].

2.7.2 Derjaguin, Landua, Verwey and Overbeek theory

The point where the potential energy opposing coagulation disappears is called the Critical Coagulation Concentration (CCC). An estimation of the CCC can be obtained by using an approximate expression for the potential energy of attraction and the potential energy of repulsion. The Derjaguin, Landau, Verwey and Overbeek (DLVO) theory states that the stability of a colloid depends on the balance of all forces and the total potential energy of particle interactions as they approach each other [105, 109, 110]. To obtain a stable colloid, a high surface charge is required to induce a high repulsive force. Stability arises from the particle surface charge interaction, hence

32

known as electrostatic stability. The total potential energy is affected by the ionic strength of the suspension and the surface potential of the particles. It involves the electrostatic repulsive force which depends on the degree of EDL overlap and the attractive force caused by the Van der Waals interaction. The total interaction energy (V_{total}) can be written as

$$V_{total} = V_{vdw} + V_{elect} \qquad (2.11)$$

$$\text{where } V_{vdw} = -\frac{Ha}{12S} \qquad (2.12)$$

is the attractive potential energy due to the van der Waals interactions between the particles and

$$V_{elect} = 2\,\pi\varepsilon_0\varepsilon a\psi_0^2 \ln(1 + e^{-ks}) \qquad (2.13)$$

is the repulsive potential energy resulting from electrostatic interactions between like charged particle surfaces. H is the Hamakar constant, S is the inter-particle distance, a is the particle radius, ε_0 is the permittivity of free space, ε is the dielectric constant of the medium, ψ_0 is the surface potential and k is the Debye-Huckle constant [109]. When the surface charge density relative to the ionic strength is high, the net particle interaction is repulsive and a low viscosity stable suspension is obtained. When the surface charge density relative to the ionic strength is low, an agglomerated suspension is obtained [111].

For some systems, stable suspensions are obtained by simply dispersing the particles in the solution. In general particles can be positively or negatively charged by adding

33

appropriate amounts of acid, base or polyelectrolytes (having functional groups such as carboxylic acid groups or amino groups on the side chains) to the suspension. Polyelectrolyte surfactants adsorb onto the surfaces of the particles and modify the surface charges and thus electrostatic forces [111, 112]. Electrostatic repulsive forces are the main source of stabilisation of the suspension. Steric hindrance and a combination of electrosteric repulsions may also be responsible for stabilisation. Colloidal stability is therefore governed by the total inter-particle energy, V_{total}, which can be expressed mathematically as follows:

$$V_{total} = V_{vdw} + V_{elect} + V_{steric} + V_{structural} \tag{2.14}$$

where V_{vdw} is the attractive potential energy due to the Van der Waals interactions between the particles, V_{elect} is the repulsive potential energy resulting from electrostatic interactions between like charged particle surfaces, V_{steric} is the repulsion between particle surfaces coated with adsorbed polyelectrolyte species and $V_{structural}$ is the potential energy resulting from the presence of non-adsorbed species in solution which may increase or decrease suspension stability [111].

2.7.3 EPD background

EPD was discovered by the Indian scientist G.M. Bose during the 1740's in a liquid-siphon experiment [113]. In 1807, the Russian scientist Ruess observed the movement of clay particles in water under an induced electric field. The first practical application of EPD came in 1933 when the deposition of thoria particles on a *Pt* cathode as an emitter for electron tube application was patented in the USA [107, 113]. EPD can be applied to any solid (< 30 μm) that is available in a powder form or a colloidal

suspension. EPD can be used to produce coatings, for shaping monolithic, laminated and graded freestanding objects, woven fibre pre-forms for composite production and for the infiltration of porous materials [96]. EPD from both aqueous and non-aqueous media plays an important role in many industries such as cosmetics, chemicals, pharmaceuticals, paint and pigments, microelectronics, ceramics, etc. [111].

EPD is usually carried out in a two electrode cell as illustrated by **Fig. 2.8**. There are two kinds of EPD that can be defined depending on the sign of the particles. If the particles are positively charged, it will move towards the negatively charged electrode (i.e. cathode) and the process is called cathodic EPD. If the particles are negatively charged, it will move toward the positively charged electrode (i.e. anode) and the process is called anodic EPD [114].
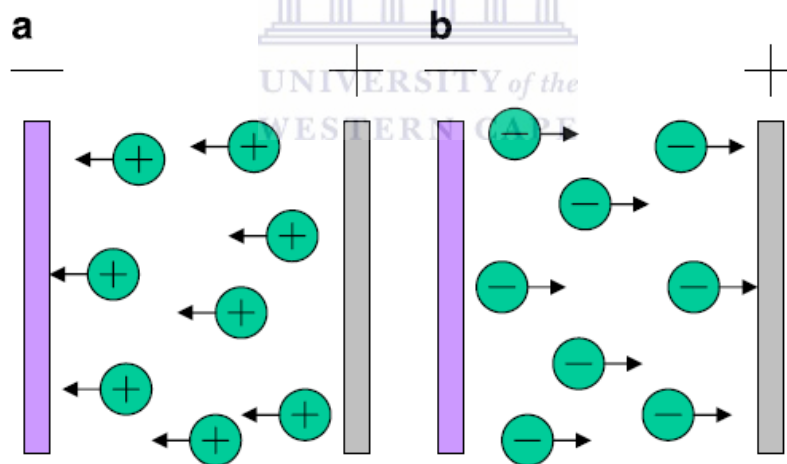
Fig. 2.8: Schematic representation of the electrophoretic deposition process (a) cathodic EPD and (b) anodic EPD [31].

The first model for EPD kinetics was proposed by Hamaker in order to predict the deposition yield [115]. The yield of deposition during EPD with planar electrodes is described by the Hamaker equation [116]:

$$Y = \sigma C \iint \frac{dV}{dn} dS \, dt \qquad (2.15)$$

Where Y is the deposition yield (g), C is the particle concentration (g/cm^3), dV/dn is the electric field strength (V/cm) perpendicular to the surface, S (cm^2), and σ is a constant (cm^2/Vs) that is equal to the electrophoretic velocity when every particle reaching the electrode takes part in the formation of the deposit. The parameter σ is dependent on the chemical composition of the suspension however it is independent on the physical experimental conditions.

In recent years, EPD has received considerable attention from academia and is applied in various applications in different research fields. EPD has received significant attention by SOFC researchers [117-122] for fabricating electrodes while very few PEMFC researchers have given attention to EPD. PEMFC researchers who studied EPD have only focussed on fabricating catalyst materials and electrodes for LT-PEMFCs. Hsu *et al*. [123] used EPD to synthesise a catalyst for methanol oxidation by depositing *Pt-Ru* nano-particles onto carbon nanotubes. The *Pt-Ru* nano-particles had an average particle size of 2.08 nm and the catalyst material showed good activity (1.6A/cm^2/mg) toward the electro-oxidation of methanol suitable for fuel cell applications.

2.8 Mechanism of EPD

The mechanism of EPD involves two steps: (i) an electric field is applied between two electrodes and charged particles suspended in a suitable liquid move toward the oppositely charged electrode (i.e. electrophoresis) and (ii) particles accumulate at the

deposition electrode and create a compact and homogeneous thin film [26, 96, 107, 124, 125]. The process only produces a compact powder therefore EPD should be followed by a densification step such as sintering or curing to obtain a fully dense material [96, 126]. The second step of EPD is still a controversial matter and both the particle aggregation mechanism and particle arrangement at the electrode surface are open for further research. The following mechanisms of particle aggregation or deposit formation are proposed: (i) particle charge neutralisation, (ii) electrochemical particle coagulation or zeta potential lowering, (iii) flocculation by particle accumulation [124, 127] and (iv) EDL distortion and thinning [124]. The particle charge neutralisation mechanism proposes that the particle charge neutralises upon contact with the electrode. The particle charge neutralisation mechanism works well for the initial stages of EPD from dilute suspensions. The particle charge neutralisation mechanism however becomes invalid for long EPD times when the pH changes due to particle-electrode interactions and when particles are prevented from contacting the electrode (e.g. the presence of a semi-permeable membrane between the two electrodes). The electrochemical particle coagulation mechanism proposes that an increase in electrolyte concentration near the electrode surface lowers the particle zeta potential. The electrochemical particle coagulation lowering mechanism is valid in solutions (e.g. water) where electrode reactions generate OH^- however it is invalid when no increase in electrolyte concentration occurs at the electrode surface. The particle accumulation mechanism proposes that the electric field moves particles toward the electrode where it accumulates. Pressure exerted by incoming particles and those in the outer layers causes the formation of a deposit. The particle accumulation mechanism is feasible only when deposition occurs on a porous membrane and not on the electrode. The increase in particle concentration at the electrode causes the

particle zeta potential to shift toward the isoelectric point [127]. The EDL thinning and distortion mechanism proposes that for particles moving in a stationary liquid, their diffuse double layers would distort and tail out behind it. This distortion is further promoted by the attraction of the ions in the EDL to the other electrode in the system. The distortion results in diffuse double layer thinning ahead and to the equator of the moving particles, reducing its zeta potential [128]. The particle neutralisation mechanism is rejected as the main cause for deposit formation and the most developed theories considers that deposit formation is due to EDL distortion and thinning during electrophoresis followed by the coagulation of particles under the influence of the externally applied electric field [129].

2.9 Parameters of EPD

There are various factors that influence the EPD process. Two types of parameters can be distinguished that determine the characteristics of the EPD process: (i) those related to the process and (ii) those related to the suspension. Parameters related to the process include the effect of deposition time, applied voltage, concentration of the solid in suspension and the conductivity of the substrate. Parameters related to the suspension include particle size, dielectric constant of the solvent, conductivity of the suspension, viscosity of the suspension, zeta potential and stability of the suspension. [107, 129, 130]. At the submicron or nanometer particle size scale, surface chemistry or surface properties, controls the processing behaviour of the particles in the suspension. It is important to understand and manipulate the surface phenomena to control the processing conditions and to achieve more desirable products [111].

2.9.1 Applied voltage

In EPD, strong electric fields are required to ensure sufficiently rapid movement of colloidal particles and consequently reasonable deposition times from sufficiently dilute suspensions. The electric field ($\mathbf{E}$) in the suspension is related to the conductivity (k) of the suspension and current density (J) which is basically a microscopic formulation (Eq. (2.16)) of Ohm's law [114]:

$$J = k\mathbf{E} \tag{2.16}$$

In constant voltage EPD, the potential between the electrodes is constant however because deposition requires a steeper potential gradient than electrophoresis, with increasing deposition (i.e. increasing electrical resistance), the potential inducing electrophoresis ($\mathbf{E}$, voltage drop/cm in the suspension) decreases and particle motion also decreases. Particle deposition becomes zero if $\mathbf{E}$ is too flat. Under constant current EPD, the voltage drop/cm ($\mathbf{E}$) is maintained constant by increasing the total potential drop between the electrodes. Constant current EPD avoids limited deposition and deposition rate problems of constant voltage EPD [113].

2.9.2 Deposition time

Deposition is linear during the initial stage of EPD however as more time is allowed the deposition rate decreases and attains a plateau for long deposition times. In constant voltage mode, the potential between the two electrodes are kept constant however the electric field strength will decrease due to the resistance introduced by the formed deposit on the electrode surface [107].

39

2.9.3 Solid concentration

Radice *et al*. [116] studied the role of the particle concentration during EPD and observed that a threshold concentration value exists where deposition would occur. Below the threshold concentration value, no deposited mass was detected and the proportionality between the concentration and deposited mass did not follow the Hamaker formula (Eq. (2.15)). Below the threshold concentration value, no deposit growth occurred even with higher applied voltages and longer EPD durations. The flux of particles depositing onto the substrate can be controlled by adjusting the solid concentration [131].

2.9.4 Substrate conductivity

The quality of the deposit formed by EPD can be affected by the uniformity and conductivity of the substrate. Talebi *et al*. [119] studied the effect of substrate conductivity by depositing on a non-conducting substrate as well as a conducting substrate. They observed deposit formation on both substrates however they noticed significant differences in the quality of the deposits. The non-conductive substrate showed significant crack formation and the deposit showed low adhesion strength to the substrate in comparison to the conductive substrate which formed a uniform deposit with high adhesion strength. Significantly higher deposition weights were obtained for the conductive substrate compared to the non-conductive substrate. Besra *et al*. [121] observed that it was only possible to deposit onto the non-conducting substrate (NiO-YSZ) when the porosity of the substrate was above a certain threshold value which was dependent on the applied voltage. No deposition was possible when the substrate porosity was below the threshold value.

2.9.5 Particle size

It is important that particles remain well dispersed over the full duration of EPD. Larger particles tend to sediment due to gravity and result in non-uniform deposits. Smaller particles are most suitable to form stable suspensions for EPD and to obtain homogeneous deposits. In general, EPD can be applied to any solid (< 30 μm) that is in a fine powder form or in a colloidal suspension [27]. For clay and ceramic systems, good deposition were reported for particle sizes in the range of 1 to 20 μm [107]. Suspension pH and temperature influences particle size [101].

2.9.6 Suspension viscosity

In EPD, low particle concentrations are required and the viscosity of the dispersant cannot be used to determine the dispersion state of the particles. It is desirable to have a suspension with a low viscosity. Zeta potential and suspension conductivity should be used to study the suspension [107, 132].

2.9.7 Suspension conductivity

When the suspension conductivity is too low, particle motion is slow and when the conductivity of the suspension is too high the particles charge electronically and stability is lost [107, 132].

2.9.8 Dielectric constant of the dispersant solvent

When the dielectric constant of the dispersing solvent is too low, deposition fails due to insufficient dissociative power. When the dielectric constant of the dispersing solvent is too high, the high ionic concentration reduces the size of the EDL region

and consequently the electrophoretic mobility [107]. Water ($\varepsilon \approx 78.3$) has a much higher dielectric constant in comparison to IPA ($\varepsilon \approx 18.2$) at 25°C. Cihlar *et al.* [133] observed that the zeta potentials of Al_2O_3 and ZrO_2 particles in IPA (under acidic and basic conditions) were opposite in charge compared to when the particles was studied in water (acidic and basic conditions). They explained this behaviour by the low dissociation of acids and bases in IPA.

2.9.9 Suspension stability

The first step in EPD is to prepare a stable suspension of independent particles [134]. The suspension should remain stable for the entire duration of deposition. The morphology of the deposited layer is directly affected by the stability of the suspension. Suspension stability is characterised by the particle settling rate and the tendency for the particles to undergo or avoid flocculation [107, 135]. Stable suspensions have no or very low tendency to sediment or flocculate. The addition of excess acid or base is disadvantageous as the un-adsorbed ions compress the EDL and affects the suspension stability. Free ions can become the majority of charge carriers during EPD and the transport number of the charged particles drops which affects the deposition rate of the particles resulting in thin deposited layers. The addition of excess binders can also negatively affect the stability of the colloidal suspension and lead to poor deposition of the particles. Excess binders also affect the quality of the deposited layer therefore the optimum binder content should be determined [112].

2.9.10 Zeta potential

Particles in a solution become surrounded by ions of opposite charge in a higher concentration than the bulk concentration of these ions, to form the EDL. Under the

influence of an externally applied electric field, the particle and ions should move in opposite directions however the ions are also attracted by the particle (i.e. some of the ions will move along with the particle). Particle mobility is thus not determined by the surface charge however it is determined by the net charge enclosed in the liquid sphere which moves along with the particle. The potential at the surface of shear is known as the zeta potential [96]. Zeta potential plays an important role in stabilising the suspension and determining the direction and migration velocity of the particles. Zeta potential plays an important role in many applications such a ceramics, food preparation, agriculture, paper industry, pharmaceuticals, paints, coatings and photographic emulsions. Zeta potential also plays an important role in waste water treatment, environmental transport of nutrients, sol-gel synthesis, mineral recovery and corrosion processes [108]. Zeta potential has become the standard parameter to describe the surface charge of colloidal particles suspended in a liquid. The zeta potential is calculated from the electrophoretic mobility of the particles, which is assumed to be colloidal, hard and spherical. Both zeta potential and electrophoretic mobility measurements incorporate interactive effects from the suspending medium and additives, such as excess deflocculants and charging agents [136]. The general dividing line between stable and unstable suspensions is taken as +30 mV or -30 mV. Particles with zeta potentials more positive than +30 mV or more negative than -30 mV are generally considered stable. Suspension pH and temperature influences particle zeta potential [101].

2.10 Electrokinetic phenomena

According to the classical description of colloidal suspensions, the zeta potential is the main parameter to determine the dielectric and electrokinetic properties of the

colloidal suspension. The zeta potential is obtained experimentally through electrophoretic mobility measurements and using the Standard Electrokinetic Model. According to the Standard Electrokinetic Model, the colloidal particles in suspension are surrounded by a uniform surface density of fixed charge. The ions in the electrolyte solution are treated as mathematical points and the macroscopic values of permittivity and viscosity remain valid at the microscopic scale up to the surface of the particle. Under these assumptions the equilibrium distributions of ions around a suspended particle coincides with the Gouy-Chapman distribution, the zeta potential coincides with the electric potential at its surface and the surface conductivity coincides with the conductivity of its diffuse double layer. The surface conductivity is thus a function of the zeta potential and other parameters of the Standard Electrokinetic Model such as the ion concentrations in the electrolyte solution far from the particle, its valences, diffusion coefficients and the fluid viscosity. The dielectric and electrokinetic properties of the system would thus be functions of a series of known parameters and a single variable i.e. the zeta potential [137, 138]. Zukoski *et al.* [139] studied the electrokinetic properties of two monodispersed colloidal systems by means of electrophoretic mobility, electrical conductivity measurements and the Standard Electrokinetic Model. The two zeta potentials obtained were substantially different which raised doubts to the completeness of the Standard Electrokinetic Model. It also meant that a single parameter, i.e. the zeta potential cannot fully characterise the electrokinetic transport properties of some colloidal particles. The Standard Electrokinetic Model assumes surface smoothness on a molecular level and thus cannot be universal. The requirement of homogeneous, smooth and impervious surfaces can only be satisfied by properly selected systems e.g. emulsion droplets in water, silver iodide crystals, partially fused molecularly

smooth quarts, mica, etc [140]. Porous and rough surfaces are abundant however it does not correspond to the Standard Eelectrokinetic Model [141]. Recent advances in the theory of electrokinetic phenomena demonstrated that electrokinetic effects are not only determined by the zeta potential but by other parameters of the EDL as well. The occurrence of ionic motions in the inner part of the EDL has particularly received increasing interest. Neglecting the Stagnant Layer Conductivity (SLC) has in several cases been found to cause considerable error in the estimation of zeta potential from electrokinetic experiments [140]. The common method to overcome the difficulties faced by the Standard Electrokinetic Model is to consider that the particle surface is more complex than assumed by the model. It can be considered that the particle is surrounded by a thin layer where the ion density is determined by adsorption isotherms or the particle surface is rough or hairy so that both fixed charges and free ions populate the surface layer. These generalisations may solve some of the deficiencies of the Standard Electrokinetic Model however it may also worsen the interpretation of the experimental data for high electrophoretic mobility values [138].

Chapter 3: Experimental method

3.1 Materials

HiSpec 4000, 40 wt% *Pt/C* (Johnson Matthey, United Kingdom) was used as received as catalyst material for all experiments. A 5 wt% Nafion® solution (Johnson Matthey, United Kingdom) was used as received as a binder and ionomer. A 60 wt% PTFE solution (Electrochem, USA) was diluted with Ultra-Pure (UP) water ($R = 18.3M\Omega$) to obtain a 20 wt% PTFE solution and was used as a binder. UP water was obtained using the Zeneer Power III (Human Corporation, South Korea) water purification system. UP water and IPA (Kimix, South Africa) were used a dispersing medium for the preparation of the catalyst suspensions. *$HClO_4$* and *NaOH* (Kimix, South Africa) were used to adjust the pH of the catalyst suspensions. *NaCl* (Kimix, South Africa) was used to prepare catalyst suspensions with various salt concentrations. A commercially available GDL, H2315 CX196 (Freudenberg, Germany), was used as received. A commercially available ABPBI membrane, Fumapem® AM (Fumatech, Germany), was doped in PA (Kimix, South Africa) be use.

3.2 Zeta potential and particle size

Electrophoretic mobility and size of the *Pt/C* nano-particles were measured *via* the Zetasizer Nano ZS (Malvern Instrument Ltd., United Kingdom). **Fig. 3.1** shows an image of the Zetasizer Nano ZS instrument. The Zetasizer Nano ZS was fitted with a production standard 532 nm, 50 mW diode laser source. Electrophoretic mobility was measured *via* a 3M-PALS method which is a combination of Laser Doppler Velocimetry (LDV) and Phase Analysis Light Scattering (PALS). An electric field is applied to a solution containing dispersed particles which will move at a velocity

related to its zetapotential. This particle movement enables the instrument to calculate the electrophoretic mobility. The instrument then calculates the zeta potentials (ζ_{exp}) from the measured electrophoretic mobility *via* the Smoluchowski formula (See Chapter 6). Particle size was also obtained *via* the Zetasizer Nano ZS through a Dynamic Light Scattering (DLS) technique. DLS is a well-established optical technique used to study dynamic processes of liquids and solids. When a scattering medium is in motion, the light that it scatters will fluctuate with time. The intensity of this scattered light is measured and its temporal fluctuations are quantified to characterise the underlying motion [142]. The Zetasizer Nano ZS converts the motion of particles to size and size distribution using the Stokes-Einstein relationship. An advantage of DLS is that it can be used in-situ to study particle aggregation [143].
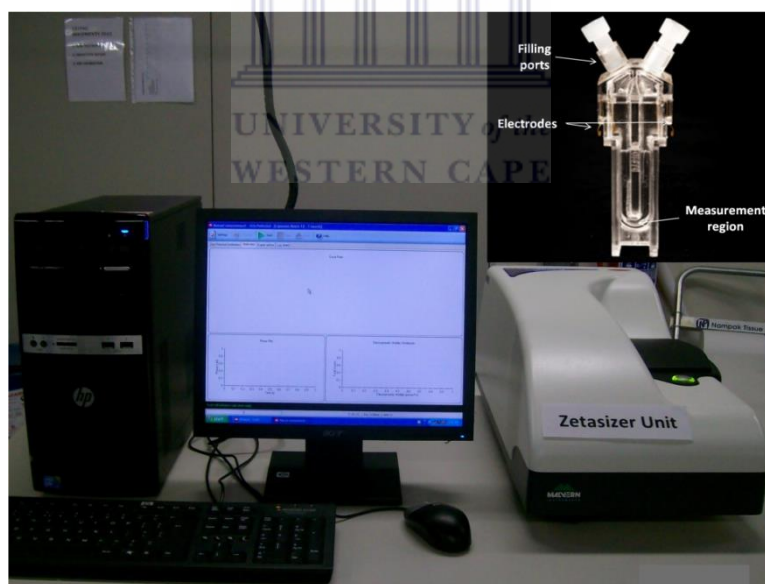
Figure 3.1: Zetasizer Nano ZS and a semi-disposable capillary cell (insert).

3.3 Catalyst suspensions

3.3.1 Organic suspensions

Organic suspensions were obtained by ultrasonically (20 kHz) mixing the *Pt/C*, Nafion® ionomer or PTFE and IPA for 5 minutes *via* the Biologics 3000 (Biologics, Inc., USA) ultrasonic homogeniser fitted with a micro tip ultrasonic finger. The Nafion® ionomer content studied was 15 and 30 wt% with respect to the *Pt/C* catalyst whereas the PTFE content was varied between 0 and 50 wt% with respect to the *Pt/C* catalyst. The pH of the catalyst suspensions were adjusted between 2 and 12. The salt concentrations that were studied were between 0 and 0.5mM. The power of the homogeniser was set at 40% with the pulser set to the *off* position (0%). The pH of the suspensions was monitored using the Metrohm 827 pH lab equipped with a Primatrode pH electrode. The electrophoretic mobility of each sample was obtained by averaging 3 values measured at 100 V. The particle size was measured *via* the Zetasizer Nano ZS by averaging 10 size values obtained over a 600 s time interval with a measurement recorded every 60 s. Each sample was repeated thrice for reproducibility. All measurements were performed at 25°C.

3.3.2 Aqueous suspensions

Homogeneous aqueous catalyst suspensions were obtained by ultrasonically (20 kHz) mixing *Pt/C*, UP water and *HClO₄*, *NaOH* or *NaCl* for 5 minutes *via* the Biologics 3000 ultrasonic homogeniser. The pH of the catalyst suspensions were adjusted between 2 and 13. The salt (*NaCl*) concentrations studied ranged between 0 and 40mM. The power of the homogeniser was set at 40% with the pulser set to the *off* position (0%). The pH of the suspensions was monitored using the Metrohm 827 pH

lab equipped with a Primatrode pH electrode. Zeta potential and size was obtained similarly to the organic suspensions.

3.4 Fabrication of GDEs and MEAs

3.4.1 EPD method

For the fabrication of GDEs, only organic catalyst suspensions were used. Catalyst suspensions were obtained by ultrasonically (38 kHz) mixing *Pt/C*, Nafion® ionomer or PTFE, UP water and IPA using an ultrasonic bath (Grant Instruments, United Kingdom) for 15 and 30 minutes for the *Pt/C*/Nafion® and *Pt/C*-PTFE suspensions respectively. UP water was added in a ratio 2:1 to the *Pt/C* catalyst to prevent chemical reaction of the active *Pt* with the IPA. The *Pt/C* compositions were 0.5 and 2 mg/ml of IPA for the *Pt/*C-Nafion® and *Pt/*C-PTFE suspensions respectively. The Nafion® ionomer content was varied from 10 to 30 wt% while the PTFE content was varied between 10 to 50 wt% with respect to the *Pt/C* content. The pH of the *Pt/C*-Nafion® suspensions was adjusted to improve suspension conductivity. The ionic strength of the *Pt/C*-PTFE suspensions was adjusted to improve the suspension conductivity. A microelectrophoresis power supply (Consort, Belgium) was used to deposit the catalyst particles onto the GDLs by varying the applied electric field strength and EPD duration.

An *in-house* EPD cell was constructed and used for GDE fabrication. **Fig. 3.2** shows a schematic diagram of the *in-house* EPD cell.
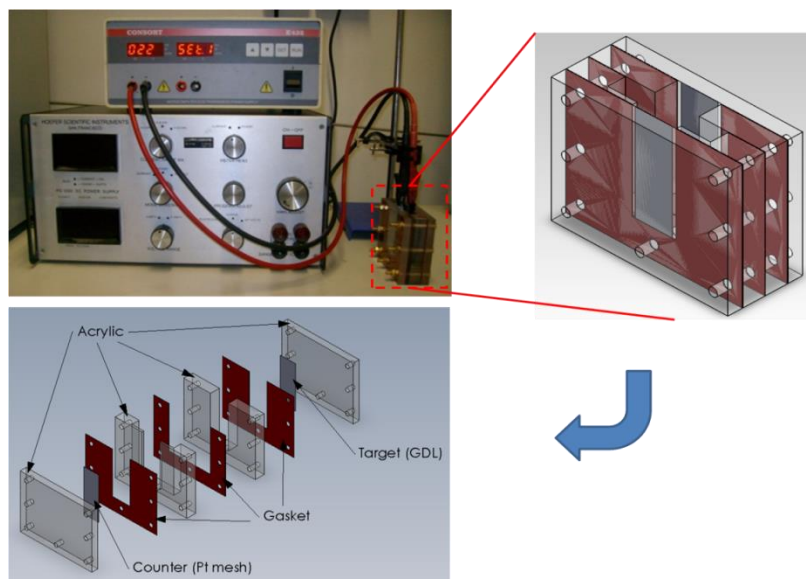
Fig. 3.2: Schematic diagram of the EPD setup and cell.

This cell construction allowed fixing the distance between the working and counter electrode to 1.8 cm. It is important to reduce the distance between the working and counter electrode as greater distances requires higher electric field strengths which lead to a more energy intensive process and higher process costs. The obtained GDEs were placed in a vacuum oven (Binder GmbH, Germany) at ambient temperature and heated to 50°C (~1.5°C/min) to dry the CL. Heat treatment of the GDEs were performed at 340°C under *Ar* atmosphere. Heat treatment of the GDEs was performed by heating the furnace to 340°C within ~1 hour followed by maintaining 340°C for 30 minutes and then cooling the furnace to room temperature without artificial cooling. The ABPBI membrane was doped in PA for 24 hours at 85 and 130°C for the MEAs containing the Nafion® ionomer and PTFE respectively. The MEAs were obtained by sandwiching the anode and cathode GDEs and the acid doped membrane together inside a single cell fixture. All GDEs and MEAs prepared *via* the EPD method are referred to as EPD GDEs and EPD MEAs respectively from this point on.

3.4.2 Hand spray method

MEAs fabricated *via* a hand spray method was used as a comparison to the EPD MEAs containing the Nafion® ionomer in the CLs. Catalyst inks were obtained *via* ultrasonically (38 kHz) mixing *Pt/C*, Nafion® ionomer, UP water and IPA for 60 minutes. UP water was added in a ratio 2:1 to the *Pt/C* catalyst to prevent chemical reaction of the active *Pt* with the IPA. The *Pt/C* composition was 13.5 mg/ml of IPA with 20 wt% Nafion® ionomer. A spray gun (Prona RH-CP, Taiwan) with nitrogen as carrier gas was used to spray the catalyst particles onto the GDL. The CLs were dried *via* a warm air blower (Russell Hobbs, United Kingdom) between each deposited layer. GDEs fabricated by the hand spray method were assembled and evaluated in a similar way to the EPD GDEs. The MEAs were obtained by the same procedures as for the EPD MEAs. All GDEs and MEAs prepared *via* the Hand Spray (HS) method are referred to as HS GDEs and HS MEAs respectively from this point on.
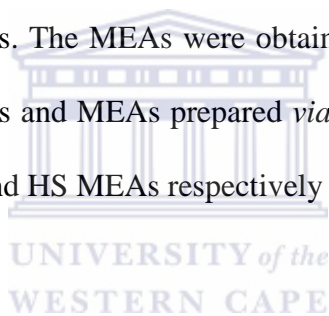
3.4.3 Ultrasonic spray method

MEAs fabricated *via* an ultrasonic spraying method were used as a comparison to the EPD MEAs containing PTFE in the CLs. Catalyst inks were obtained *via* ultrasonically (38 kHz) mixing *Pt/C*, PTFE solution, UP water and ethanol for 30 minutes. UP water was added in a ratio 2:1 to the *Pt/C* catalyst to prevent chemical reaction of the active *Pt* with the ethanol. The catalyst ink was loaded into the ultrasonic sprayer (Sono-tek Corporation, USA) then sprayed onto the GDLs. A hot plate heated to 80°C was used to continuously dry the deposited CLs during the spraying process. The ultrasonic nozzle operated at 120 kHz and an ultrasonic power of 3 W. The heat treatment procedures were the same as for the EPD GDEs. MEAs were obtained by the same procedures as for the EPD MEAs. All GDEs and MEAs

prepared *via* the ultrasonic spray method are referred to as Sonotek GDEs and Sonotek MEAs respectively from this point on.

3.5 Physical characterisation methods

3.5.1 High Resolution Scanning Electron Microscopy

Morphology of the GDE/MEAs were characterised by High Resolution Scanning Electron Microscopy (HR-SEM) using the Nova NanoSEM 230 (FEI, USA) working at 20kV and the Auriga HRFEGSEM (Carl Zeiss, Germany) working at 5 kV.

3.5.2 Mercury Intrusion Porosity

Mercury Intrusion Porosity (MIP) analysis of the GDEs was obtained *via* the Autopore IV 9510 (Micromeritics, USA) by applying pressures between 0.0145 to 4136.85 bar. Intrusion of mercury into pores of different sizes occurs at different pressures. At low pressures, mercury moves into the larger pore diameters while at low pressures, mercury is forced into the smaller pore diameters. By applying a pressure range from low to high pressure values, the porosity of the sample is obtained.

3.6 Electrochemical characterisation of MEAs

3.6.1 Apparatus

An *in-house* HT-PEMFC test bench was used to evaluate the electrochemical performance of the MEAs. The *in-house* HT-PEMFC test bench consisted of a personal computer installed with Labview software to control the electronic load (Höcherl & Hackl GmbH, Germany) and mass flow controllers (Bronkhorst,

Netherlands). A cell compression unit (Pragma Industries, France) controlled the cell pressure and temperature. All measurements were performed at 160°C and a cell compression pressure of 20 bar with dry air (1 slpm) and dry hydrogen (0.5 slpm).

3.6.2 Polarisation and stability studies

The MEAs were activated for 3 hours at 0.55 V followed by measuring the polarisation curve between open circuit voltage (OCV) and 0.2 V. Stability of MEAs were performed at 0.55 V.

3.6.3 Electrochemical Impedance Spectroscopy

Electrochemical Impedance Spectroscopy (EIS) is an electrochemical technique in which a cell is perturbed by applying a signal of small magnitude. EIS allows observing the way the system follows the perturbation at steady state. During EIS, the impedance of a cell can be measured as a function of the frequency of an AC source. EIS is capable of high precision and is frequently used for the evaluation of heterogeneous charge transfer parameters and for studies of double layer structure [144]. EIS is a powerful technique to characterise the kinetics of an electrode-electrolyte interface. EIS is well established in PEMFC diagnostics and is also applicable to HT-PEMFCs [46]. The Autolab PGSTAT302N (Metrohm, Netherlands) was used for EIS analysis of the MEAs in a frequency range of 0.1 to 50,000 Hz.

3.6.4 Cyclic Voltammetry

CV is an extremely powerful technique and is amongst the most commonly used electrochemical methods. During CV, information about the analyte is obtained by measuring the current response as a function of the applied potential. The resultant

plot of current against potential is termed a voltammogram. The potential is ramped at a scan rate (υ) from an initial potential (E_i) to a final potential (E_f) however then the potential is reversed, usually stopping at E_i (or it may continue for additional cycles). The potential at which the scan is reversed is known as the switch potential (E_λ) [145]. In PEMFCs, CV is used to determine the electrochemical surface areas of the electrodes. CV is performed by passing ultra-high purity hydrogen and ultra-high purity nitrogen over the anode and cathode respectively [46]. The Autolab PGSTAT302N was used for CV analysis which was performed by cycling the potential between 0.02 to 0.8 V at a scan rate of 50 mV/s. **Fig. 3.3** shows images of some of the test equipment used to characterise the MEAs.
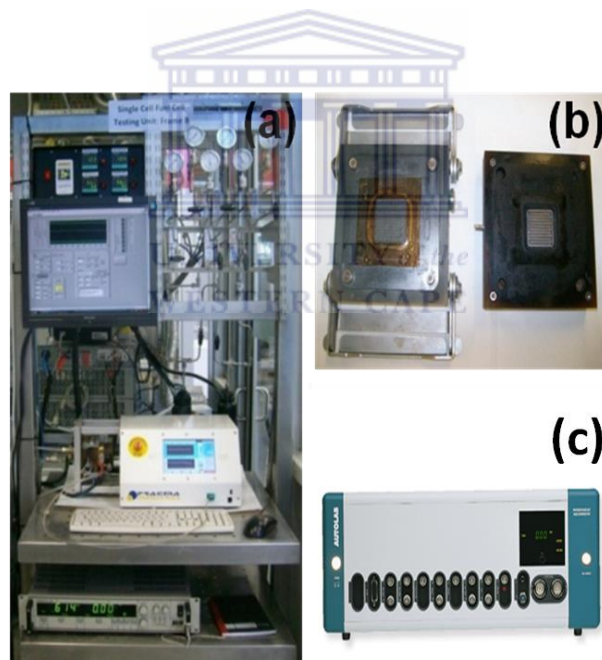
Fig. 3.3: Images of (a) *in-house* **HT-PEMFC test bench (b) high temperature single cell (c) Autolab PGSTAT302N.**

Chapter 4: EPD of Pt/C-Nafion® nano-particles for fabrication of GDEs/MEAs

4.1 Introduction

Catalyst layers (CL) with extensive, high density Triple Phase Boundary (TPB) distributions are important to maximise Pt utilisation. The TPB concept holds that electrochemical reactions (i.e. ORR and HOR) can only occur at confined spatial regions where the proton conducting electrolyte, reactant gases and the electrically connected catalyst particles are in contact [146]. The addition of the Nafion® ionomer to the *Pt/*C particles is common place when preparing catalyst suspensions for the fabrication of MEAs for LT-PEMFCs. The Nafion® ionomer is added to improve TPB formation and the bonding of the CL to the GDL or membrane. It is also important to optimise the electrolyte ionomer content incorporated into the CLs to maximise TPB formation and obtain good MEA performance[147].
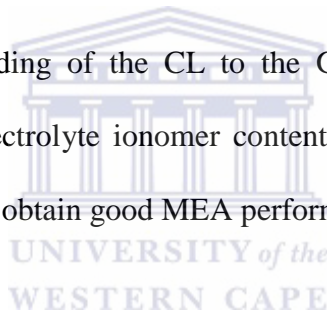
Organic alcohols are commonly used as dispersing solvents to prepare the catalyst suspensions. Thus catalyst suspensions comprising of IPA, the *Pt/C* catalyst and the Nafion® ionomer were studied *via* the Zetasizer Nano ZS to obtain stable catalyst suspensions for the EPD method. The optimum catalyst suspensions were used to fabricate GDEs *via* the EPD method. The obtained EPD GDEs/MEAs were characterised by physical methods (i.e. HR-SEM and MIP) and electrochemical methods (i.e. polarisation measurements and EIS). The best performing EPD MEA was compared to a MEA fabricated *via* the conventional hand spraying method.

4.2 Results and Discussion

4.2.1 Catalyst suspension characterisation

Fig. 4.1 shows the sizes of the *Pt/C*-Nafion® particles obtained after ultrasonically mixing for various time intervals. The particle sizes varied between 235 to 250 nm for the ultrasonic time intervals of 5 to 30 minutes. The smallest particle sizes were observed for an ultrasonic time between 10 to 15 minutes. The ultrasonic time of 15 minutes was selected for preparing well dispersed catalyst suspensions for GDE fabrication.
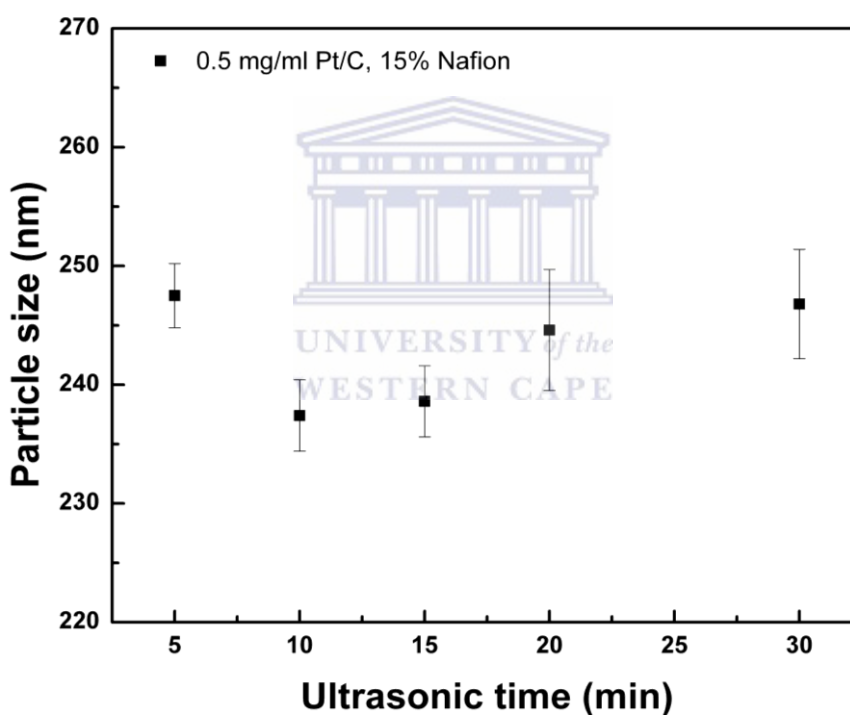
Fig. 4.1: Size of *Pt/C*-Nafion® particles vs. ultrasonic time.

Stable catalyst suspensions are important for the formation of homogeneous catalyst deposits. The overall stability of the suspension depends on the interaction between individual particles. Interactions between particles are affected by two mechanisms namely the electrostatic and Van Der Waals forces. A high electrostatic repulsion due

to a high particle charge is required to avoid particle agglomeration [107]. Stable suspensions suitable for successful EPD are those that contain particles that have a high zeta potential while maintaining a low ionic conductivity. Controlling particle size is also important as larger particles tend to sediment due to gravity. **Fig. 4.2** shows the zeta potentials (ζ_{exp}) of the *Pt/C* and *Pt/C*-Nafion® particles between pH 2 and 12.
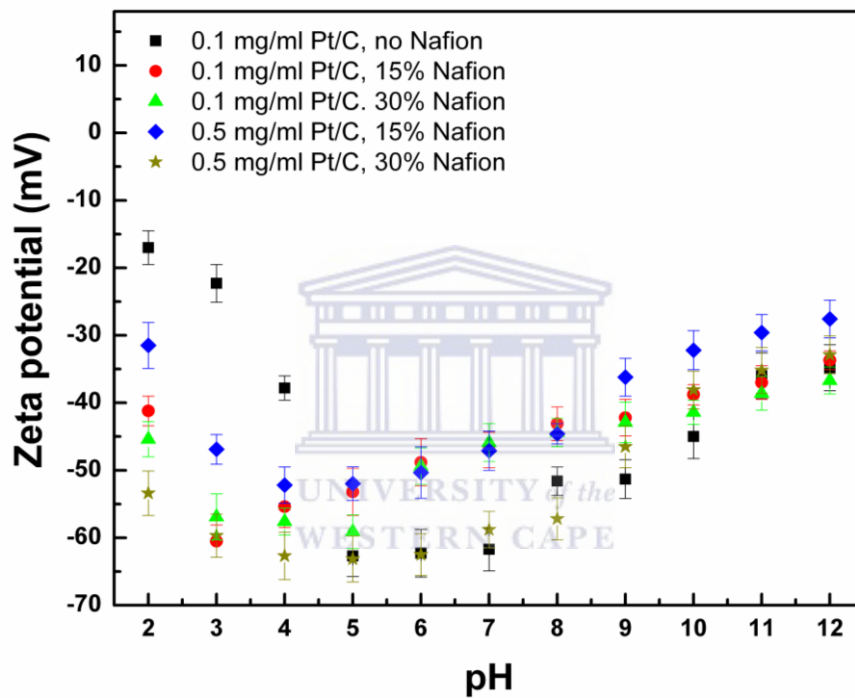
Fig. 4.2: Zeta potential of *Pt/C* and *Pt/C*-Nafion® particles vs. suspension pH.

For stable suspensions, zeta potentials that are more positive than +30 mV or more negative than -30 mV depending on the particle sign, is recommended. The isoelectric point occurs when the particles have a zeta potential of 0 mV however no isoelectric point was observed over the whole pH range studied. At zeta potentials of 0 to ±10 mV, particle coagulation or flocculation occurs rapidly and particles would either sediment to the bottom or float on top of the solution. The zeta potentials from ±10 to ±30 mV indicate incipient instability. For the *Pt/C* particles in IPA, low zeta

potentials were observed at pH 2 and 3 thus unstable suspension behaviour was expected. Highest zeta potentials were observed between pH 5 and 7 followed by decreasing zeta potentials as the pH was increased to more basic pH values. Suspensions containing the *Pt/C*-Nafion® particles have higher zeta potentials than the *Pt/C* particles in the acidic range (i.e. pH 2 to 4) but similar or lower zeta potentials from pH ~ 5 to 12.

Fig. 4.2 shows that higher zeta potentials were obtained as the Nafion® ionomer content was increased. Comparing the results in **Fig. 4.2** to that reported by Louh *et al.* [31], a similar trend for the *Pt/C*-Nafion® particles were observed. For the *Pt/C* particles however, they observed a continual increase of the zeta potential as the suspension was increased to pH 12. **Fig 4.3** shows the size of the *Pt/C* and *Pt/C*-Nafion® particles between pH 2 and 12. By examining the particle size results in **Fig. 4.3**, a clear relation can be made between the zeta potential and particle size. For the *Pt/C* particles in IPA where the zeta potentials were the lowest (i.e. at acidic pH 2 to 4 and basic pH 11 to 12) the particle size showed significant increase due to particle coagulation. The size for the *Pt/C*-Nafion® particles were stable over the whole pH range studied which clearly demonstrated the steric stabilisation effect of the Nafion® ionomer. Even at higher *Pt/C* concentrations, no significant changes in particle size were observed when the Nafion® ionomer was present. The Nafion® ionomer acts as
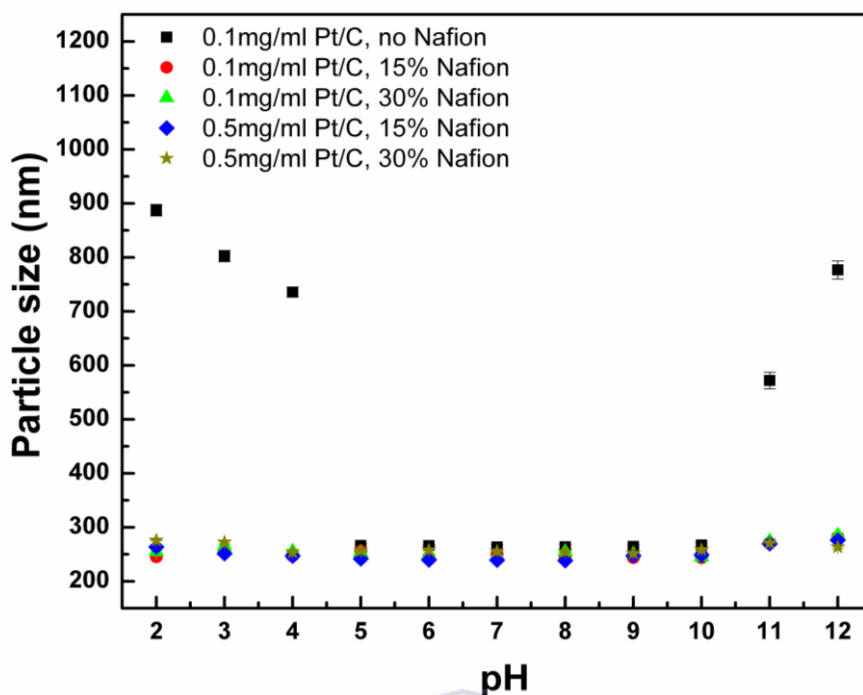
Fig. 4.3: Size of *Pt/C* and *Pt/C*-Nafion® particles vs. suspension pH.

a surfactant as well as an active component of the CL structure. The Nafion® ionomer is an amphiphilic polymer consisting of a hydrophobic fluoro-backbone and a hydrophilic sulphonic acid group which is readily ionised and negatively charged to impart an electrostatic force on the *Pt/C*-Nafion® particles [148]. As the *Pt/C*-Nafion® particles approach each other; the sulphonic acid side chains oppose attraction causing steric repulsion due to the unfavourable decrease in conformational entropy. Colloidal surfaces are maintained at distances large enough to damp any attractions due to the depletion effect or London-Van der Waals forces and the colloidal suspension is stabilised [149]. Sterically stabilised systems tend to remain stable even at high salt concentrations [150] and conditions were the zeta potentials of the surfaces are reduced to near zero.

Besides high values of particle zeta potential, sufficient suspension conductivity is also crucial for the EPD process. When the suspension conductivity is too high the particle motion is very low. When the conductivity is too low the suspension becomes too resistive and the particles become electronically charged and stability is lost [107]. A suspension pH of 9 was selected to fabricate the GDEs as it provided sufficient ionic conductivity for the fabrication of GDEs *via* EPD.

Fig. 4.4 shows the particle sizes obtained after subjecting the *Pt/C*-Nafion® particles to an externally applied electric field of 100 V/cm for various time intervals between 5 and 30 minutes. The particle sizes varied between 245 and 263 nm for the time intervals studied. The small increase in particle size should not be a significant obstacle for the EPD process as it is selective toward particle size. The result implied that particle coagulation was slow even when an external electric field was applied and that the particle size will not be significantly affected from the beginning to the end of the EPD duration.
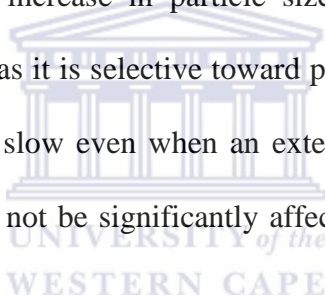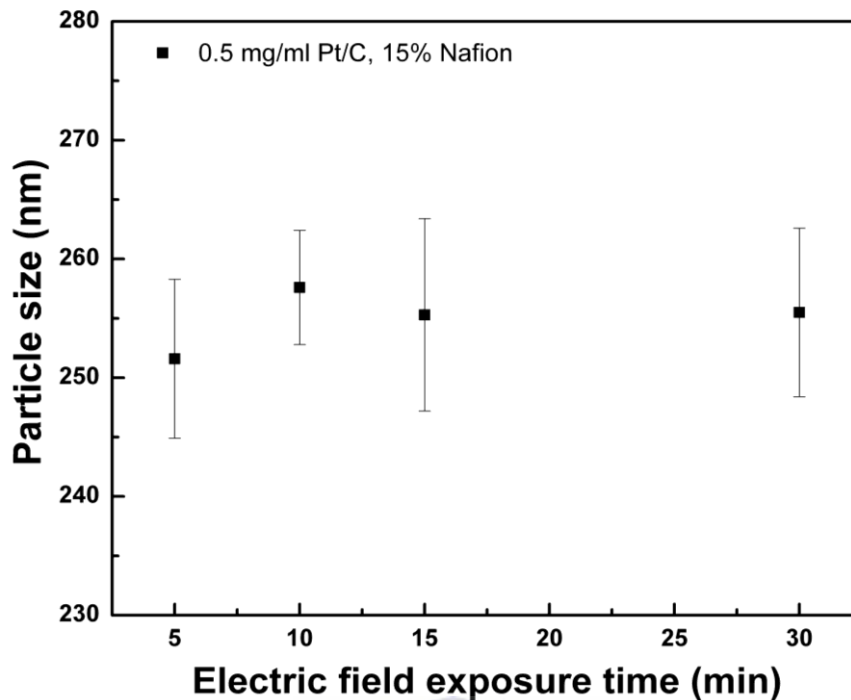
Fig. 4.4: Size of *Pt/C*-Nafion® particles vs. electric field exposure time.

4.2.2 GDE/MEA fabrication and physical characterisation

The driving force for the catalyst particle movement is the strength of the externally applied electric field; the higher the externally applied electric field strength the faster the particles will move toward the target substrate. The strength of the externally applied electric field should also be sufficiently high to overcome the viscous drag and other forces exerted by the counter ions surrounding the particles. **Fig 4.2** shows that the particles were negatively charged over the entire pH range studied and would therefore deposit onto the positively charged electrode. To obtain the desired *Pt* loadings, a calibration curve for the *Pt* loading as a function of the externally applied electric field strength and deposition time was constructed and is shown in **Fig. 4.5.** It is clear from the calibration curve that the catalyst particles were deposited more rapidly as the strength of the externally applied electric field was increased. The

increase of the *Pt* loading was not linear due to the increase of resistance as the CL thickened [32, 107].
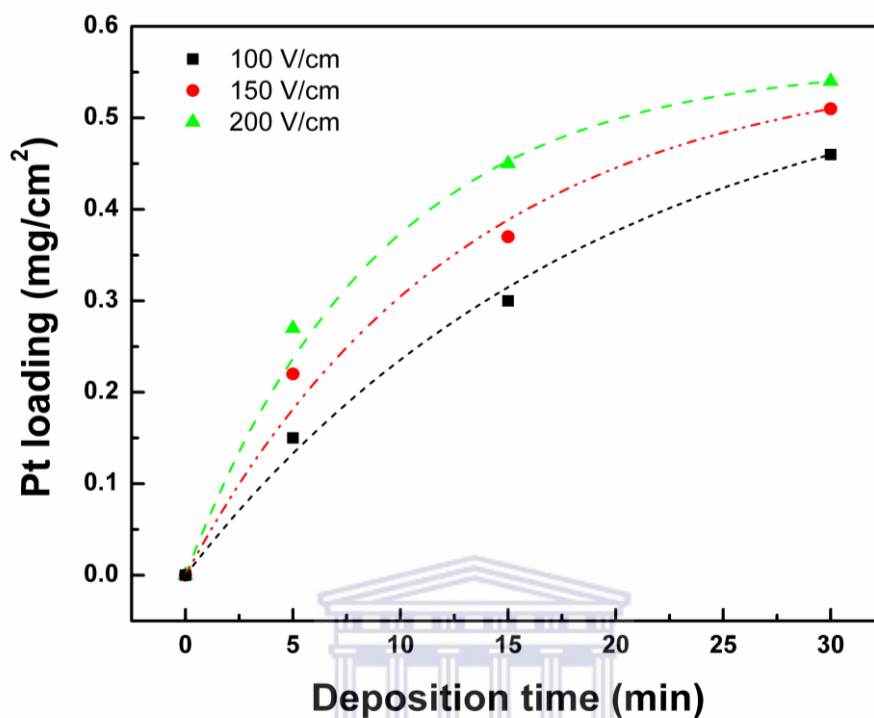
Fig. 4.5: Calibration curve for *Pt* loading at various applied electric field strengths and deposition time.

Based on the calibration curve, the *Pt* loadings were fixed at 0.4 mg/cm^2 for both the anode and cathode GDEs. **Figs. 4.6 a** to **c** show the HR-SEM images of EPD GDEs fabricated at various applied electric field strengths while **Fig. 4.6 d** shows the HR-SEM image of the HS GDE. The Nafion® ionomer content was fixed at 20 wt% with respect to *Pt/C* particles for all the GDEs. At 50,000 x magnification (insert pictures), no significant differences between the EPD GDEs and the HS GDE were observed.
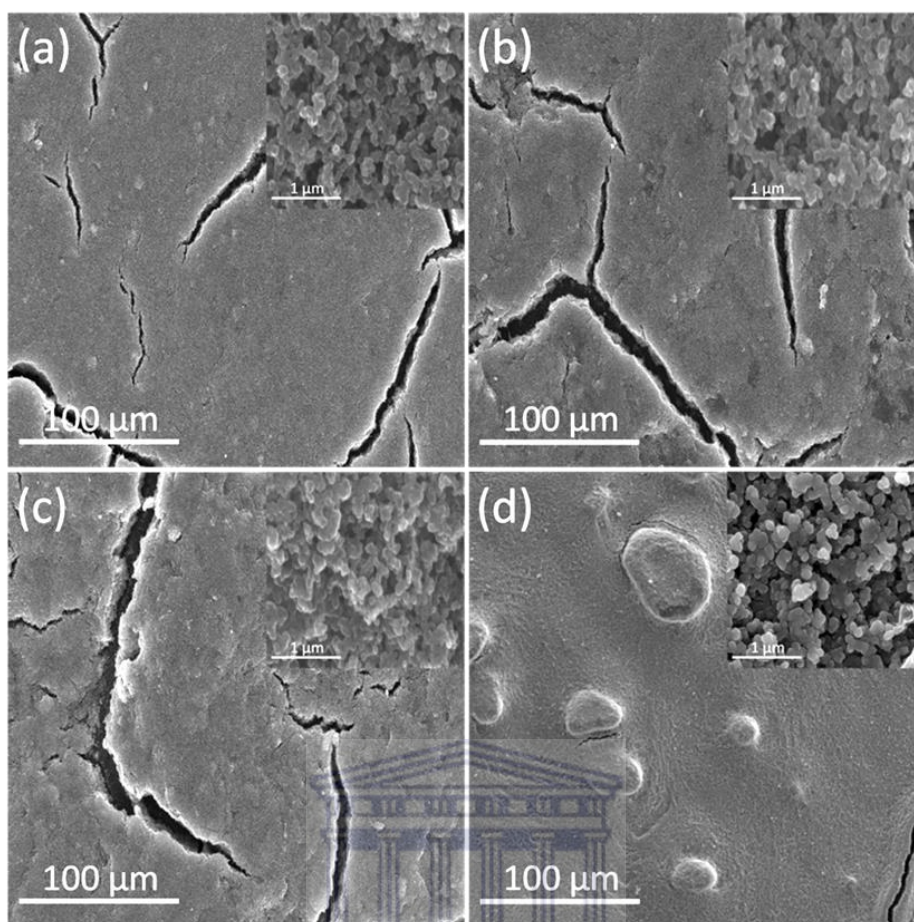
Fig. 4.6: HR-SEM images of (a) EPD GDE (100 V/cm), (b) EPD GDE (150 V/cm), (c) EPD GDE (200 V/cm) and (d) HS GDE. All CLs contained 20 wt% Nafion® ionomer and 0.4 mg/cm² Pt loading.

All GDEs showed porous morphologies which are important to ensure that reactant gases effectively diffuse to the active *Pt* sites. At 1,000 x magnification, the morphologies of the GDEs fabricated by the two methods were significantly different. The HS GDE exhibit minor cracks and large catalyst lumps. The morphologies of the EPD GDEs were dominated by cracks while no catalyst lumps were observed. The absence of large catalyst lumps could be due to the use of more dilute catalyst suspensions during EPD (i.e. 0.5 mg/ml for the EPD method compared to 13.5 mg/ml for the hand spray method) resulting in more uniformly dispersed catalyst suspensions. The crack dominated morphologies of the EPD GDEs were caused by

63

drying the relative thick CLs (i.e. ~11.5 μm) in a single step. Cracks are formed due to the evaporation of the solvent from the CL. Fine cracks are regarded as beneficial for CL morphologies as it provides gas access to the reaction sites close to the membrane and increases catalyst utilisation [97].

Figs. 4.7 a and **b** show the back scattered images of the EPD GDE (100 V/cm) and the HS GDE respectively. The EPD GDE exhibits better dispersion of the *Pt* particles (the bright reflective particles) than the HS GDE which promotes TPB formation. The better dispersion of the *Pt* particles in the EPD GDE was probably a result of using a more dilute and stable catalyst suspension. **Figs. 4.7 c** and **d** show the cross sectional views of the EPD MEA (100 V/cm) and the HS MEA respectively. The thickness of the CL for the EPD MEA was ~11.5 μm while the CL for the HS MEA was ~10 μm. The thicker CLs of the EPD GDE compared to the HS GDE was probably a result of the higher porosity as revealed by MIP analysis.
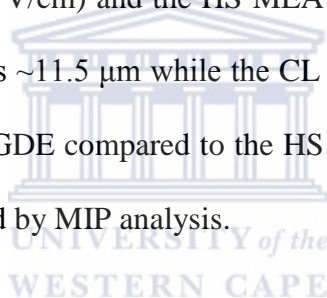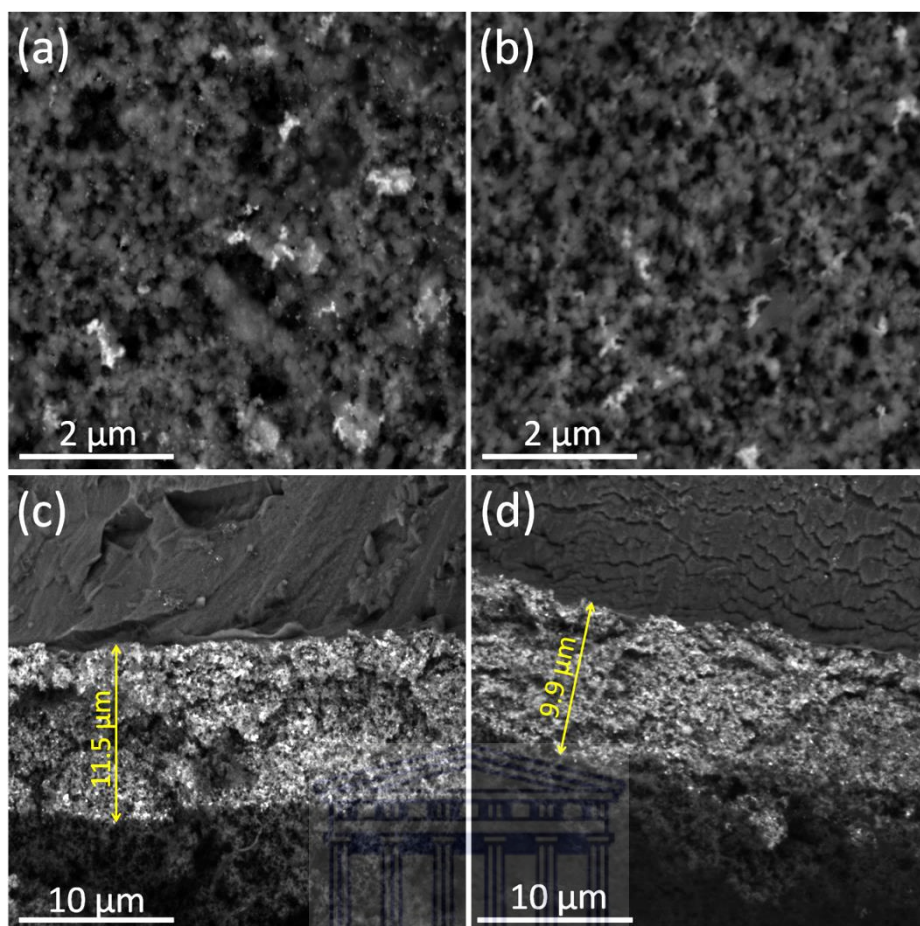
Fig. 4.7: Back scattered images of (a) EPD GDE (100 V/cm), (b) HS GDE, (c) EPD MEA 100 V/cm) cross section and (d) HS MEA cross section. All CLs contained 20 wt% Nafion® ionomer and 0.4 mg/cm² Pt loading.

Fig. 4.8 shows the MIP results obtained for EPD GDEs fabricated at various applied electric field strengths. The higher electric field strengths resulted in more porous electrodes especially in the macro pores region. The presence of macro pores could result in higher gas flow through the pores. Larger pore diameters results in higher fuel crossover from the anode to the cathode and lower the cell performance [151]. In electrodeposition, high voltages are known to cause a rupturing of the deposited film due to current breaking through the film leading to local generation of gas under the deposited film [152]. Rupturing can similarly occur in EPD and usually result in a thick and porous film. **Fig. 4.9** shows the MIP results of the EPD GDE (100 V/cm)

65

and the HS GDE. The figure shows a distinct difference between the EPD GDE and HS GDE. The HS GDE shows no pore diameters > 100 μm while the EPD GDE shows pore diameters up to ~1,000 μm. The larger pore diameters present in the EPD GDE was probably a result of the cracked morphology as revealed by HR-SEM analysis. The EPD GDE also showed more prominent peaks in the micro pore region compared to the HS GDE. This indicates the presence of a larger number of smaller pores for the EPD GDE compared to the HS GDE. Smaller pore diameters are beneficial for MEA performance. The EPD GDE had a total pore area of 22.46 m^2/g and the HS GDE had a total pore area of 13.43 m^2/g as calculated by the MIP analyser.
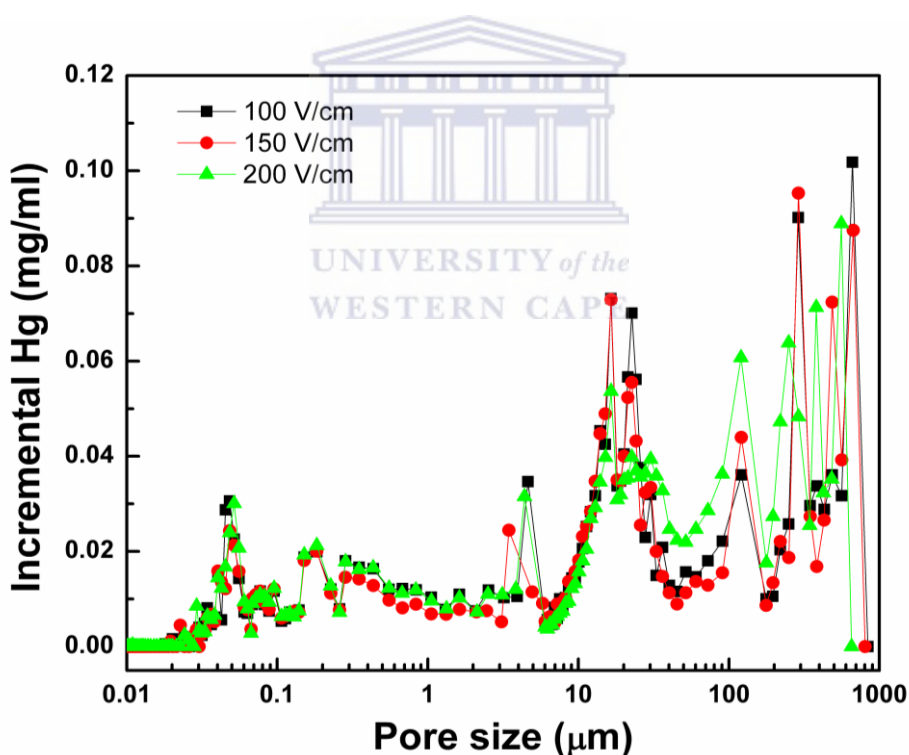
Fig. 4.8: MIP analysis of the EPD GDEs fabricated at various applied electric field strengths. All CLs contained 20 wt% Nafion® ionomer and 0.4 mg/cm^2 Pt loading.
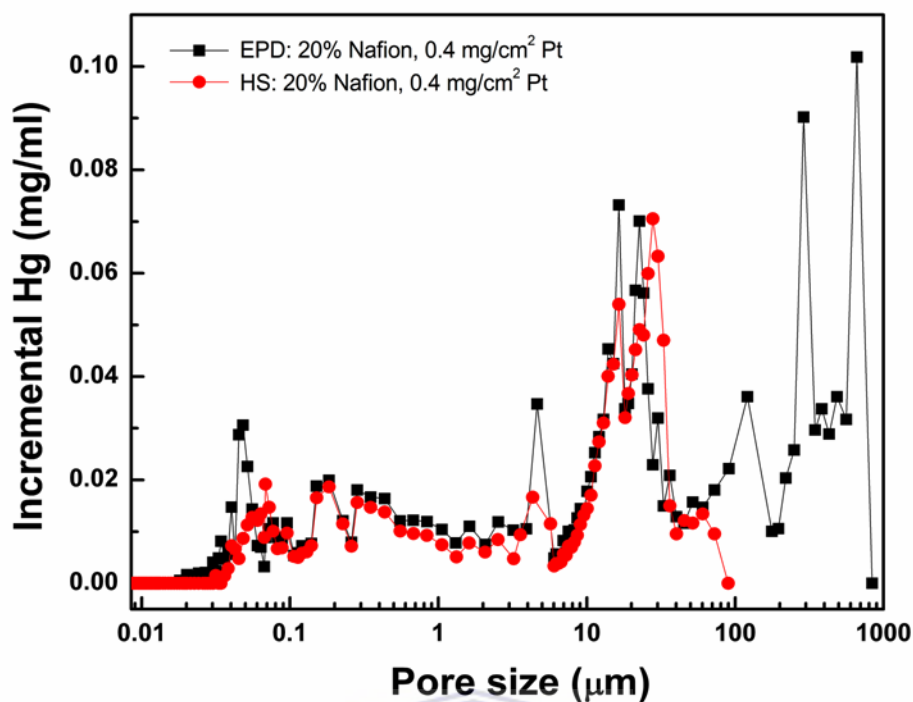
Fig. 4.9: MIP analysis of the EPD GDE (100 V/cm) and HS GDE. All CLs contained 20 wt% Nafion® ionomer and 0.4 mg/cm² Pt loading.

4.2.3 Electrochemical characterisation of MEAs

The Nafion® ionomer plays an important role in TPB formation and maintaining the structure of the CL therefore it is important to determine the optimum amount of Nafion® ionomer to be incorporated into the CL structure. **Fig. 4.10** shows the polarisation and power density curves of EPD MEAs with various Nafion® ionomer contents in the CLs. The Nafion® ionomer content was varied simultaneously on both anode and cathode from 10 to 30 wt% with respect to the Pt/C content. The Pt loading was 0.4 mg/cm² for both anode and cathode GDEs. The air flow rate was 1 slpm and the H_2 flow rate was 0.5 slpm.
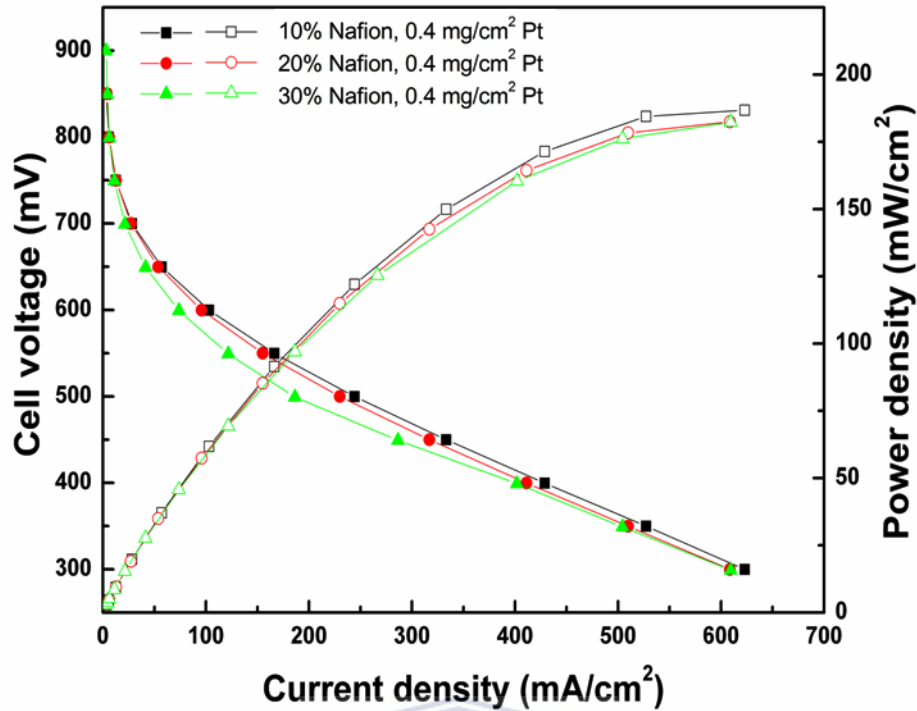
Figure 4.10: Polarisation and power density curves of the EPD MEAs (100 V/cm). CLs contained various Nafion® ionomer (10 to 30 wt%) contents and 0.4 mg/cm^2 Pt loading. Operating temperature was 160°C. Air flow rate was 1 slpm and H_2 flow rate was 0.5 slpm.

The MEA with 10 wt% Nafion® ionomer in the CLs showed comparable performance to the MEA with 20 wt% Nafion® ionomer in the CL during the polarisation measurements. A slight decrease in MEA performance was observed as the Nafion® ionomer content was increased to 30 wt%. The Nafion® ionomer is not a suitable ionomer/binder material for HT-PEMFCs as it needs to be kept hydrated for optimum proton conduction. Although 10 wt% Nafion® ionomer content showed slightly higher MEA performance, it showed the lowest stability during the activation period. Therefore 20 wt% Nafion® ionomer content was selected for all further studies. The optimum Nafion® ionomer content can be affected by both the *Pt* loading as well as the method of CL formation. Louh *et al.* [31] observed optimum performance at 40 wt% Nafion® ionomer content for a 0.16 mg/cm^2 *Pt* loading *via*

the EPD method while Huang *et al.* [153] observed the best MEA performance at 33 wt% Nafion® ionomer content for a 0.3 mg/cm^2 *Pt* loading *via* an ultrasonic spray method, both for LT-PEMFCs.

Fig. 4.11 shows the polarisation and power density curves of EPD MEAs with 20 wt% Nafion® ionomer and CLs deposited at various applied electric field strengths. The Pt loading was 0.4 mg/cm^2 for both anode and cathode GDEs. The air flow rate was 1 slpm and the H_2 flow rate was 0.5 slpm.
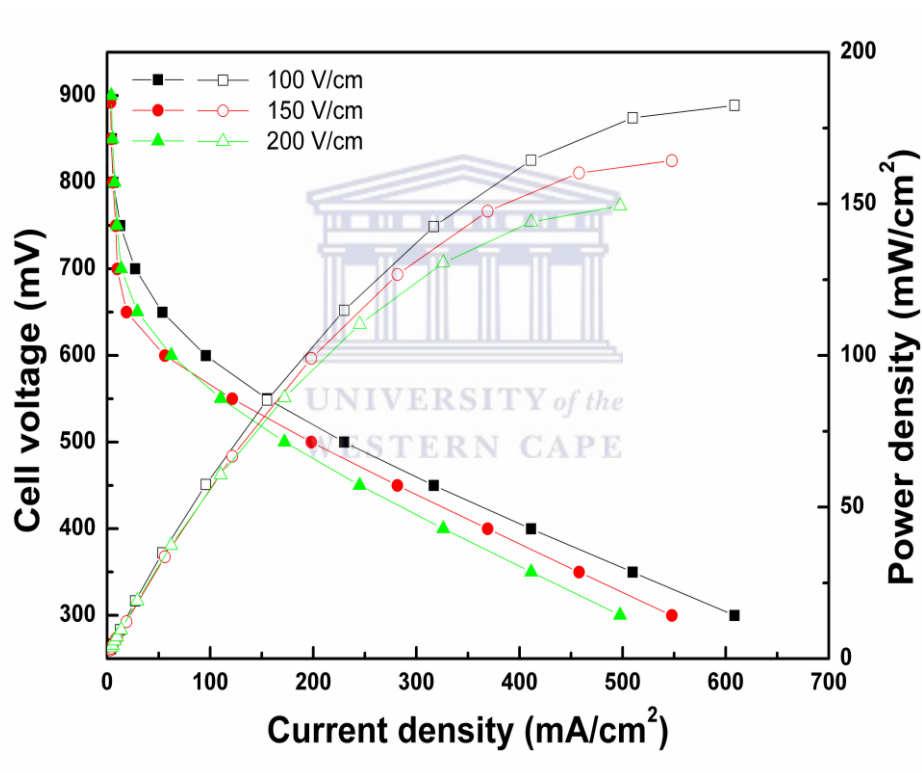
Fig. 4.11: Polarisation and power density curves of the EPD MEAs with GDEs fabricated at various applied electric field strengths. All CLs contained 20 wt% Nafion® ionomer and 0.4 mg/cm^2 Pt loading. Operating temperature was 160°C. Air flow rate was 1 slpm and H_2 flow rate was 0.5 slpm.

The result indicated that the lower applied electric field strength (i.e. 100 V/cm) yielded a higher MEA performance. Basu *et al.* [122] observed that higher quality deposits were obtained at moderate applied electric field strengths (i.e. 25 to 100

V/cm) whereas the deposit quality deteriorates at higher applied electric field strengths (> 100 V/cm). The applied electric field strength will however depend on the dielectric constant of the dispersant. Particle deposition at the electrode is a kinetic phenomenon therefore the particle accumulation rate affects the particle packing behaviour in the deposit. Higher applied electric field strengths are also known to cause more turbulent particle movement that leads to uneven deposited layers. Since the EPD process is selective towards smaller particles it may be possible that at higher applied electric field strengths, larger particles are also deposited due to the stronger driving force. HR-SEM images showed greater roughness and wider cracks for the GDEs fabricated at higher applied electric field strengths. Based on the polarisation results, the morphology of GDEs obtained at 100 V/cm were more favourable for the formation of TPBs required for high MEA performance.
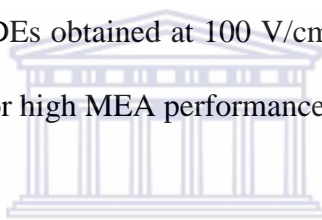
Fig. 4.12 shows the polarisation and power density curves of the EPD MEA (100 V/cm) and HS MEA. For peak power, the EPD MEA exhibited up to 73% higher power compared to the HS MEA. The significant difference in MEA performance was due to the significant difference in GDE morphology. HR-SEM analysis revealed that the EPD GDEs possessed a significant amount of cracks which where beneficial for MEA performance. Back scattered images also showed better dispersion of the *Pt* particles in the CLs of the EPD GDEs compared to the HS GDEs. This suggested an improvement in TPB formation for the EPD MEA compared to the HS MEA. MIP analyses confirmed that the EPD GDEs possessed larger pore diameters as well as a greater abundance of micro pores, allowing easier access for gaseous reactants to the catalyst sites.
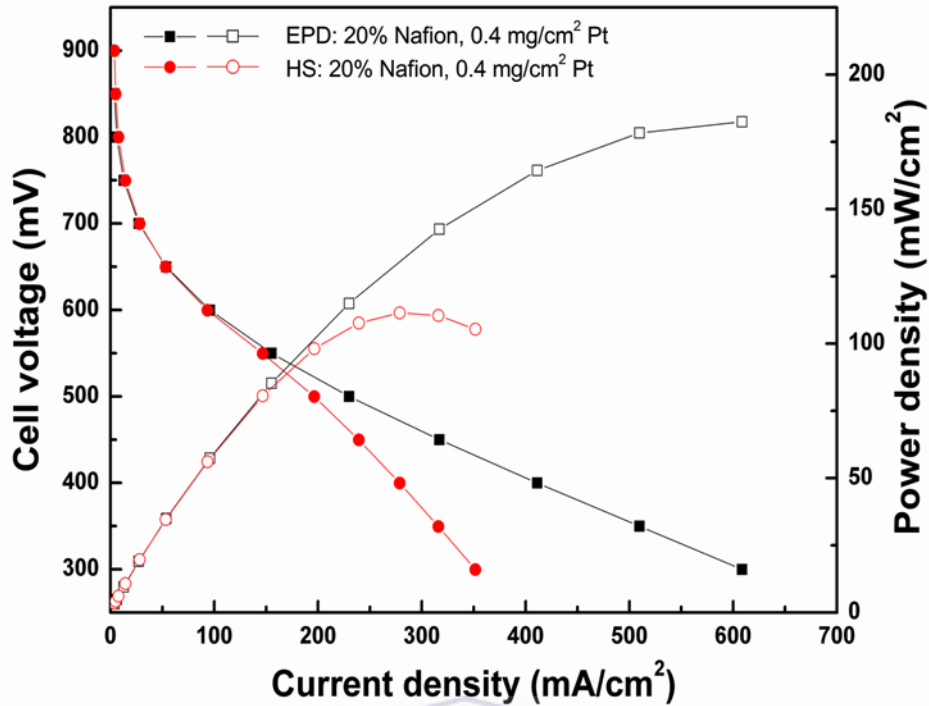
Fig. 4.12: Polarisation and power density curves of the EPD MEA (100 V/cm) and HS MEA. All CLs contained 20 wt% Nafion® ionomer and 0.4 mg/cm^{-2} Pt loading. Operating temperature was 160°C. Air flow rate was 1 slpm and H_2 flow rate was 0.5 slpm.

Fig. 4.13 shows the EIS spectra of the EPD MEA (100 V/cm) and HS MEA under 300 mA/cm^2 current loads. The left intercept of the impedance arc is due to the high frequency response and represents the total ohmic resistance of the cell. The total ohmic resistance is due to cell components such as the membrane, CL, GDL (inc. MPL) and bipolar plates [154]. The EPD MEA and HS MEA exhibited comparable behaviour in the high frequency range which implied that the ohmic resistances of the two MEAs were comparable. The charge transfer resistance, represented by the diameter of the arc, is the resistance dominated by the ORR. The charge transfer resistance was much lower for the EPD MEA compared to the HS MEA and resulted in a significantly higher MEA performance. The lower charge transfer resistance

71

indicated that the EPD method was more suitable to fabricate GDEs for HT-PEMFCs compared to the HS method.
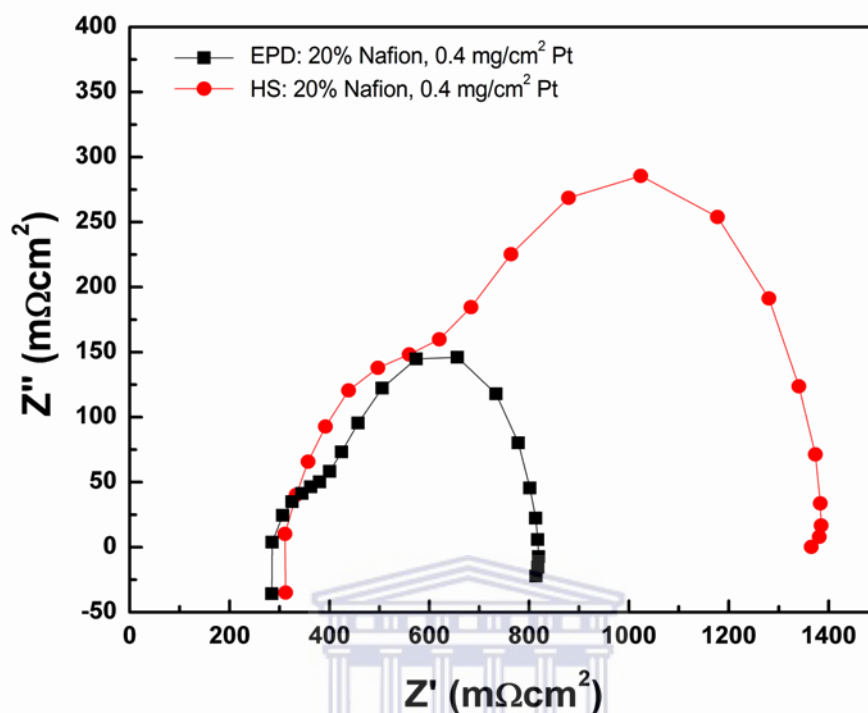
Fig. 4.13: EIS analysis of the EPD MEA (100 V/cm) and HS MEA under 300 mA/cm^2 load. All CLs contained 20 wt% Nafion® ionomer and 0.4 mg/cm^2 Pt loading. Operating temperature was 160°C. Air flow rate was 1 slpm and H_2 flow rate was 0.5 slpm.

Fig. 4.14 shows the *IR* free polarisation curves of the EPD MEA (100 V/cm) and HS MEA. Internal resistances were corrected based on the high frequency resistance of the *AC* impedance. Under low current load, the EPD MEA and HS MEA displayed similar performances which implied that the activities of the catalysts were similar due to the use of the same catalyst material for both MEAs. Under higher current load, a significant difference in MEA performance was observed. Under higher current load, a higher relative mass transport resistance was observed for the HS MEA. The EPD GDEs had a larger total pore area compared to the HS GDEs,

72

allowing easier access for gaseous reactants to the catalyst sites; therefore a better performance was expected for the EPD MEA, especially under higher current load.
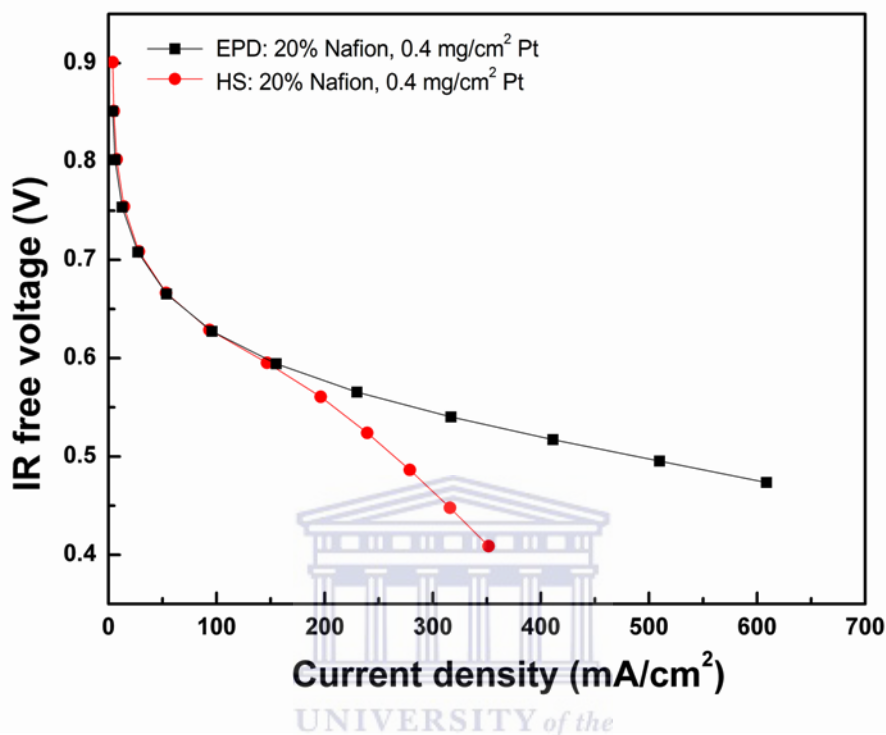
Fig. 4.14: *IR* **free polarisation curves of the EPD MEA (100 V/cm) and HS MEA. All CLs contained 20 wt% Nafion® ionomer and 0.4 mg/cm^2 Pt loading. Operating temperature was 160°C. Air flow rate was 1 slpm and H_2 flow rate was 0.5 slpm.**

4.3 Conclusions

The EPD method was adapted to fabricate GDEs/MEAs with Nafion® ionomer in the CLs. Catalyst suspensions were studied and optimum *Pt/C*-Nafion® suspensions to fabricate the GDEs *via* EPD were obtained when the pH was adjusted between 8 and 10. These suspensions yielded good stability and sufficient conductivity to form CLs on top of the GDLs. Higher applied electric field strengths (> 100 V/cm) negatively affected MEA performance while increasing the Nafion® ionomer content (up to 30 wt %) only slightly affected MEA performance. Single cell tests showed that MEAs

73

fabricated by the EPD method performed better than the HS MEAs due to a lower charge transfer resistance at high current densities. This study showed that the EPD method was more suitable than the traditional hand spray method to fabricate GDEs for HT-PEMFCs even though the highest performance observed, was only ~180 mW/cm^2. The reason for the low MEA performances was because the Nafion® ionomer was not the best suited ionomer/binder for high temperature MEAs. The Nafion® ionomer formed stable catalyst suspensions that readily deposited onto the GDLs with good reproducibility. Therefore these GDEs would be more suitable for MEAs in LT-PEMFCs.

UNIVERSITY *of the*
WESTERN CAPE

Chapter 5: EPD of Pt/C-PTFE nano-particles for the fabrication of GDEs/MEAs

5.1 Introduction

Polytetrafluoroethylene (PTFE) is hydrophobic in nature and is commonly incorporated in the MPL of LT-PEMFC electrodes to maintain the integrity of carbon particles and to improve water management [155]. PTFE forms porous catalyst structures [156] and allows both reactant gases and liquid acid (such as the phosphoric acid (PA) present in the membrane) to access the active catalyst sites [24, 156]. The presence of PA in the CLs is important as PA is needed to conduct protons from the active *Pt* sites of the anode through the ABPBI membrane to the active *Pt* sites of the cathode. PTFE facilitates the formation of the TPBs which consists of the proton conducting electrolyte, electron conducting catalyst and reactant gases [24]. For these reasons PTFE are also incorporated into CLs for HT-PEMFC electrodes [59, 66].
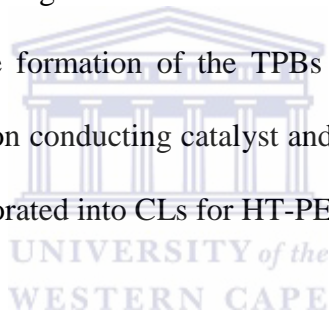
The stability of the *Pt/C*-PTFE catalyst particles in IPA was studied and optimum catalyst suspensions were used to fabricate the GDEs/MEAs. Physical characterisations of the GDEs/MEAs included HR-SEM and MIP analyses while electrochemical characterisations included polarisation measurements, EIS and CV analyses. An ultrasonic spray method was demonstrated by refs [94, 153] and proved to be very useful for the fabrication of GDEs with ultra-low *Pt* loadings for MEAs in LT-PEMFCs. Thus MEAs fabricated *via* the ultrasonic spray method were used as a comparison to the EPD MEAs. The influence of the Nafion® ionomer and PTFE in the CLs of EPD MEAs were compared based on MEAs performance.

5.2 Results and Discussion

5.2.1 Catalyst suspension characterisation

To prepare suspensions suitable for EPD the following four conditions should be met: (i) the particles in solution need to be charged otherwise the particles will not migrate with the externally applied electric field, (ii) the particles should be well dispersed and stable over the EPD duration to form homogeneous deposits, (iii) ions other than the charged particles should be kept to a minimum as these lower the transport number of the particles. Compression of the electrical double layer (EDL) occurs at high ionic concentrations which reduces the stability of the suspension and (iv) the particles should strongly adhere to the substrate. Adhesion may be improved by the addition of polymer binders.
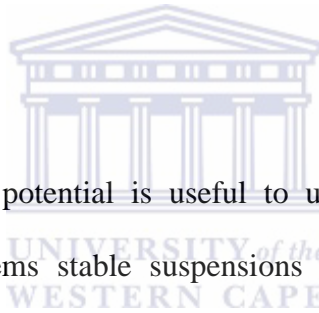
Measuring the particle zeta potential is useful to understand the stability of the suspensions. For some systems stable suspensions with high zeta potentials are obtained by simply dispersing the particles in the solution. In general, particles can be positively or negative charged by adding the appropriate amount of acid, base or polyelectrolytes to the suspension. Particle surfaces modified by polyelectrolytes have charges corresponding to the functional groups (e.g. carboxylic acid groups or amino groups). The addition of excess acid or base can be disadvantageous as the un-adsorbed ions compress the EDLs and affect the suspension stability. Free ions become the majority of the charge carriers during EPD and the transport number of the charged particles drops which affects the deposition rate of the particles resulting in thin deposited layers [112]. For the case of Carbon Nanotubes (CNT), it was observed that the addition of charger salts (such as *NaCl*) can increase the suspension

stability by associating a charge with the CNT surface in the solution and improve the adhesion and deposition of the CNTs to the target substrate [157].

Figs. 5.1 and **5.2** show the zeta potentials (ζ_{exp}) and sizes of the *Pt/C* particles mixed with various PTFE contents in IPA solutions with various *NaCl* concentrations respectively. **Fig. 5.1** shows that the catalyst particles were negatively charged in all suspensions and would therefore deposit onto the positively charged electrode. When no *NaCl* was added to the suspensions, the catalyst particles showed the highest zeta potentials ranging between -44 and -52 mV and particle sizes ranging between ~248 and 263 nm. These suspensions were stable since no significant change in particle size was observed which was indicative of very slow particle coagulation. This type of suspensions is commonly prepared for spraying methods where the conductivity of the suspension is not crucial. For suspensions containing no *NaCl*, the highest zeta potential (i.e. -52 mV) and smallest particle size (i.e. 248 nm) were observed when 20 wt% PTFE was added while the lowest zeta potential (i.e. -44 mV) and largest particle size (i.e. 263 nm) were observed when no PTFE was added. This suggested that the PTFE had some stabilising effect on the *Pt/C* particles in suspension however the mechanism is not clear however it may be predominantly hydrophobic and steric in nature. These suspensions are not suitable for EPD since there is insufficient conductivity due to the low dielectric constant ($\varepsilon \approx 18.23$) of IPA and the particles would not deposit under the force of the externally applied electric field. For suspensions containing 0.1mM *NaCl*, zeta potentials ranged between -33 and -35mV. The zeta potentials were noticeably smaller in magnitude however the particle sizes were unaffected. Particle sizes ranged between 246 and 255 nm. For suspensions containing 0.2 mM *NaCl*, zeta potentials ranged between -30 and -34 mV. The

average particle sizes were clearly affected as the PTFE content was increased ranging from 265 nm for 0 wt% PTFE to 366 nm for 50 wt% PTFE. For suspensions containing 0.5 mM *NaCl*, zeta potentials decreased to less than -30 mV and the particle sizes were significantly affected. The zeta potentials decreased from -25 mV for 0 wt% PTFE to -17 mV for 50 wt% PTFE. Particles sizes ranged from 472 nm for 0 wt% PTFE to 1600 nm for 50 wt% PTFE. The rapid coagulation could be the result of the compression of the EDLs due to the high ionic concentration. At high ionic concentrations, the PTFE content had a significant influence on the stability of the suspension. From **Figs 5.1** and **5.2** it was clear that to obtain stable catalyst suspensions for EPD, the *NaCl* concentration should be < 0.1 mM.
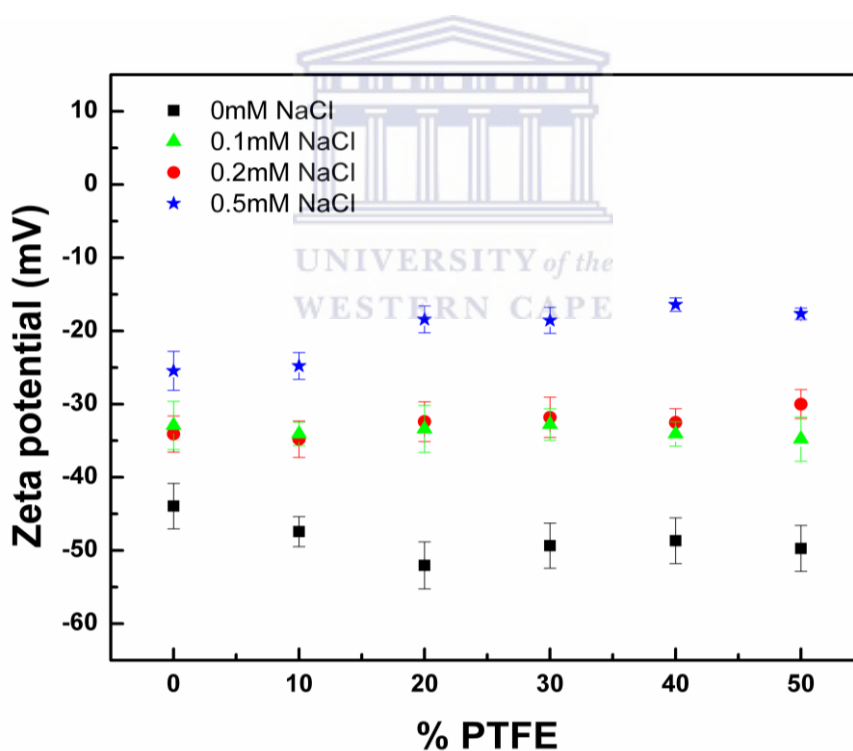
Fig. 5.1: Zeta potential of *Pt/C* particles with various PTFE compositions in IPA with various *NaCl* concentrations.
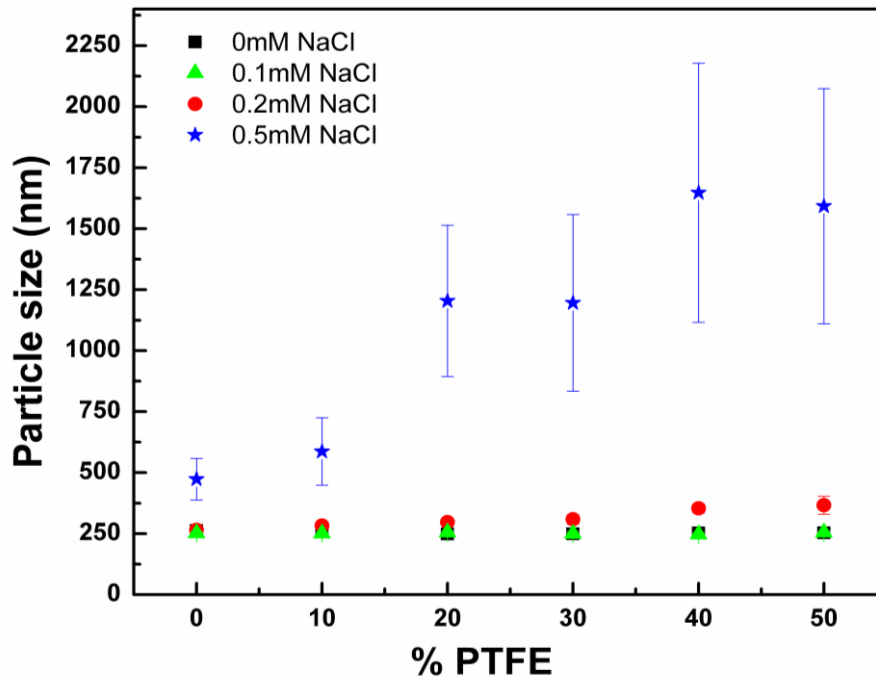
Fig. 5.2: Size of *Pt/C* particles with various PTFE compositions in IPA with various *NaCl* concentrations.

Figs. 5.3 and **5.4** show the zeta potentials and sizes of the *Pt/C*-PTFE and *Pt/C*-Nafion® particles at various pH values respectively. The *Pt/*C-PTFE suspension was only stable between pH 3 to 9 as was deduced from the particle sizes which ranged between 285 to 300 nm. At pH 2, the *Pt/*C-PTFE particle size increased to 920 nm while at pH 10 to 12 the particles coagulated to form particles with sizes ranging between 740 to 1300 nm. The *Pt/*C-Nafion® suspensions were stable over the whole pH range due to the steric stabilisation effect of the sulphonic acid side chains. No or very little steric stabilisation was expected from the PTFE polymer as it contained no charged side chains. A suitable suspension pH is necessary for successful EPD therefore pH 7 to 8 would be most suitable as it would yield sufficient conductivity.
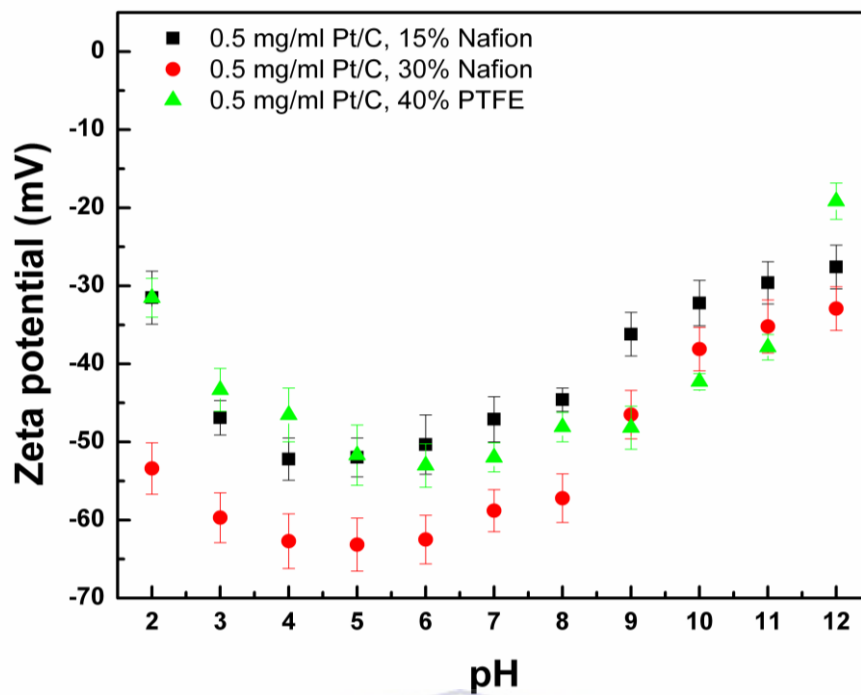
Fig. 5.3: Zeta potential of *Pt/C*-PTFE and *Pt/C*-Nafion® particles vs. suspension pH.
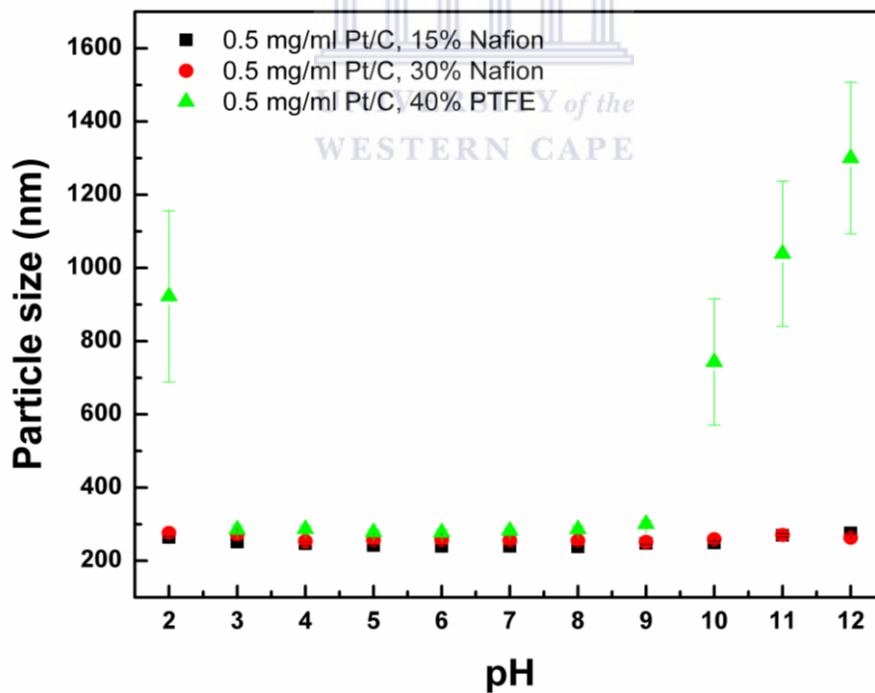
Fig. 5.4: Size of *Pt/C*-PTFE and *Pt/C*-Nafion® particles vs. suspension pH.

5.2.2 GDE/MEA fabrication and physical characterisation

For the fabrication of EPD GDEs with PTFE in the CLs, the *NaCl* concentration was kept at 0.01 mM for all catalyst suspensions to minimize the *NaCl* concentration deposited into the CLs and to avoid the formation of unstable suspensions. Syed *et al.* [158] observed that the chloride impurity can drastically decrease the performance and durability of the PBI based MEAs. It was proposed that *Pt* chloro-complexes such as hexachloroplatinate ($PtCl_6^{2-}$) or terachloroplatinate ($PtCl_4^{2-}$) were formed in the presence of chloride impurities. The *Pt/C*-PTFE suspension where the pH was adjusted was not used for the fabrication of EPD GDEs in this study. For the fabrication of EPD GDEs with the Nafion® ionomer in the CL, the catalyst suspension was adjusted to pH 9. Lower zeta potentials were observed for the *Pt/C*-PTFE suspensions compared to the *Pt/C*-Nafion® suspensions; therefore higher applied electric field strength (i.e. 200 V/cm) was required to obtain sufficiently high *Pt* loadings for the GDEs. GDEs that received heat treatment are referred to as 340°C HT while GDEs that received no heat treatment are referred to as no HT. Heat treatment of GDEs were carried out at 340°C under Ar atmosphere to remove the surfactant from the PTFE binder and to increase the porosity of the GDE.

Fig. 5.5 shows the HR-SEM images of the EPD and Sonotek GDEs. The EPD GDEs had 0.48 mg/cm^2 *Pt* loadings while the Sonotek GDEs had 0.5 mg/cm^2 *Pt* loadings and both GDE types had 40 wt% PTFE contents. **Figs 5.5 a** and **b** show the HR-SEM images of the EPD GDE (no HT) and the Sonotek GDE (no HT) at 1, 000 x magnification respectively. The EPD GDE morphology was dominated by cracks which was the result of drying of the relatively thick (~25 μm) CL in a single step. The Sonotek GDE appeared relatively smooth and uniform. The Sonotek automated

sprayer is capable of spraying a very fine mist of the catalyst particles which is continuously dried *via* a hot plate (heated to 80°C) during the spraying process. **Figs. 5.5 c** and **d** show the HR-SEM images of the EPD GDE (no HT) and the Sonotek GDE (no HT) at 50, 000 x magnification respectively. The EPD GDE exhibited uniform porous morphology while the morphology of the Sonotek GDE was notably different. The Sonotek GDE exhibited catalyst particles that were smaller compared to the EPD GDE however it also contained larger particles (i.e. > 300 nm). Energy dispersive X-ray (EDX) analysis showed that these larger particles had higher (~60 %) PTFE contents compared to the smaller catalyst particles. PTFE resulted in the agglomeration of the catalyst particles in the CL of the Sonotek GDE. **Figs. 5.5 e** and **f** show the HR-SEM images of the EPD GDE (340°C HT) and the Sonotek GDE (340°C HT) at 50, 000 x magnification respectively. The EPD GDE (340°C HT) showed no notable change in morphology after the heat treatment process. The Sonotek GDE (340°C HT) showed agglomeration of the catalyst particles due to the melting of PTFE. No agglomeration of the catalyst particles were observed for the EPD GDE (340°C HT). This suggested that during EPD the *Pt/C* particles were uniformly coated with PTFE due to the formation of stable catalyst suspensions. It also suggested that only fine catalyst particles deposited during the EPD process which was consistent to that reported in the literature [30, 32].
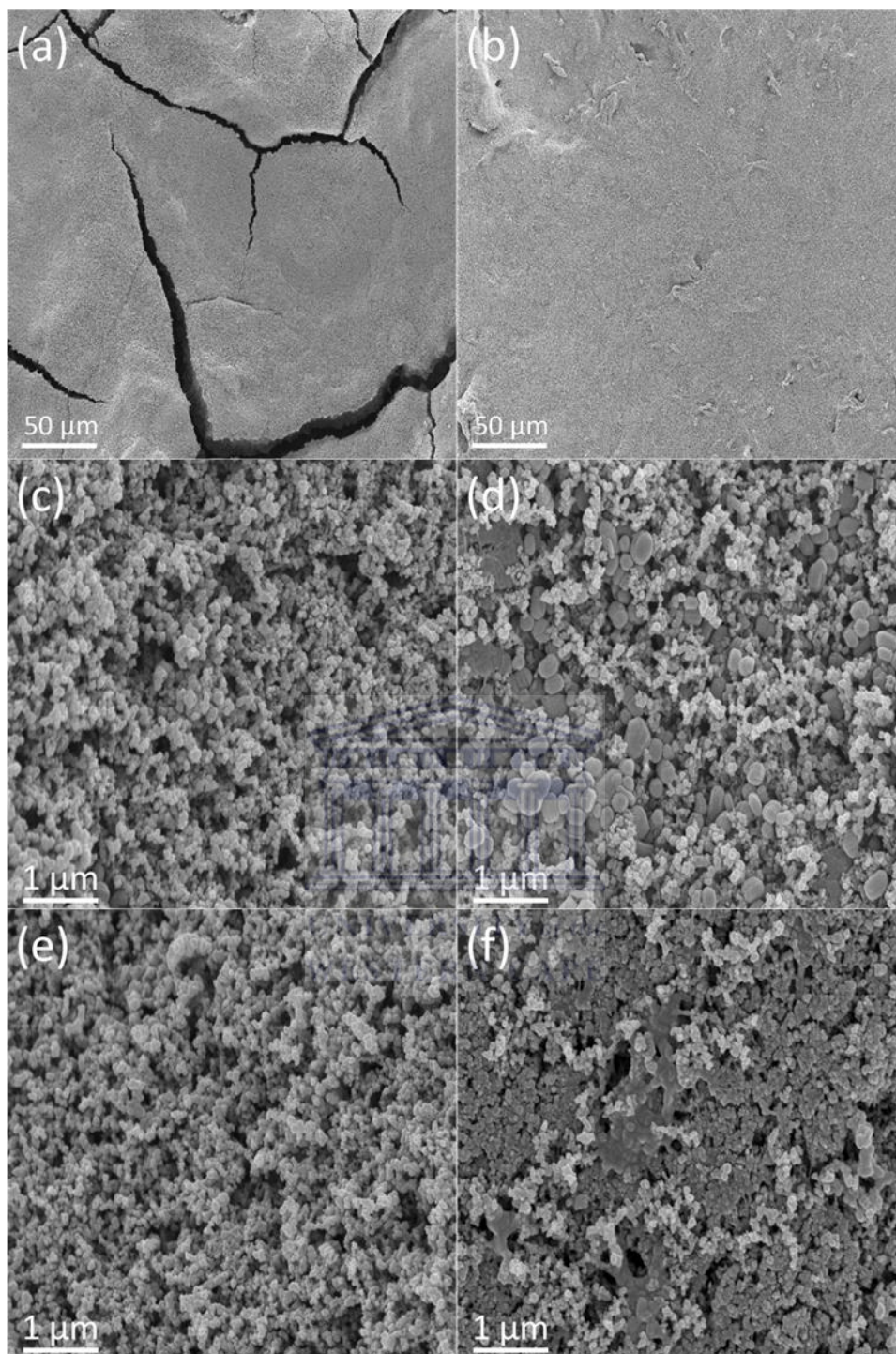
Fig. 5.5: HR-SEM images of **(a)** EPD GDE (no HT) at 1, 000 x magnification **(b)** Sonotek GDE (no HT) at 1, 000 x magnification **(c)** EPD GDE (no HT) at 50, 000 x magnification **(d)** Sonotek GDE (no HT) at 50, 000 x magnification **(e)** EPD GDE (340°C HT) at 50, 000 x magnification and **(f)** Sonotek GDE (340°C HT) at 50, 000 x magnification. EPD CLs contained 40 wt% PTFE and 0.48 mg/cm^2 Pt loading. Sonotek CLs contained 40 wt% PTFE and 0.5 mg/cm^2 Pt loading.

Fig. 5.6 a and **b** show the HR-SEM images of the cross sectional views of the EPD MEA (no HT) and Sonotek MEA (no HT) respectively. The thickness of the CLs for the EPD MEA (no HT) was ~25 μm and the thickness of the CLs for the Sonotek MEA (no HT) was between ~22 to 25 μm.
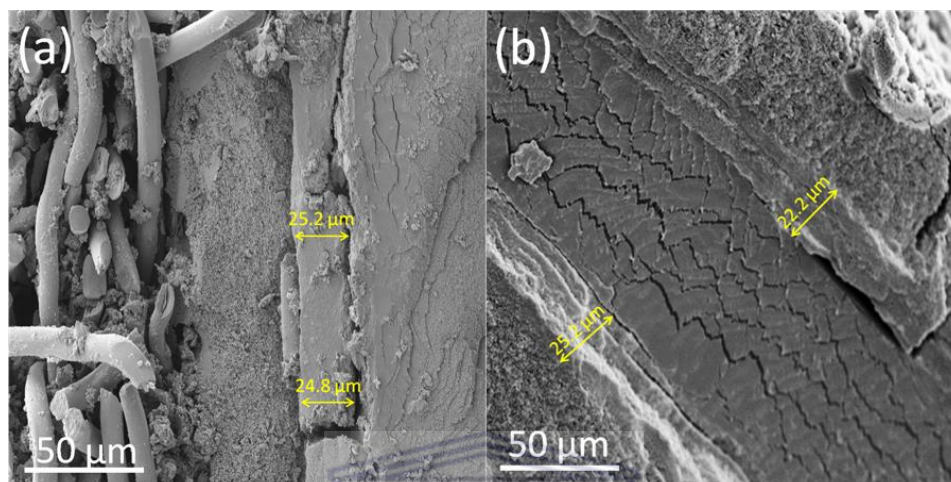
Fig. 5.6: HR-SEM images of the cross sections of (a) EPD MEA (no HT) and (b) Sonotek MEA (no HT). EPD CLs contained 40 wt% PTFE and 0.48 mg/cm^2 Pt loading. Sonotek CLs contained 40 wt% PTFE and 0.5 mg/cm^2 Pt loading.

Figs 5.7 a and **b** show the HR-SEM images of the EPD GDE (no HT) with PTFE in the CL and the EPD GDE (no HT) with Nafion® ionomer in the CL at 50, 000 x magnification respectively. Both GDE types showed uniform and porous morphology however the EPD GDE (no HT) containing the Nafion® ionomer in the CL showed slightly larger catalyst particles and larger pore sizes.
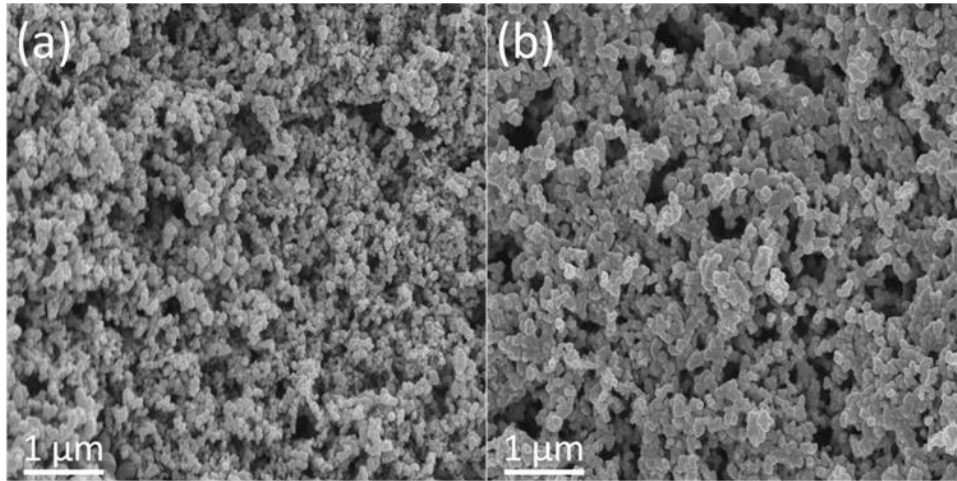
Fig 5.7: HR-SEM images of (a) EPD GDE (no HT) with CLs containing 40 wt% PTFE and 0.48 mg/cm^2 at 50, 000 x magnification and (b) EPD GDE (no HT) with CLs containing 20 wt% Nafion® ionomer and 0.5 mg/cm^2 at 50, 000 x magnification.

Fig. 5.8 shows the MIP analysis of the EPD and Sonotek GDEs. The EPD GDE (no HT) showed a higher total pore area (30.5 m^2/g) than the Sonotek GDE (no HT) which had a total pore area of 25.2 m^2/g. Heat treatment of the GDEs yielded an increase in porosity for both GDE types which was expected due to the presence of PTFE in the CLs [159]. The increase in porosity was mainly a result of a significant increase in macro pores. **Fig. 5.9** compares the MIP analysis of the EPD GDEs containing PTFE and Nafion® ionomer in the CLs. The EPD GDE with Nafion® ionomer in the CL had a slightly lower total pore area of 27.4 m^2/g. The results showed significantly more macro pores for the EPD GDE with Nafion® ionomer in the CL which was consistent to that observed from HR-SEM (**Fig. 5.6 b**).
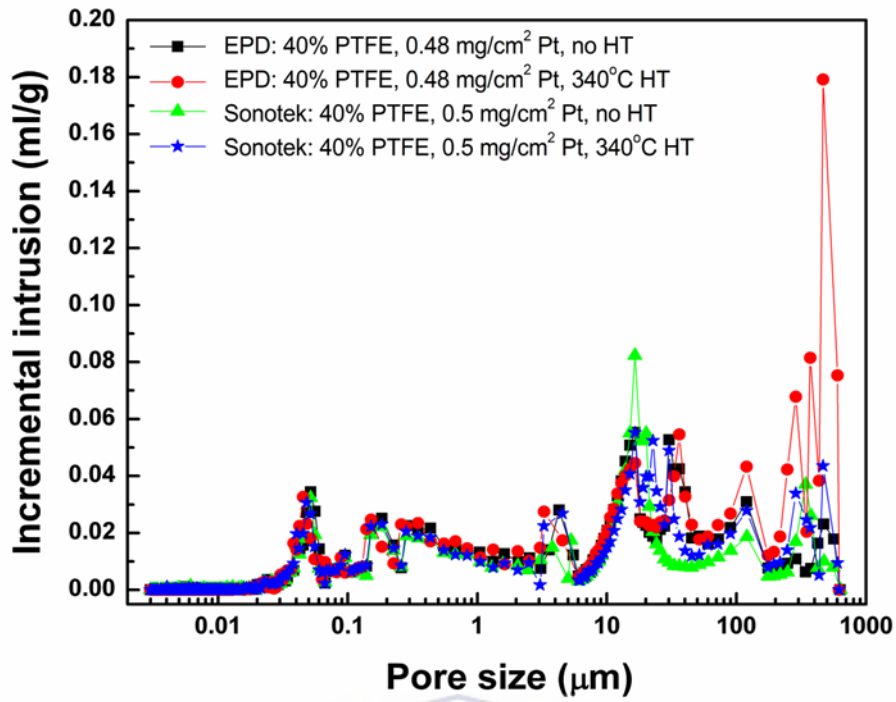
Fig. 5.8: MIP analysis of the EPD and Sonotek GDEs.
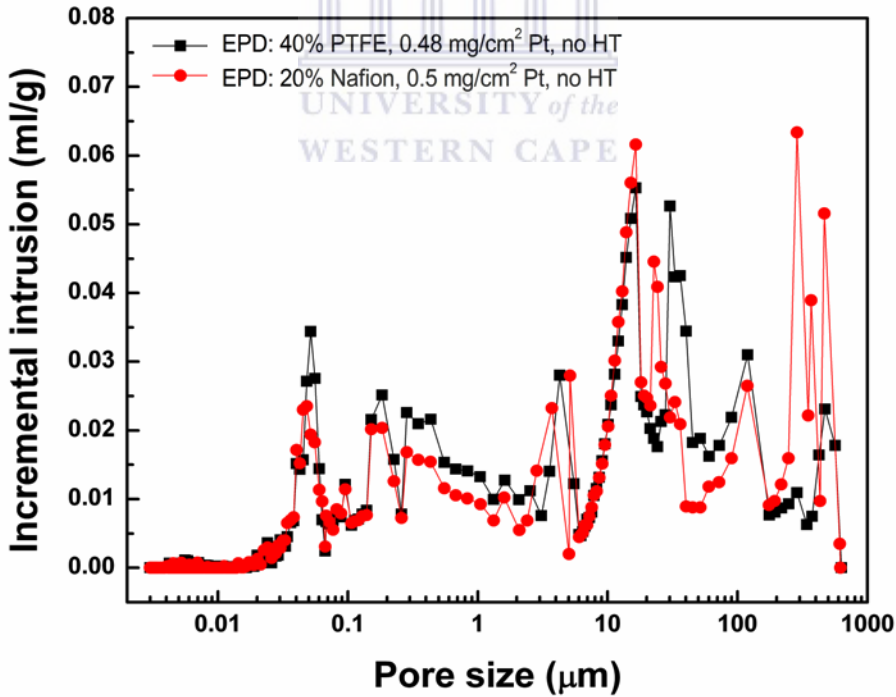
Fig. 5.9: MIP analysis of EPD GDEs (no HT).

5.2.3 Electrochemical characterisation of MEAs

All electrochemical analyses of the MEAs were carried out at 160°C. **Fig. 5.10** shows the polarisation and power density curves of the EPD MEAs where various PTFE contents in the CLs were studied. The *Pt* loading was 0.32 mg/cm^2 and the PTFE content was varied between 10 and 50 wt% with respect to the *Pt/C* content simultaneously for both the anode and cathode. Air flow rate was 1 slpm and the H_2 flow rate was 0.5 slpm. No noticeable change in MEA performance was observed as the PTFE content was increased. This suggested that the PTFE and *Pt/C* particles were well dispersed and were uniformly distributed in the CLs.
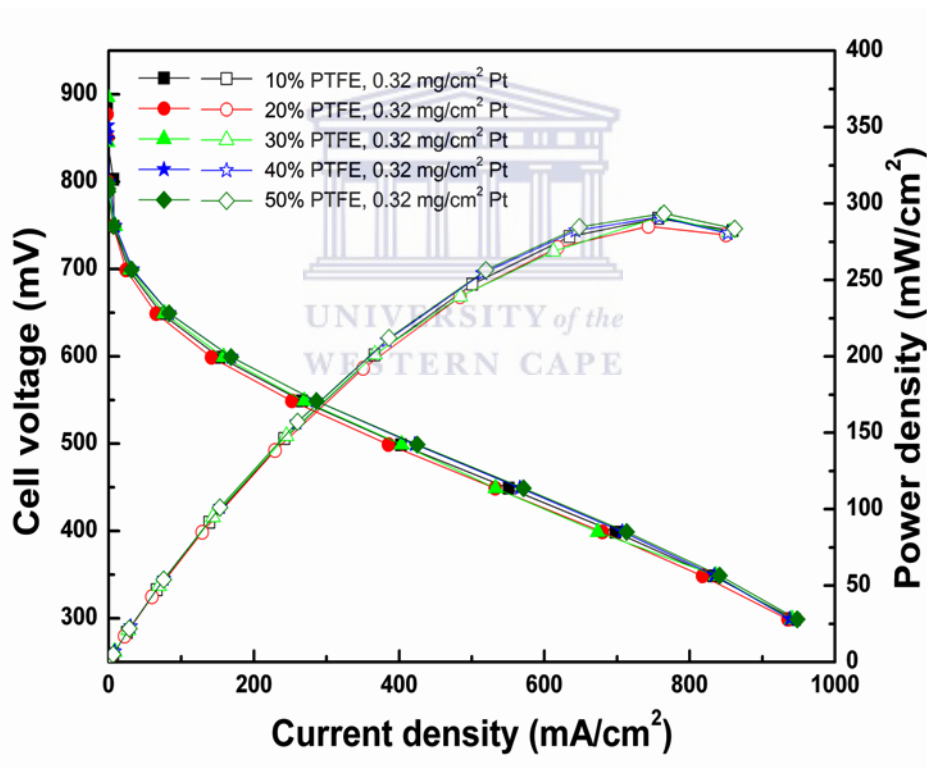
Fig. 5.10: Polarisation and power density curves of EPD MEAs with various PTFE (10 to 50 wt%) contents and 0.32 mg/cm^2 Pt loading. Operating temperature was 160°C. Air flow rate was 1 slpm and H_2 flow rate was 0.5 slpm.

The PTFE content with respect to the *Pt/*C particles was 40 wt% for all MEAs studied further in this chapter. The *Pt* loading for the EPD GDE with PTFE in the CLs was

0.48 mg/cm^2 (for both anode and cathode) while the *Pt* loading for the Sonotek GDE with PTFE and the EPD GDE with Nafion® ionomer was 0.5mg/cm^2 (for both anode and cathode). **Fig. 5.11** shows the polarisation and power density curves of the EPD and Sonotek MEAs. The EPD MEA (no HT) showed the highest MEA performance with ~12% increase in peak power compared to the Sonotek MEA (no HT). Heat treatment of the GDEs resulted in a slight lowering in the performance of the EPD MEA (340°C HT) while significantly lowering the performance of the Sonotek MEA (340°C HT). The increase in porosity of the GDEs usually result in improved MEA performance due to improved access for both the reactant gases and the liquid acid to the active catalyst sites [24, 156]. On the contrary, the increase in porosity may allow easier covering of the active *Pt* particles by PTFE and PA in the CL. The PO^{4-} in PA strongly adsorbs onto the *Pt* sites causing it to be inaccessible for electrochemical reactions. The significant lowering in the performance of the Sonotek MEA (340 °C HT) can be explained using the HR-SEM image in **Fig. 5.5 f** where the melting of PTFE clearly resulted in the agglomeration of the catalyst particles and covering of the active *Pt* sites.
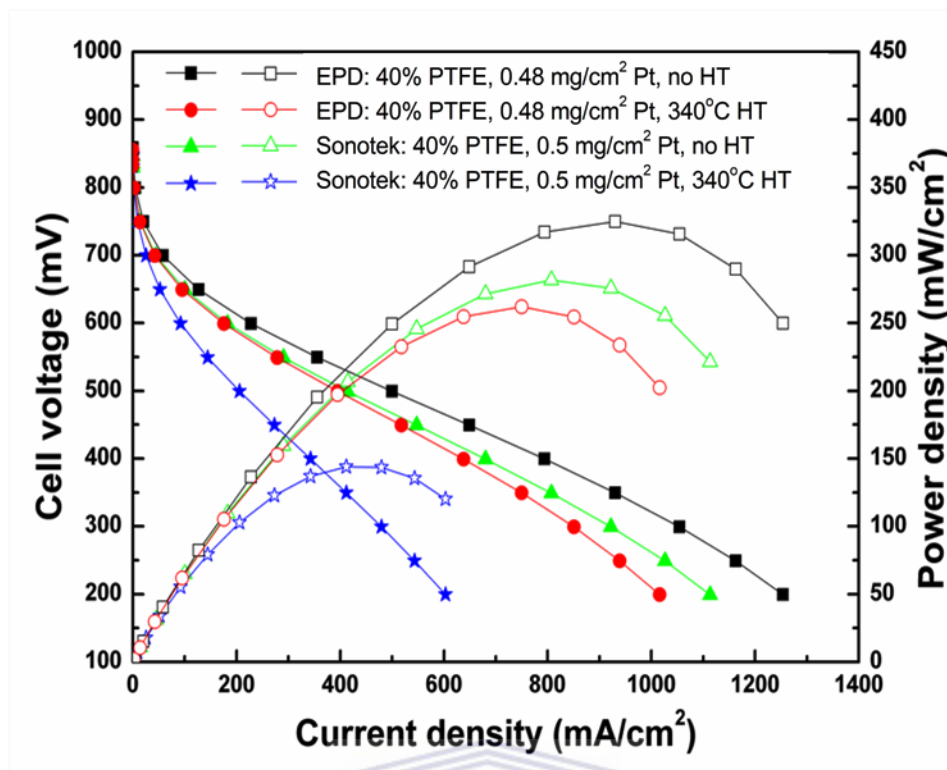
Fig. 5.11: Polarisation and power density curves of EPD and Sonotek MEAs. Operating temperature was 160°C. Air flow rate was 1 slpm and H_2 flow rate was 0.5 slpm.

Fig. 5.12 compares the polarisation and power density curves of the EPD MEAs (no HT), one containing 0.48 mg/cm^2 Pt and 40 wt% PTFE and the other containing 0.5 mg/cm^2 Pt and 20 wt% Nafion® ionomer in both anode and cathode CLs. The EPD MEA containing PTFE in the CLs exhibited better MEA performance. The tests were performed at 160°C which were above the glass transition temperature of the Nafion® ionomer. Above the glass transition temperature of the Nafion® ionomer, the polymer chain may rearrange which can lead to structural changes. The structural changes may have a negative effect on the stability and performance of the Nafion® ionomer [160].

89
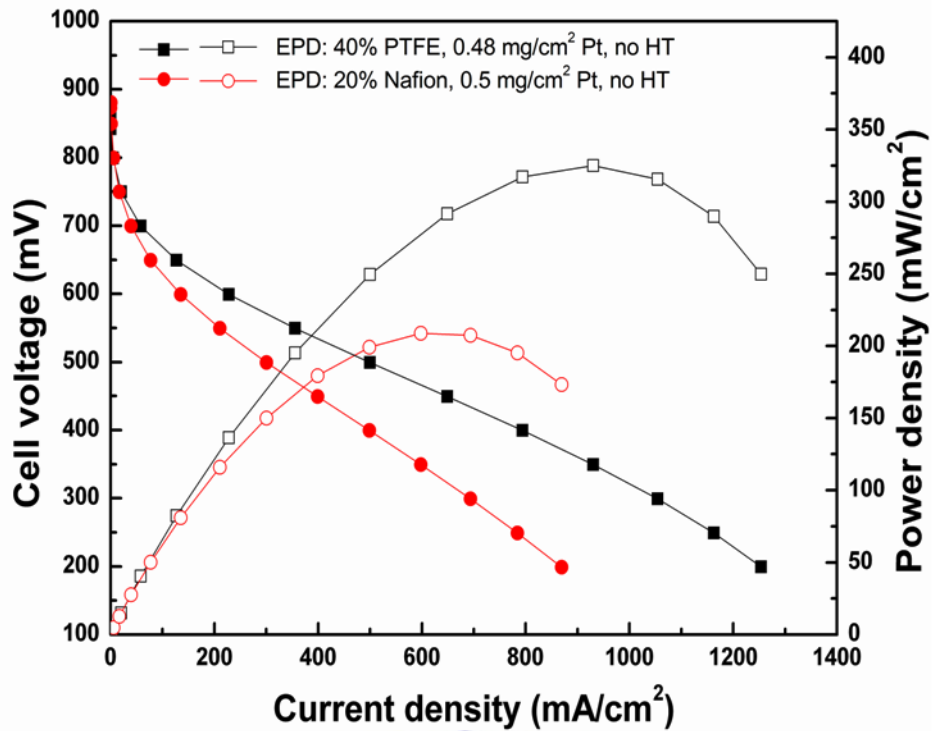
Fig. 5.12: Polarisation and power density curves of EPD MEAs (no HT). Operating temperature was 160°C. Air flow rate was 1 slpm and H_2 flow rate was 0.5 slpm.

CV analysis of the EPD and Sonotek MEAs is shown in **Fig. 5.13**. The Electrochemical Surface Area (ECSA) of each MEA was calculated using Eq. (5.1) [161].

$$ECSA = \frac{10^5 \times A_d}{C \times m \times v} \tag{5.1}$$

where A_d is the integral area of the hydrogen adsorption peak (AV), C is the coefficient of hydrogen adsorbed by *Pt* (0.21 mC/cm^2), m is the mass of *Pt* at the cathode (mg/cm^2) and v is the potential scan rate (mV/s).
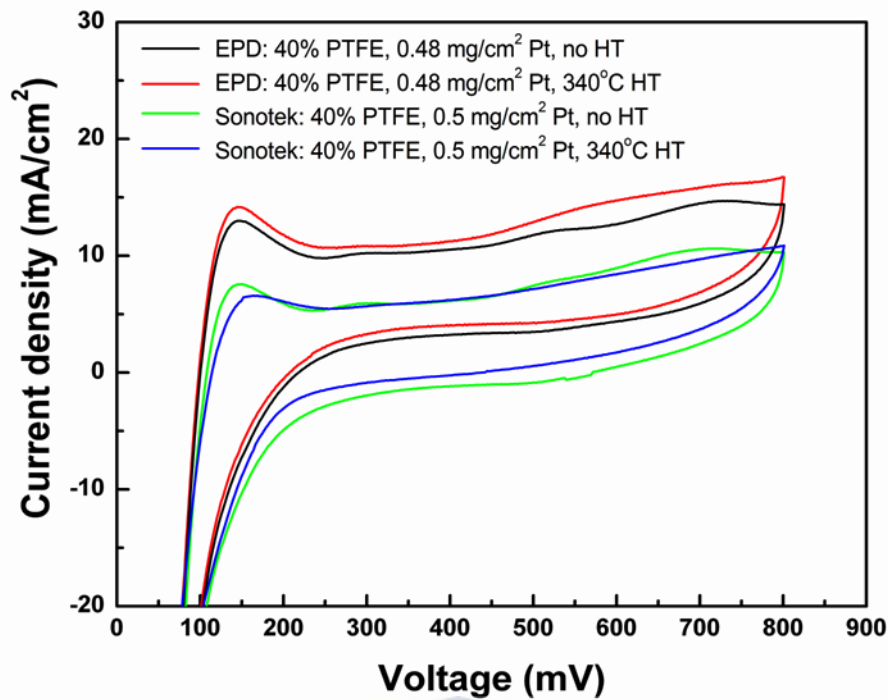
Fig. 5.13: CV analysis of EPD and Sonotek MEAs. Operating temperature was 160°C. Air flow rate was 1 slpm and H_2 flow rate was 0.5 slpm.

In **Fig. 5.13**, the hydrogen adsorption peak occurred between 110 and 230 mV for the MEAs studied. The ECSAs decreased by ~3 and ~51% after heat treatment of the EPD and Sonotek MEAs respectively. The reduction in the ECSA implied that the available surface *Pt* sites were reduced which affected MEA performance.

Fig. 5.14 shows the CV analysis of the EPD MEAs (no HT), one containing 0.48 mg/cm^2 Pt and 40 wt% PTFE and the other containing 0.5 mg/cm^2 Pt and 20 wt% Nafion® ionomer in both anode and cathode CLs. The hydrogen adsorption peak occurred between 110 and 230 mV for the MEAs studied. The EPD MEA (no HT) with PTFE in the CL showed ~53% larger ECSA compared to the EPD MEA (no HT) with the Nafion® ionomer in the CL.

91
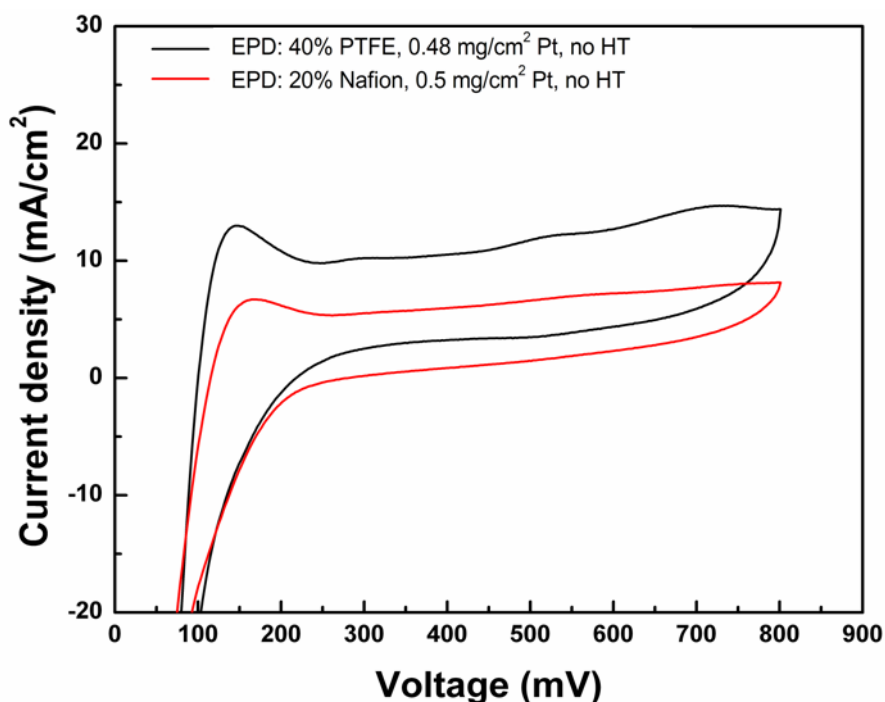
Fig. 5.14: CV analysis of EPD MEAs (no HT). Operating temperature was 160°C. Air flow rate was 1 slpm and *H₂* flow rate was 0.5 slpm.

Fig. 5.15 shows the EIS analysis of EPD and Sonotek MEAs and revealed highest charge transfer resistance (observed from the diameter of the arc) for the Sonotek MEA (340°C HT). This indicated that the Sonotek GDE (340°C HT) had less active *Pt* sites which was the result of being covered by PTFE and becoming inaccessible to the reactant gases for electrochemical reactions. The EPD MEA (no HT) showed the lowest charge transfer resistance which was indicative of better electrode kinetics, resulting in better MEA performance.
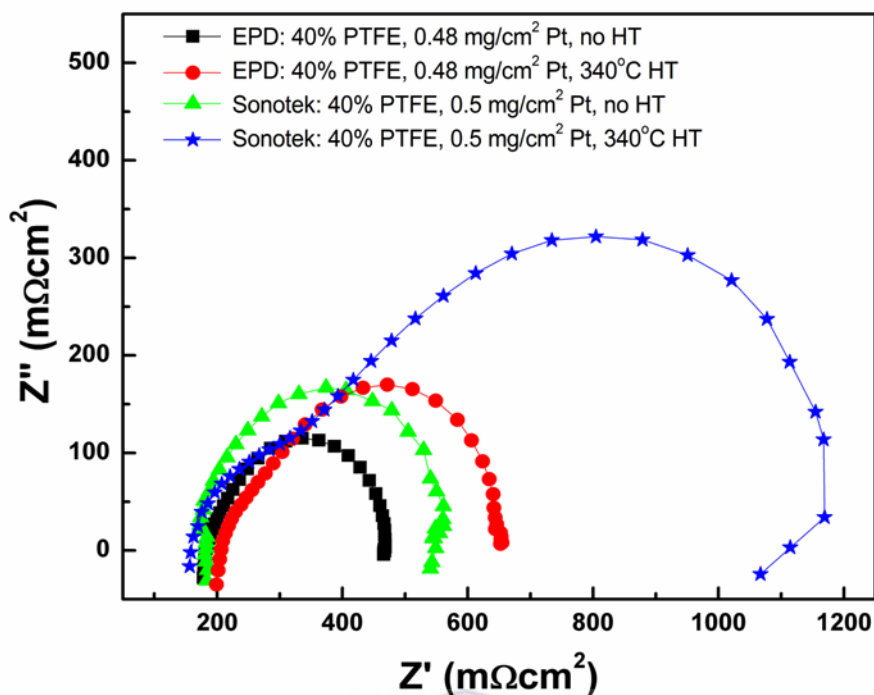
Fig. 5.15: EIS analysis at 0.6V of the EPD and Sonotek MEAs. Operating temperature was 160°C. Air flow rate was 1 slpm and H_2 flow rate was 0.5 slpm.

Fig. 5.16 shows the EIS analysis of the EPD MEAs (no HT) containing PTFE and the Nafion® ionomer in the CLs. Significantly higher charge transfer resistance was observed when the Nafion® ionomer was present in the CL was probably due to the larger catalyst particles formed by the Nafion® ionomer which reduced the ECSA.
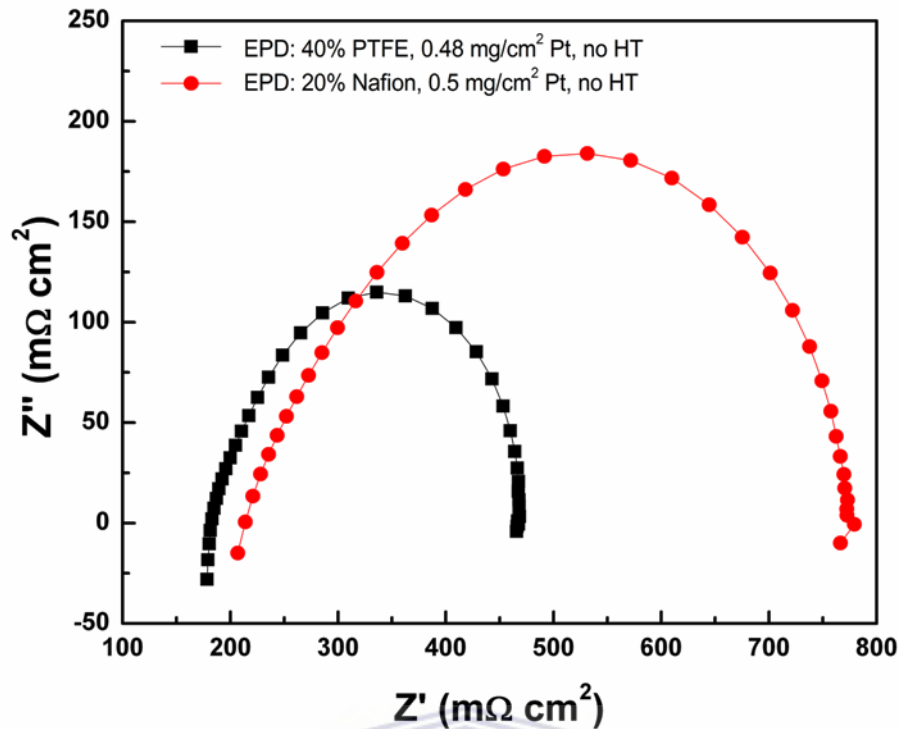
Fig. 5.16: EIS analysis at 0.6V of EPD MEAs (no HT). Operating temperature was 160°C. Air flow rate was 1 slpm and H_2 flow rate was 0.5 slpm.

Figs. 5.15 and **5.16** revealed that the membrane resistances of the MEAs were slightly different therefore *IR* free polarisation curves, where the internal cell resistances were corrected based on the high frequency resistance, was plotted. **Fig. 5.17** shows the IR free polarisation curves of the EPD and Sonotek MEAs. The EPD MEA (no HT) clearly exhibited better electrode kinetics which resulted in the better MEA performance. The *IR* free curves showed that the Sonotek (no HT) and EPD (340 °C) had comparable performances but the Sonotek (no HT) showed slightly better performance under high current conditions.

94
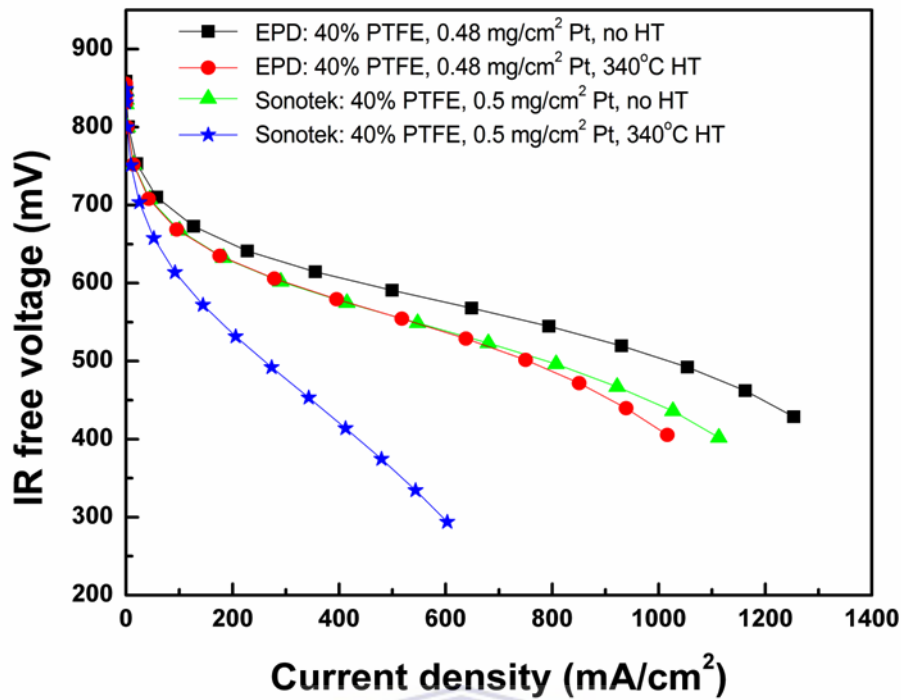
Fig. 5.17: *IR* **free polarisation curves of EPD and Sonotek MEAs. Operating temperature was 160°C. Air flow rate was 1 slpm and** *H₂* **flow rate was 0.5 slpm.**

Fig. 5.18 shows the *IR* free polarisation curves of the EPD MEAs, one containing 0.48 mg/cm² Pt and 40 wt% PTFE and the other containing 0.5 mg/cm² Pt and 20 wt% Nafion® ionomer in both anode and cathode CLs. The EPD MEA with PTFE in the CLs exhibited better performance under high temperature (160 °C) operation compared to the EPD MEA with the Nafion® ionomer in the CLs.
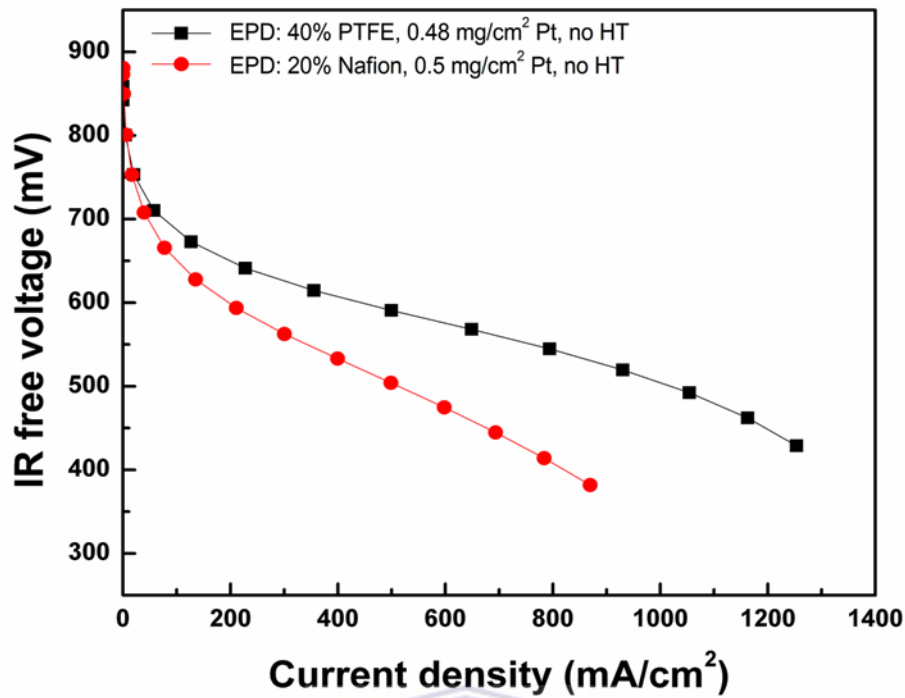
Fig. 5.18: *IR* **free polarisation curves of EPD MEAs (no HT). Operating temperature was 160°C. Air flow rate was 1 slpm and** *H₂* **flow rate was 0.5 slpm.**

Fig. 5.19 shows the stability of the EPD MEAs with PTFE and the Nafion® ionomer in the CLs at a constant cell voltage of 0.55 V. Both MEAs showed stable behaviour over the duration of the test (i.e. 180 hours). The EPD MEA with PTFE in the CL showed double the current density (i.e. ~340 mA/cm^2) compared to the EPD MEA with the Nafion® ionomer in the CL (i.e. ~170 mA/cm^2).
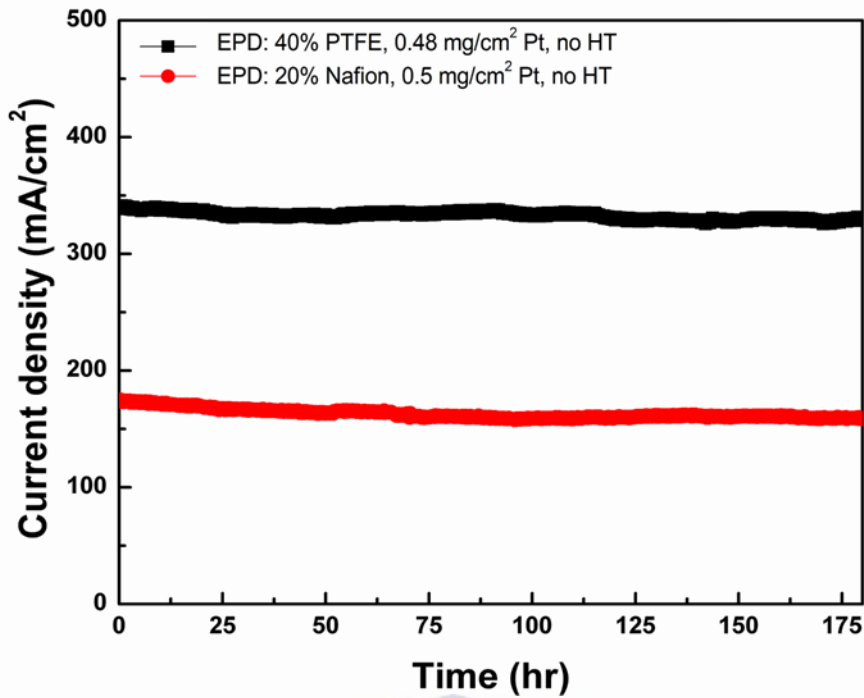
Fig. 5.19: Stability of EPD MEAs (no HT) at 0.55V. Operating temperature was 160°C. Air flow rate was 1 slpm and H_2 flow rate was 0.5 slpm.
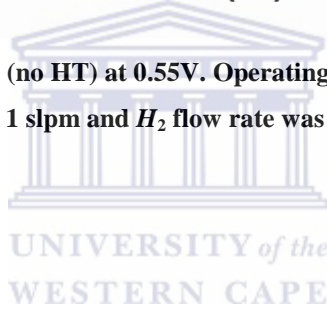
5.3 Conclusions

MEAs for HT-PEMFCs were fabricated *via* the EPD method. Suspensions of *Pt/C*-PTFE particles in IPA with various salt (*NaCl*) concentrations and various pH conditions were studied. *NaCl* concentrations (< 0.1mM) should be considered for the fabrication of the GDEs. The *Pt/*C-PTFE suspensions were stable between pH 3 to 9. At pH 2 and pH values 10 to 12, rapid coagulation of the *Pt/C*-PTFE particles occurred forming unstable catalyst suspensions while the *Pt/C*-Nafion® particles remained stable over the entire pH range studied (i.e. pH 2 to 12).

EPD and Sonotek GDEs/MEAs with PTFE in the CLs were compared under similar test conditions. HR-SEM images revealed cracked but uniform morphologies for the EPD GDEs while the Sonotek GDEs exhibited morphology consisting of small, fine

97

particles as well as larger particles that contained higher PTFE contents. Heat treatment of both GDE types resulted in higher porosity however a lowering in the MEA performance. For the Sonotek GDE, the melting of the PTFE resulted in the covering of the active Pt sites which significantly affected the electrochemical performance of the MEA. Under the test conditions the EPD MEA (no HT) performed better than the EPD MEA (340°C HT) and Sonotek MEAs as revealed by the polarisation measurements. EPD MEAs with PTFE in the CLs yielded better MEA performance compared to the EPD MEA with the Nafion® ionomer in the CLs under high temperature (i.e. 160°C) operation. Stability measurements of the EPD MEAs with PTFE and Nafion® ionomer in the CLs showed that both MEAs reached stable current densities after ~48 hours of activation followed by negligible decrease in current densities over the duration of the stability tests.
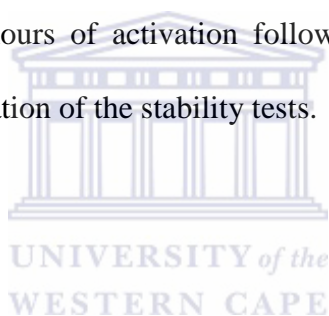
Chapter 6: Integrated electro-surface study of Pt/C aqueous suspensions

6.1 Introduction

The results obtained in chapters 4 and 5 showed that the EPD method was feasible to fabricate GDEs/MEAs for HT-PEMFCs. In these studies, organic based catalyst suspensions were optimised for the fabrication of GDEs for MEAs in HT-PEMFCs. The advantages of using organic solvents include low conductivity and good chemical stability, the absence of electrochemical reactions and joule heating at the electrodes. The disadvantages of using organic suspensions include high cost, volatility, toxicity and flammability. Organic solvents have a low dielectric constant (i.e. dissociation power) inducing a limited particle charge. Higher electric field strengths are thus required to move the particles towards the electrode. There is a strong requirement to reduce the overall cost of PEMFC production for its commercialisation to be realised. Environmental concerns are also the major driving force for developing alternative clean energy technologies. Therefore it becomes more important to develop PEMFC components using environmentally friendly materials.

Water is the most abundant chemical compound on earth and is considered a more suitable alternative to using organic solvents for EPD. The advantages of EPD from aqueous solutions are low cost, benign environmental impact and ease in controlling dispersion and coagulation [112, 135, 162]. Water has a high dielectric constant ($\varepsilon \approx 78.3$) which produces a charge build-up on the particles; therefore low electric field strengths can be applied. The main disadvantage of using aqueous solutions is the electrolysis of water which occurs above the thermodynamic voltages of water

oxidation and reduction. This results in gas formation at the electrodes which affects the quality of the deposit. The application of low voltages are thus limited to low deposition rates and thin deposits [114, 163]. To address the challenges faced by EPD from aqueous solutions it becomes important to obtain a deep understanding about the nature of particle interactions in these suspensions. A theoretical model that accounts for the electrostatic and Van der Waals forces between the *Pt/C* particles in aqueous solutions was developed. The insight obtained from the theoretical model will lay a foundation for future studies of the aqueous *Pt/C* suspensions.

6.1 Aggregative stability and the composition of equilibrium electrolyte solutions

A deep understanding of the nature of the interactions between the particles of suspensions is required for developing and optimising a great variety of technological processes for which it is necessary to maintain the aggregative stability of colloidal systems or, on the contrary, to destabilise the system [164-166]. The behaviour of dilute aqueous suspensions of *Pt/C* containing solutions of salt (*NaCl*), acid (*HCl*) or base (*NaOH*) was studied. The mean particle radius of the *Pt/C* was *a* = 140 nm. The electric potential and charge of the particle surfaces were determined with the help of electrophoretic measurements (*via* the Malvern Zetasizer Nano ZS) conducted for different electrolyte compositions.

While studying aggregation, the coagulation rates for systems with various salt concentrations and various pH values were compared. To inspect the possibility to address all the studied cases in terms of a single time scale parameter which will be referred to as the coagulation time (τ), each of the time dependencies of the "particle

size" (as the instrument determined it) that was obtained for various solution compositions, were analysed. For each of the dependencies, dimension vs. time (τ) was determined by considering the initial stage of coagulation. Finally all the experimental curves were re-plotted by representing the "particle size" as a function of time normalised by the coagulation time (τ), determined for each of the curves separately. The results of implementing this described scheme are represented in **Fig. 6.1** where all the experimental points formed a set that can be fitted by a single smooth curve. Such behaviour revealed that obtaining τ for each of the solution compositions yielded the required information regarding the system's aggregative behaviour.
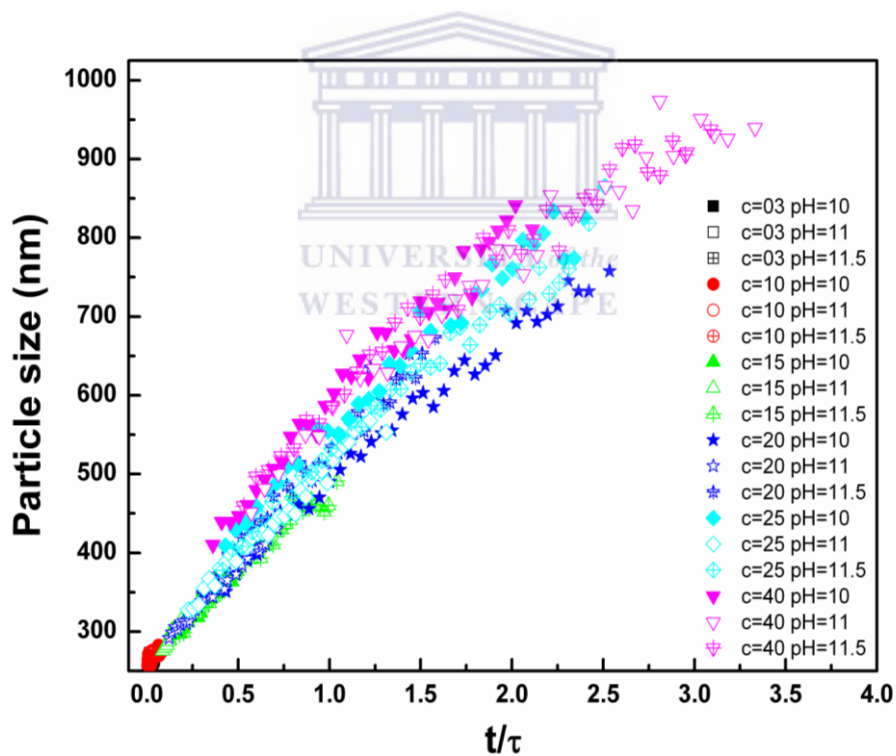
Fig. 6.1. Size of *Pt/C* particles vs. normalised time for different electrolyte solution compositions.

Qualitatively, the observed aggregation of particles was consistent with the DLVO theory [164, 167, 168]. The system remained relatively stable at neutral pH values however the addition of an acid significantly accelerated coagulation which reached

the maximum rate at pH ~3 to 4. At such pH values, as observed from the electrophoretic mobility measurements, the particle charge dramatically decreased and thus weakened the electrostatic repulsion that lead to the acceleration of coagulation.

Fig. 6.2 shows the interaction energy between two particles as a function of the minimum distance between its surfaces. The method of calculation of the interaction energy is given in Section 6.3. Arbitrary parameters were used in the calculations for **Fig. 6.2** to demonstrate the role of the electrostatic mechanism in coagulation and to illustrate the ability of the DLVO theory to describe general trends in the behaviour. For a quantitative comparison, it was necessary to find the particle surface charge or potential which the electrostatic repulsion depended on. These data can be obtained from electrophoretic mobility measurements which should be interpreted by using a theory that does not have limitations in terms of the charge value and the EDL thickness. The latter requirements of the theory are important because of the particle's small size is comparable with the EDL thickness.
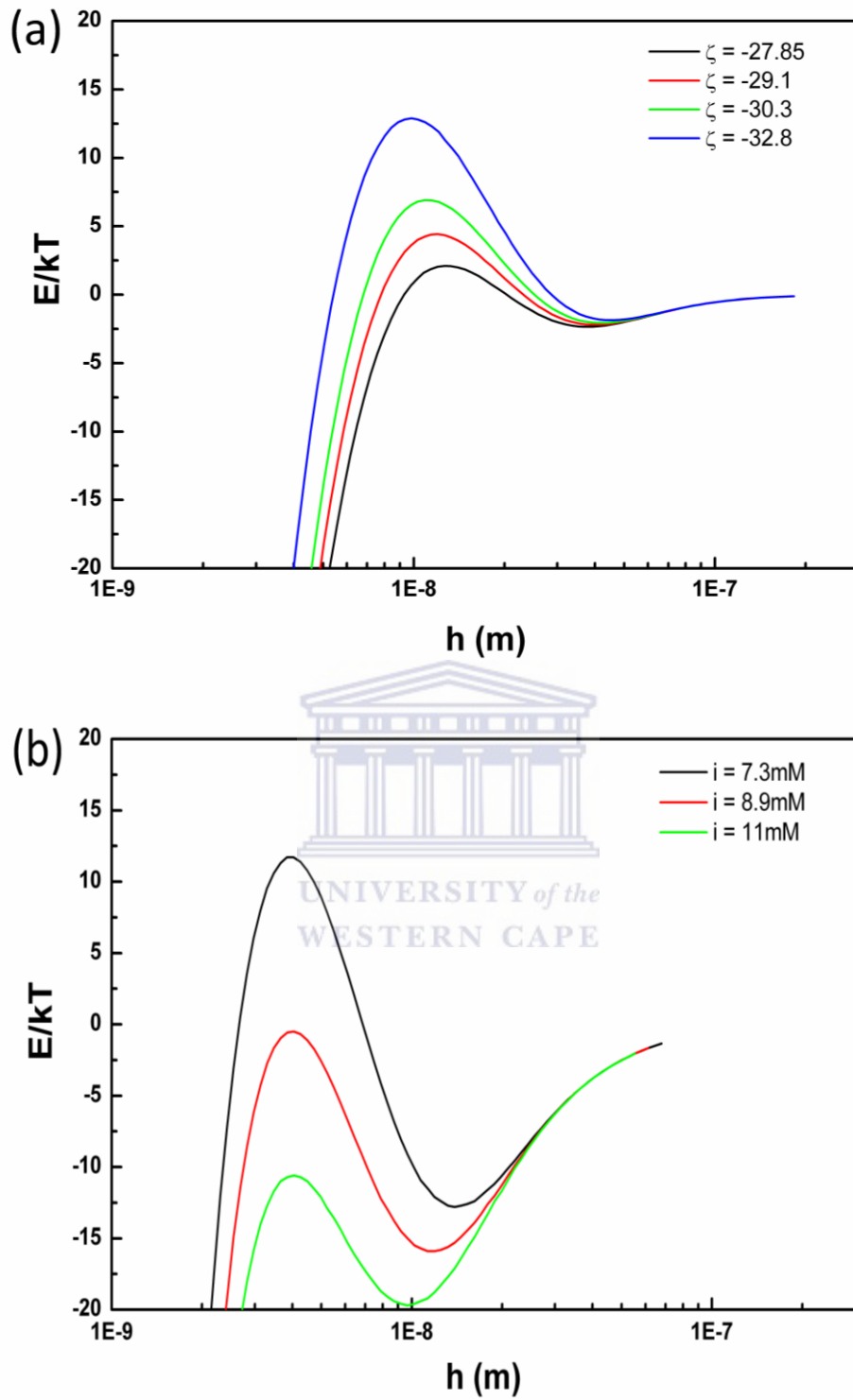
Fig. 6.2: Dependency of the interaction energy on the shortest distance between particle surfaces in a 10⁻³ M electrolyte solution for different (a) surface potentials (ζ) and (b) ionic strengths (i) at ζ = 55.6 mV. Hamaker constant is H = 1.8 x 10⁻²⁰ J.

6.2 Obtaining surface electric potential from electrophoretic measurements

The first step of the analysis was concerned with obtaining the particle equilibrium surface potential (ζ) or the particle interfacial charge density (q) from the particle electrophoretic velocity. The electrophoretic method intended for determining ζ deals with measuring the electrophoretic velocity ($\mathbf{U}_{eph}$) in an external electric field ($\mathbf{E}$). The experimentally measured zeta potential ($\zeta_{\exp}$) is usually calculated from $\mathbf{U}_{eph}$ by employing the classical Smoluchowski [169, 170] formula:

$$\mathbf{U}_{eph} = \frac{\varepsilon \zeta_{\exp}}{\eta} \mathbf{E} \tag{6.1}$$

$\varepsilon \approx 7 \times 10^{-10}$ F/m and $\eta \approx 0.9$ mP.s are the electrolyte solution dielectric constant and viscosity respectively.

Using Eq. (6.1) yields a correct value of the surface potential, i.e. $\zeta_{\exp} = \zeta$ for a sufficiently small value of the Dukhin number (Du) [171]:

$$Du \approx \exp\left(\zeta_{\exp} F z_{cntr} / 2RT\right) / \kappa a \ll 1 \tag{6.2}$$

where a is the particle radius, z_{cntr} is the counterion valence, $F = 9.65 \times 10^4$ C/mol is the Faraday constant, $R = 8.31$ J/(mol.K) is the gas constant, $T = 300$ K is the absolute temperature, κ is the Debye parameter (inverse Debye length) which is expressed as

$$\kappa = F\sqrt{\frac{\sum_k C_k z_k^2}{\varepsilon RT}} \tag{6.3}$$

104

where z_κ and C_κ are the kth ion valence and bulk (infinitely far from the particle) concentration respectively.

When the condition of Eq. (6.2) is violated, the value ζ_{exp} obtained from electrophoretic data by using the simple relationship of Eq. (6.1), noticeably differs from the surface potential (ζ). Violation of the condition of Eq. (6.2) is very typical for submicron (and smaller) particles with high surface potentials. For e.g., while dealing with 10^{-4} N aqueous solution of 1:1 electrolyte, $\zeta \approx 100$ mV and the particle radius ~100 nm, one obtains that $Du \approx 2$. In such a case $\zeta \neq \zeta_{exp}$ and for obtaining ζ one should develop an approach which would enable obtaining ζ by using the measured value ζ_{exp} and other system parameters. This approach should be based on a more general relationship than Eq. (6.1).
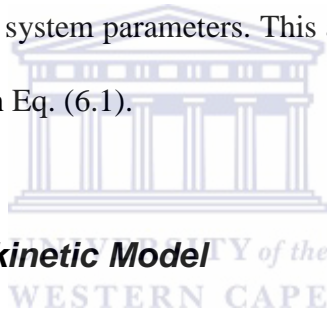
6.2.1. Standard Electrokinetic Model

During the 20th century a number of theoretical approaches were developed for addressing electrophoresis in various situations where the condition of Eq. (6.1) was violated [170-186]. According to the most consistent and convenient formalism [181-187], to determine the electrophoretic velocity, one should solve two boundary value problems in turn. The first of the above problems describes the distribution of electric potential around a particle in the thermodynamic equilibrium state ($\Psi = \Psi(\mathbf{r})$), i.e. in the absence of an externally applied electric field. This problem includes the Poisson-Boltzmann (P-B) equation:

$$\nabla \cdot \nabla \Psi = -\frac{F}{\varepsilon} \sum_k C_k z_k \exp\left(-\Psi z_k F / RT\right) \tag{6.4}$$

where $\nabla = \mathbf{e_n} \partial / \partial x_\mathbf{n}$ ($\mathbf{e_n}$ and $x_\mathbf{n}$ are unit vectors and respective coordinates of the Cartesian coordinate system). The P-B equation, Eq. (6.4) is subject to the boundary conditions:

$$\Psi = \zeta \qquad \text{at the particle surfaces} \qquad (6.5)$$

$$\Psi \to 0 \qquad \text{at infinity} \qquad (6.6)$$

By solving the boundary value problems given by Eqs. (6.4) to (6.6), one obtains the spatial distribution of electric potential ($\Psi(\mathbf{r})$), existing in the thermodynamic equilibrium state. Using the obtained function $\Psi(\mathbf{r}, \zeta)$, the interfacial charge density (q) is determined from the electrostatic condition written in the form:

$$q = -\varepsilon \mathbf{n} \cdot \nabla \Psi \qquad \text{at the particle surfaces} \qquad (6.7)$$
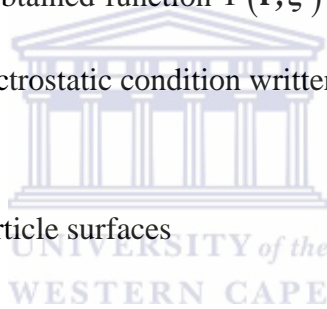
where $\mathbf{n}$ is the unit outward vector normal to the particle surface. The latter equation yields the required relationship between the surface potential and charge density.

The second of the aforementioned problems is formulated for addressing a non-equilibrium regime when an external electric field is applied. The problem formulation contains the function $\Psi(\mathbf{r})$ which is known as the solution of the first problem. The set of governing equations of the second problem includes the continuity equations for individual ionic fluxes and liquid flow and a version of the Stokes equation which accounts for the presence of the electric force acting on the

106

EDL space charge. The flux continuity equation can be represented in the following form:

$$\nabla \cdot \nabla \mu_k - \frac{z_k F}{RT} \nabla \mu_k \cdot \nabla \Psi = -\frac{z_k F}{D_k} \mathbf{u} \cdot \nabla \Psi \qquad (6.8)$$

In Eq. (6.8), $d\mu_k = z_k F d\Phi + d\mu_k^{ch}$ is the differential of the electrochemical potential of the kth ion; Φ is the local electric potential and μ_k^{ch} is the chemical potential of the kth ion. For the general case, μ_k^{ch} depends on all the ion concentrations. However, for an ideal electrolyte solution which is usually considered in electrokinetic studies, $d\mu_k^{ch} = RT dc_k / c_k$ where $c_k = c_k(\mathbf{r})$. When $\mathrm{r} \to \infty$, $c_k(\mathbf{r}) \to C_k$.

The Stokes equation accounting for the electric bulk force, after some transformations, can be represented as

$$\eta \nabla \times \nabla \times \mathbf{u} = -\nabla \Pi - \sum_k C_k \left[\exp\left(-\Psi F z_k / RT\right) - 1 \right] \nabla \mu_k \qquad (6.9)$$

where the effective pressure, $\Pi = p - RT \sum_k C_k \left[\exp\left(-\Psi F z_k / RT\right) - 1 \right]$ signifies the deviation of local pressure (p) from its value defined in the thermodynamic equilibrium state with reference to the solution bulk (the second term on the right hand side of latter equality). The continuity equation for liquid velocity is written in the usual form:

$$\nabla \cdot \mathbf{u} = 0 \qquad (6.10)$$

107

The governing equations, i.e. Eqs. (6.8) to (6.10) are subject to the boundary conditions at the particle surface and infinity. The particle surface is impermeable for ions. The latter requires for the normal flux of the kth ion to be zero. The problem is considered in the reference system linked to the particle. Consequently, the respective conditions take the forms:

$$\mathbf{n} \cdot \nabla \mu_k = 0 \qquad \text{at the particle surfaces} \qquad (6.11)$$

$$\mathbf{u} = 0 \qquad \text{at the particle surfaces} \qquad (6.12)$$

At infinity, a uniform external field strength ($\mathbf{E}$) is imposed with zero concentration gradients. These two physical conditions are expressed with the help of equality:

$$\nabla \mu_k = -F z_k \mathbf{E} \qquad \text{at infinity} \qquad (6.13)$$

One more boundary condition should be set to impose zero total force exerted on the particle. Such a force is the sum of the electrical and mechanical forces and is given by the integration of the sum of the Maxwell and viscous stress tensors over any closed surface containing the particle inside. It is convenient to choose such a surface as a sphere with infinitely large radius. In this case, the electrical force acting and the totally electroneutral volume inside the surface takes of value of zero. Accordingly, the integral of the Maxwell stress tensor over the chosen surface, S_∞ turns out to be zero. As a consequence the required boundary condition takes the form:

$$\oiint_{S_\infty} \left[\Pi \mathbf{I} + \eta \left(\nabla \mathbf{u} + (\nabla \mathbf{u})^* \right) \right] \cdot \mathbf{n}_\infty dS = 0 \qquad (6.14)$$

108

where $\mathbf{I} = \mathbf{e_n}\mathbf{e_n}$, $\mathbf{n_\infty}$ is the unit vector normal to the surface (S_∞). Since the function $\Psi(\mathbf{r})$ is known as a solution of the first boundary value problem given by Eqs. (6.4) to (6.6), Eqs. (6.8) to (6.10) are subject to the boundary conditions of Eqs. (6.11) to (6.14) which yields a closed problem formulation enabling one to find the unknown functions $\mu_k(\mathbf{r})$, $\mathbf{u}(\mathbf{r})$ and $\Pi(\mathbf{r})$. By considering the limit of $r \to \infty$ for the velocity field $\mathbf{u}(\mathbf{r})$ and coming over to the reference system linked to the liquid at infinity, one obtains the electrophoretic velocity as

$$\mathbf{U}_{eph} = -\mathbf{U} = -\lim_{r\to\infty}\mathbf{u}(\mathbf{r}) \tag{6.15}$$

By solving the boundary value problems given by Eqs. (6.4) to (6.6) and Eqs. (6.9) to (6.14) and using the limiting transition of Eq. (6.15), it can be interrelated between the electrophoretic velocity ($\mathbf{U}_{eph}$) and surface potential (ζ) for any electrolyte solution employed in the experiment.

6.2.2. Scalarisation

It is assumed that the particle is a sphere having radius *a*.
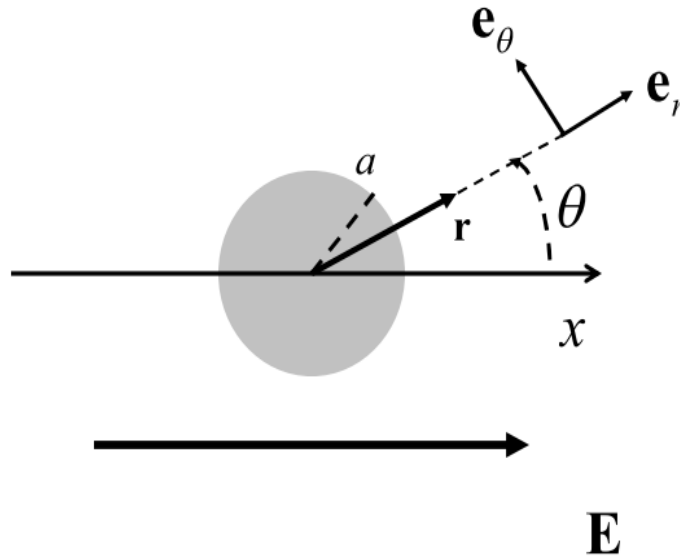
Fig. 6.3: Particle in an external electric field. Spherical coordinate system.

By using the spherical coordinate system shown in **Fig. 6.3** and realising that the system has spherical symmetry in equilibrium, Eqs. (6.4) to (6.7) are rewritten as

$$\frac{1}{r^2}\frac{d}{dr}\left(r^2\frac{d\psi}{dr}\right) = -(\kappa a)^2 \sum_k \xi_k \exp(-\psi z_k) \tag{6.16}$$

$$\psi(a) = \tilde{\zeta}$$
$$\psi(\infty) = 0 \tag{6.17}$$

$$q = -\frac{\varepsilon RT}{Fa}\cdot\frac{d\psi}{\partial r}(1) \tag{6.18}$$

where

$$\xi_k = C_k z_k / C_k z_k^2 \quad \text{(a)} \qquad \psi = \Psi F / RT \quad \text{(b)} \qquad \tilde{\zeta} = \zeta F / RT \quad \text{(c)} \tag{6.19}$$

In the presence of a uniform electric field (**E**) the system has the axial symmetry at infinity. A spherical coordinate system is chosen with unit vectors $\mathbf{e}_r$, $\mathbf{e}_\theta$, $\mathbf{e}_\varphi$ and the

polar axis directed against the vector, **E** (**Fig. 6.3**). The symmetry of the problem dictates the following angle dependencies:

$$\mu_k(r,\theta) = z_k FEa\mathrm{M}_k(r)\cos(\theta) \tag{6.20}$$

$$\mathbf{u}(r,\theta) = E\varepsilon\frac{RT}{\eta F}\left[u_r(r)\cos(\theta)\mathbf{e}_r + u_\theta(r)\sin(\theta)\;\mathbf{e}_\theta\right] \tag{6.21}$$

In Eqs. (6.20) and (6.21), a convenient normalisation of unknown functions are suggested. By combining Eqs. (6.8), (6.20) and (6.21), the following is obtained:

$$\frac{d^2\mathrm{M}_k}{dr^2} + \frac{2}{r}\frac{d\mathrm{M}_k}{dr} - \frac{2}{r^2}\mathrm{M}_k = \left(z_k\frac{d\mathrm{M}_k}{dr} - \frac{3}{2}m_k u_r\right)\frac{d\psi}{dr} \tag{6.22}$$

where the electrokinetic parameter m_k is given by the following formula:

$$m_k = \frac{2}{3}\frac{\varepsilon}{\eta D_k}\left(\frac{RT}{F}\right)^2 \tag{6.23}$$

While using the substitution of Eqs. (6.20) and (6.21), the boundary conditions of Eqs. (6.11) and (6.13) take the following forms:

$$\frac{d\mathrm{M}_k}{dr}(1) = 0 \tag{6.24}$$

$$\frac{d\mathrm{M}_k}{dr}(\infty) = -1 \tag{6.25}$$

For deducing a convenient form of the Stokes equation, Eq. (6.9), one should apply operator $\nabla \times$ to both sides of Eq. (6.9) and substitute the electrochemical potential $\mu_k(r,\theta)$ and velocity $\mathbf{u}(r,\theta)$ in the forms given by Eqs. (6.20) and (6.21). While making use of such a substitution, the functions $u_r(r)$ and $u_\theta(r)$ can be represented in a form which follows from Eq. (6.10):

$$u_r(r) = -\frac{2}{r^2}Y \tag{6.26}$$

$$u_\theta(r) = \frac{1}{r}\frac{dY}{dr} \tag{6.27}$$

The above described transformation scheme leads to the following form of Eq. (6.9):

$$\left(\frac{d^2}{dr^2} - \frac{2}{r^2}\right)^2 Y = -(\kappa a)^2 \sum_k \xi_k \frac{d\exp(-z_k\psi)}{dr} M_k \tag{6.28}$$

Consequently, Eq. (6.28) is subject to boundary conditions that are obtained by combining the boundary conditions given by Eqs. (6.12) and (6.14) with Eqs. (6.21), (6.26) and (6.27). The vector boundary condition of Eq. (6.12) transforms into two scalar conditions:

$$\begin{aligned} Y(1) &= 0 \\ \frac{dY}{dr}(1) &= 0 \end{aligned} \tag{6.29}$$

112

For specifying the boundary condition of Eq. (6.14) which imposes zero total force exerted on the particle, the results of refs [187, 188] was used where this condition was obtained at the spherical cell border. By considering the limiting case of infinitely large cell radius that corresponds to a single particle or very dilute suspension, the boundary condition given by Eq. (6.14) is rewritten in the following form:

$$\left(r^2 \frac{d}{dr} + 2r \right) \left(\frac{d^2}{dr^2} - \frac{2}{r^2} \right) Y \bigg|_{r \to \infty} \to 0 \tag{6.30}$$

The governing Eqs. (6.16), (6.22) and (6.28) are subject to the boundary conditions of Eqs. (6.17), (6.18), (6.24) to (6.27), (6.29) and (6.30) which make up a closed problem formulation that enables one to determine N+2 (N is the number of ions) and the unknown functions $\psi(r)$, $M_k(r)$, and $Y(r)$.
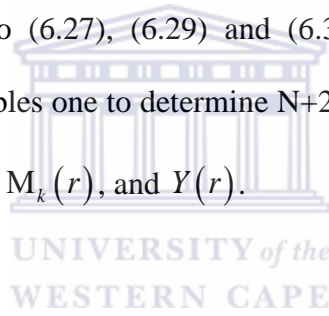
By using the function $Y(r)$ to be obtained, one can determine the electrophoretic mobility, $\chi = \mathbf{U}_{eph}/\mathbf{E}$. The respective expression is obtained by combining Eqs. (6.15), (6.21) and (6.26). While taking into account Eq. (6.1) and the normalisation given by Eq. (6.21), the normalised electrophoretic mobility becomes equal to the normalised zeta potential obtained from experiment, i.e. $\tilde{\zeta}_{exp} = \zeta_{exp} F / RT$. Consequently, one obtains:

$$\tilde{\zeta}_{exp} = 2 \lim_{r \to \infty} \left(\frac{Y}{r^2} \right) \tag{6.31}$$

113

Since $Y = Y\left(r, \tilde{\zeta}, m_k, \kappa a, z_k, \xi_k\right)$, Eq. (6.31) yields the required relationship between the measured zeta potentials ($\tilde{\zeta}_{\exp}$) and actual surface potentials ($\tilde{\zeta}$) for any given composition of electrolyte. In the next section, a numerical algorithm of determining $\tilde{\zeta}$ from a given value of $\tilde{\zeta}_{\exp}$ are discussed based on the solution of the above stated boundary value problem.

6.2.3. Numerical analysis

For the given functions $\psi(r)$ and $M_k(r)$, the distribution $Y(r)$ is obtained by solving the boundary value problems of Eqs. (6.28) to (6.30). The solution of this problem is easily shown to be represented in the following form:

$$
u_r = -\frac{2(\kappa a)^2}{9}\left[\int_1^r \left(-\frac{3}{2r}x^2 + \frac{3}{2}x + \frac{3x^4}{10r^3} - \frac{3r^2}{10x}\right)f(x)dx + \left(\frac{3}{2r} - 1 - \frac{1}{2r^3}\right)A + \left(\frac{3}{10}r^2 - \frac{1}{2} + \frac{1}{5r^3}\right)B\right]
$$

(6.32)

where

$$
f(r) = \sum_k \xi_k \frac{d\exp\left[-z_k\psi(r)\right]}{dr}M_k(r)
$$

(6.33)

$$
A = \int_1^\infty x^2 f(x)dx
$$

(6.34)

$$
B = \int_1^\infty \frac{f(x)}{x}dx
$$

(6.35)

By using Eqs. (6.26), (6.31) and (6.33) to (6.35), the expression for the measured zeta potential ($\tilde{\zeta}_{\exp}$) takes the form:

114

$$\tilde{\zeta}_{exp} = -\frac{(\kappa a)^2}{9} \sum_k \xi_k \int_1^\infty \left(\frac{1}{r} + 2r^2 - 3r \right) \frac{\partial \exp\left[-z_k \psi\left(r, \tilde{\zeta} \right) \right]}{\partial r} M_k\left(r, \tilde{\zeta} \right) dr \qquad (6.36)$$

Eq. (6.36) yields interrelation between the measured zeta potential ($\tilde{\zeta}_{exp}$) and the surface potential ($\tilde{\zeta}$). The dependency on the latter value is embedded into the normalised distributions of the equilibrium potential ($\psi\left(r, \tilde{\zeta} \right)$) and the chemical potential of the kth ion ($M_k\left(r, \tilde{\zeta} \right)$). In ref. [184] an integral relationship similar to Eq. (6.36) was derived for $z{:}z$ electrolyte solution. The relationship given by Eq. (6.36) yields a generalisation of the result of ref [184] for the case of a mixed electrolyte solution. As previously stated, for interrelating $\tilde{\zeta}_{exp}$ and $\tilde{\zeta}$ with the help of Eq. (6.36), one should know the functions $\psi\left(r, \tilde{\zeta} \right)$ and $M_k\left(r, \tilde{\zeta} \right)$. The function $\psi\left(r, \tilde{\zeta} \right)$ is determined separately by solving the boundary value problem given by Eqs. (6.16) and (6.17). Obtaining $M_k\left(r, \tilde{\zeta} \right)$ is associated with a more complex scheme of the solution since the functions $M_k\left(r, \tilde{\zeta} \right)$ is represented in Eq. (6.22) together with u_r, which in turn is expressed through all the functions $M_k\left(r, \tilde{\zeta} \right)$ with the help of an integral relationship of Eq. (6.32). In two limiting cases however, Eq. (6.22) does not contain u_r that allows for obtaining the set of functions $M_k\left(r, \tilde{\zeta} \right)$ by solving Eq. (6.22) subject to the boundary conditions of Eqs. (6.24) and (6.25), separately. The aforementioned two limiting cases are associated with $\kappa a \to \infty$ (Smoluchowski limit [168, 169]) and $\tilde{\zeta} \ll 1$ (Henry case, [170]).

While addressing both the Smoluchowski and Henry case, the right hand side of Eq. (6.22) can be omitted. For the Smoluchowski case, it differs from zero within the vanishingly thin ($\kappa a \rightarrow \infty$) EDL region only. The latter is a result of the presence of $d\psi / dr$ on the right hand side of Eq. (6.22). For the Henry case [170], which yields the linear term in the expansion of electrophoretic mobility by powers of $\tilde{\zeta}$, one should substitute into Eq. (6.36) the function corresponding to $\tilde{\zeta} \equiv 0$, $M_k(r,0)$, since Eq. (6.36) already contains factors proportional to $\tilde{\zeta}$ besides $M_k(r)$. For both limiting cases, Eq. (6.22) transforms into a homogeneous equation whose solution $M_k = M_k(r, \tilde{\zeta}, \kappa a)$, satisfying boundary conditions (6.24) and (6.25) is represented as

$$M_k\left(r, \tilde{\zeta}, \infty\right) = M_k\left(r, 0, \kappa a\right) = M(r) = -r\left(1 + \frac{1}{2r^3}\right) \tag{6.37}$$
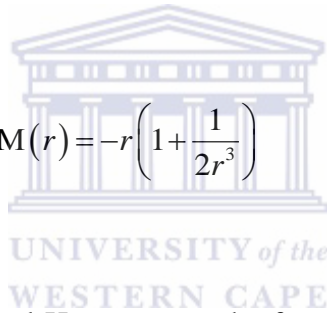
For both the Smoluchowski and Henry cases, the function $M_k(r)$ is independent of $\tilde{\zeta}$ and κa and turns out to be common for all the ions.

Eq. (6.37) can now be substituted into Eq. (6.36) and the derived equation can be combined with Eq. (6.6). The integral obtained in this way should be taken by parts three times in turn while accounting for Eq. (6.17). Finally we arrive at the following simple relationship:

$$\tilde{\zeta}_{\exp} = \tilde{\zeta} - \left(\int_1^\infty \frac{5}{r^6} - \frac{2}{r^4}\right)\psi \, dr \tag{6.38}$$

116

For the Smoluchowski limiting case, $\kappa a \to \infty$, the integral on the right hand side of Eq. (6.38) approaches zero. The latter can be understood while realising that $|\psi|/r^n \le |\zeta| \exp\left[-(r-1)\kappa a\right]$. Consequently, substituting the right hand side of the latter inequality into the integral of Eq. (6.38) one can see that the integral disappears in the limit $\kappa a \to \infty$. Eq. (6.38) and thus Eq. (6.36) lead to the expected result for the Smoluchowski limit:

$$\tilde{\zeta}_{exp} = \tilde{\zeta} \tag{6.39}$$

While dealing with the Henry case, from the boundary value problem given by Eqs. (6.16) and (6.17), one obtains the following:

$$\psi = \tilde{\zeta}\, \frac{\exp\left[-(r-1)\kappa a\right]}{r} + O\left(\zeta^2\right) \tag{6.40}$$

Substituting Eq. (6.40) into (6.38) leads to

$$\tilde{\zeta}_{exp} = \tilde{\zeta}\left\{1 - e^{\kappa a}\left[5\mathrm{E}_7\left(\kappa a\right) - 2\mathrm{E}_5\left(\kappa a\right)\right]\right\} \tag{6.41}$$

where $\mathrm{E}_5\left(x\right)$ and $\mathrm{E}_7\left(x\right)$ are the exponential integrals of the fifth and seventh order respectively. Eq. (6.41) is equivalent to the classical Henry formula [170]. When the

parameter κa is known, Eq. (6.41) allows one to determine the surface potential $\tilde{\zeta}$

for any measured value $\tilde{\zeta}_{\exp}$.

For a given value of κa, the relationship between $\tilde{\zeta}_{\exp}$ and $\tilde{\zeta}$ for each of the

discussed two limiting cases, is independent of electrolyte composition. Such an

independency takes place since the distributions $M_k(r)$ given by Eq. (6.37) become

equal for all the ions. In the general case, the functions $M_k(r)$ attributed to different

ions differ from each other and can be determined with the help of a computational

scheme which is discussed next.

Eq. (6.22) can be solved with respect to $M_k(r)$ by considering the right hand side of

Eq. (6.22) as a known function. When the boundary conditions of Eqs. (6.24) and

(6.25) are satisfied, the obtained solution can be represented in the form:

$$M_k = -\left(1+H_k\right)\left(1+\frac{1}{2r^3}\right)r + \frac{1}{3}\int_1^r\left(r-\frac{x^4}{r}\right)\left(z_k\frac{dM_k}{dx}-\frac{3}{2}m_k u_r\right)\frac{d\psi}{dx}dx \qquad (6.42)$$

where the integration constants H_k are given by

$$H_k = \frac{1}{3}\int_1^\infty\left(z_k\frac{dM_k}{dr}-\frac{3}{2}m_k u_r\right)\frac{d\psi}{dr}dr \qquad (6.43)$$

Next the set of integral relationships given by Eqs. (6.32), (6.33) and (6.42) are considered. According to these relationships, in a point with coordinate $r = r_*$, the functions $u_r(r)$ and $M_k(r)$ take values, $u_r(r_*)$ and $M_k(r_*)$, that are expressed through the distributions $M_k(r)$ for $1 < r < r_*$. Consequently, both $u_r(r)$ and $M_k(r)$ can be determined numerically by gradually increasing r in the integrals on the right hand sides of Eqs. (6.32) and (6.42). Recall that when $r \to \infty$, the asymptotic value approached by $u_r(r)$ is $(-\tilde{\zeta}_{\exp})$.

The previous discussion defines the steps of the numerical scheme to be used: (i) the function $\psi(r, \tilde{\zeta}, \kappa a)$ is determined by solving the P-B boundary value problem given by Eqs. (6.16) and (6.17), (ii) certain initial values of the integration constants A, B and H_k represented in Eqs. (6.32) and (6.42) are assumed, (iii) while using Eqs. (6.32), (6.33) and (6.42), the functions $u_r(r)$ and $M_k(r)$ are computed by gradually increasing r, (iv) the obtained distribution is used for the redetermination of A, B and H_k with the help of Eqs. (6.34), (6.35) and (6.43) respectively.

6.3 Analysis of coagulation dynamics

In this section, an attempt is made to interpret the experimental data obtained while studying the rate of dispersed system coagulation. The coagulation process results in changes of size distribution of the particles and the dynamics of such a process can be characterised by a time scale parameter (τ) given by

$$\tau = \tau_{Sm} W \qquad (6.44)$$

119

where $\tau_{Sm} = 3\eta / 4k_B Tn$ ($k_B \approx 1.4.10^{-23}$ J/K is the Boltzmann constant; n is the initial concentration of particles) is the time scale parameter characterising the so-called rapid or Smoluchowski coagulation which takes place when 100% of particle collisions lead to forming doublets. In Eq. (6.44), the factor W describes the increase in τ when the efficiency of particle collisions becomes less than 100% due to the repulsive forces between the particles:

$$W = \int_0^\infty \frac{\exp\left[G(h)/k_B T\right]}{(1+h)^2} dh \tag{6.45}$$

In Eq. (6.24), $h = (r_{BA} - 2a)/2a$ where r_{BA} is the distance between the particle centers; $G(h)$ is the free energy of a system of two interacting particles defined with reference to the state when the particles are separated by an infinitely large distance. The function $G(h)$ can be obtained by calculating the mechanical work produced by the interaction forces while the particles are displaced from the state when the distance between their centres is $r_{BA} = 2a(h+1)$ to infinitely large distances.

We consider interactions due to the electrostatic and Van der Waals forces whose contributions $G_{el}(h)$ and $G_W(h)$ into $G(h)$ are assumed to be additive:

$$G(h) = G_{el}(h) + G_W(h) \tag{6.46}$$

120

In the next section, it is considered how to obtain each of these contributions for the system under consideration.

6.3.1. Electrostatic repulsion

Two particles separated by a distance (l) and bearing either constant surface potential (ζ) or constant surface charge (q) that are determined from the electrophoretic mobility measurements following the scheme described in the previous sections, are considered. Both the particle charge and potential are assumed to be common for the particles. The system containing two particles and the infinite volume of surrounding electrolyte solution is considered to be in thermodynamic and mechanical equilibrium. Consequently, the distribution of electric potential (Ψ) is obtained as a solution of the P-B problem given by Eqs. (6.4) to (6.6) with a reservation that in the limiting case of constant surface potentials, the common potential (ζ) is set at the surfaces of each of the particles. For analysing the case of constant surface charge at the surface of each of the particles, one should use Eq. (6.7) instead of Eq. (6.5) for setting the electrostatic boundary condition. By using the solution $\Psi(\mathbf{r})$ of the P-B problem, one can determine the force ($\mathbf{X}$) acting on any of the two particles. To this end, the stress tensor ($\boldsymbol{\sigma}$) should be integrated over the particle (S_p) as

$$\mathbf{X} = \oiint_{S_p} \boldsymbol{\sigma} \cdot \mathbf{n} \, dS \tag{6.47}$$

where the stress tensor $\boldsymbol{\sigma}$ is

121

$$\boldsymbol{\sigma} = \varepsilon \nabla \Psi \nabla \Psi - \frac{\varepsilon}{2} \mathbf{I} \nabla \Psi \cdot \nabla \Psi - \mathbf{I} p \tag{6.48}$$

On the right hand side of Eq. (6.48), the first two terms represent the Maxwell tensor and the third term gives the contribution of pressure (p) into the total stresses. The local pressure can be interrelated with the local value of potential with the help of the mechanical equilibrium condition which can be written in the form:

$$\nabla \cdot \boldsymbol{\sigma} = 0 \tag{6.49}$$

By combining Eqs. (6.4), (6.48) and (6.49) and after some transformations, one obtains

$$p - p_\infty = \sum_k C_k \left[\exp\left(-\Psi F z_k / RT \right) - 1 \right] \tag{6.50}$$

where p_∞ is the pressure infinitely far from the particles.

Using Eq. (6.49) and the tensor analog of the Gauss theorem one can prove the following equality:

$$\oiint_{S_p} \boldsymbol{\sigma} \cdot \mathbf{n}_A \, dS = -\frac{1}{2a(1+h)} \int_{S_{sym}} \boldsymbol{\sigma} \cdot \mathbf{r}_{\mathbf{BA}} \, dS \tag{6.51}$$

122

where S_{sym} is the symmetry plane and $\mathbf{r_{BA}}$ is the vector whose origin and end coincides with the centres of particles B and A respectively. Now the force $\mathbf{X}_A$ and $\mathbf{X}_B$ exerted on the particle A and B respectively, is considered. This is obtained while combining Eqs. (6.47), (6.48), (6.50) and (6.51) and using symmetry reasons:

$$\mathbf{X}_A = \frac{\mathbf{r_{BA}}}{2a(1+h)}X = -\frac{\mathbf{r_{AB}}}{2a(1+h)}X = -\mathbf{X}_B \tag{6.52}$$

where the force magnitude (X), which is obviously common for both the particles, is expressed as an integral over the symmetry plane (S_{sym}):

$$X = \int_{S_{sym}} \left\{ \frac{\varepsilon}{2}\left[\nabla\Psi - \frac{\mathbf{r_{BA}}}{4a^2(1+h)^2}(\mathbf{r_{BA}} \cdot \nabla\Psi) \right]^2 + RT\sum_k C_k \left[\exp(-z_k\Psi F / RT) - 1 \right] \right\} dS \tag{6.53}$$

Eqs. (6.52) and (6.53) enable one to compute the electrostatic interaction force exerted on the interacting particles when the equilibrium electric potential distribution ($\Psi(\mathbf{r})$) is known. At a given particle radius, $X = X(h)$. Consequently, the contribution of electrostatic forces into the interaction free energy ($G_{el}(h)$) is determined as

$$G_{el}(h) = \int_h^\infty X(h)\,dh \tag{6.54}$$

123

In summary the electrostatic contribution to the system's free energy is obtained by the integral of Eq. (6.54) where the interaction force magnitude ($X(h)$) is computed by using Eq. (6.53) which depends on the potential distribution ($\Psi(\mathbf{r})$). The latter distribution is obtained as a solution of the non-linear boundary value problem given by the governing Eq. (6.4) subject to boundary conditions Eq. (6.5) (for constant surface potential) or Eq. (6.7) (for constant surface charge). Both the latter conditions are set at the surface of each of the particles. One more boundary condition is given by Eq. (6.6).

For $\kappa a \gg 1$, the above outlined scheme of obtaining $G_{el}(h)$ is simplified while using the Derjaguin approximation [164, 165] according to which the zone around the particle contact is represented as a system of quasi-flat segments where the 1D P-B equation is solved. Within the frameworks of the Derjaguin approximation, the first term in round brackets in Eq. (6.53) is omitted for being small at $\kappa a \gg 1$. For moderate κa, the Derjaguin approximation is not applicable. In such a case, one should solve the complete P-B problem and take into account all the terms represented in Eq. (6.53). The analysis of this type is given in ref. [189]. For the calculation, the approach stated in [189], was used.

By following ref. [189], the distribution $\Psi(\mathbf{r})$ and the electrostatic interaction force magnitude will be computed with the help of a bispherical coordinate system. Taking into account the problem axial symmetry, one can represent the ∇ operator in terms of new coordinates (β, ν) as

$$\nabla = \frac{\cosh(v) - \cos(\beta)}{a\sqrt{h(h+2)}} \left(\mathbf{e}_\beta \frac{\partial}{\partial \beta} + \mathbf{e}_v \frac{\partial}{\partial v} \right) \tag{6.55}$$

where $\mathbf{e}_\beta$ and $\mathbf{e}_v$ are the unit vectors of the bispherical coordinate system. Differentiating $\mathbf{e}_\beta$ and $\mathbf{e}_v$ satisfies the following rules:

$$\frac{\partial \mathbf{e}_\beta}{\partial \beta} = \mathbf{e}_v \frac{\sinh(v)}{\cosh(v) - \cos(\beta)} \text{ (a)} \qquad \frac{\partial \mathbf{e}_\beta}{\partial v} = -\mathbf{e}_v \frac{\sin(\beta)}{\cosh(v) - \cos(\beta)} \qquad \text{(b)}$$

$$\frac{\partial \mathbf{e}_v}{\partial v} = \mathbf{e}_\beta \frac{\sin(\beta)}{\cosh(v) - \cos(\beta)} \text{ (c)} \qquad \frac{\partial \mathbf{e}_v}{\partial \beta} = -\mathbf{e}_\beta \frac{\sinh(v)}{\cosh(v) - \cos(\beta)} \qquad \text{(d)} \quad (6.56)$$

By combining Eqs. (6.4), (6.19 a and b), (6.55) and (6.56), the following dimensionless version of the P-B equation written in bispherical coordinate system is obtained:

$$\frac{\left[\cosh(v) - \cos(\beta)\right]^3}{h(h+2)\cdot \sin\beta} \left[\frac{\partial}{\partial \beta} \left(\frac{\sin\beta}{\cosh(v) - \cos(\beta)} \cdot \frac{\partial \psi}{\partial \beta} \right) + \frac{\partial}{\partial v} \left(\frac{\sin\beta}{\cosh(v) - \cos(\beta)} \cdot \frac{\partial \psi}{\partial v} \right) \right]$$
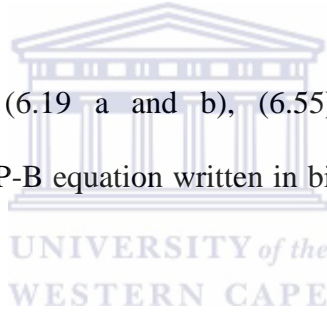
$$= -(\kappa a)^2 \sum_k \xi_k \exp(-\psi z_k) \tag{6.57}$$

Boundary conditions at the particle surface are rewritten as

$$\psi(\beta, v_0) = \tilde{\zeta} \text{ (constant potential)} \tag{6.58}$$

or

$$\frac{\cosh(v_0) - \cos(\beta)}{\kappa a \sqrt{h(h+2)}} \frac{\partial \psi}{\partial v}(\beta, v_0) = \tilde{q} \text{ (constant charge)} \tag{6.59}$$

125

where $\tilde{q} = qF / \varepsilon\kappa RT$. The coordinate surface, $v = v_0$, coincides with the surface of one of the particles. Instead of setting the same condition at the surface of another particle, the system symmetry which allows setting the following condition at the symmetry planes was used:

$$\frac{\partial \psi}{\partial v}(\beta,0) = 0 \tag{6.60}$$

and

$$\frac{\partial \psi}{\partial \beta}(0,v) = 0$$
$$\frac{\partial \psi}{\partial \beta}(\pi,v) = 0 \tag{6.61}$$

Eq. (6.57) subject to the boundary conditions of Eqs. (6.58) or (6.59), (6.60) and (6.61) form a closed problem formulation for obtaining the function $\psi(\beta,v)$. This problem is numerically solved by conducting a discretisation of the second order differential equation for obtaining equations to be solved with the help of an iteration scheme. The iteration method of Newton - Raphson is used that enables reducing the non-linear problem to several linear iterations. Finally, the obtained function $\psi(\beta,0)$ is substituted into the integral of Eq. (6.53) which is rewritten in the form:

$$X(h) = \pi\varepsilon\left(\frac{RT}{F}\right)^2 \int_0^\pi \left\{ \frac{(\kappa a)^2 h(h+2)}{\left[1-\cos(\beta)\right]^2} \sum_k \frac{\xi_k}{z_k}\left[\exp(-z_k\psi(\beta,0))-1\right] + \left[\frac{\partial\psi}{\partial\beta}(\beta,0)\right] \right\} \sin(\beta)d\beta$$

$$\tag{6.62}$$

126

The obtained function $X(h)$ is substituted into the integral of Eq. (6.62) to obtain $G_{el}(h)$.

6.3.2. Van der Waals forces

The second term $G_W(h)$ on the right hand side of Eq. (6.46) is now determined. When the dimensions of interacting bodies having volumes dV_1 and dV_2 are much less than the distance (r) between them, the Van der Waals interaction energy (dG_W) is given in the form [190]:

$$dG_W = -\frac{H \cdot dV_1 \cdot dV_2}{r^6} \tag{6.63}$$

where H is the Hamaker constant which depends on the materials of both the bodies and the surrounding medium. The negative sign of energy on the right hand side of Eq. (6.63) corresponds to the attraction. For obtaining the energy of interaction between two spheres, the spheres are represented as sets of infinitely small elements and interaction energies for each of the element pairs consisting of elements that belong to different spheres, summated. Such a calculation which is based on the assumptions that the contribution of interaction of different pairs are additive, yields the well-known result [190]:

$$G_W = -\frac{\pi^2 H}{6} \cdot \left[\frac{4 \cdot (\varpi^2 - 2)}{\varpi^2 \cdot (\varpi^2 - 4)} + \ln\left(1 - \frac{4}{\varpi^2}\right) \right] \tag{6.64}$$

where

127

$$\varpi = \frac{r}{a} = \frac{2a+h}{a} \qquad\qquad (6.65)$$

6.4 Results and discussion

6.4.1 Correlation between electrophoretic and stability data

The calculation scheme stated in Section 6.2 enables obtaining the experimentally measured value of zeta potential (ζ_{exp}) from its actual value (ζ) (within the frameworks of the employed standard electrokinetic model) for arbitrary values of ζ and κa. By solving the inverse problem, one can determine both the surface potential (ζ) and charge density (q) for ζ_{exp} and κa that are known from experiment. The parameter κa was obtained by determining particle radii and specifying Eq. (6.3) for ternary electrolytes employed in the experiments, namely the mixtures of *NaCl* with either *NaOH* or *HClO₄*. The calculation scheme of Section 6.2 is also specified for these electrolyte solutions.
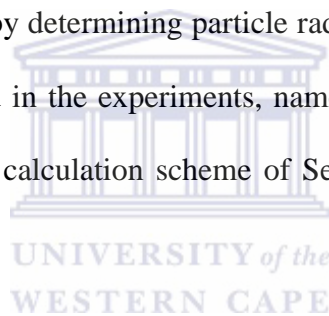
The results of the first set of experiments were obtained while measuring the zeta potential for sufficiently low concentrations of salt (i.e. 10^{-4} M and 10^{-3} M) within a wide pH range which includes low and high pH values where the suspension becomes unstable (Section 6.1). **Figs. 6.4 a** and **b** shows the measured (ζ_{exp}) and actual surface potentials (ζ) as functions of the solution pH for 10^{-4} M and 10^{-3} M concentrations of salt. The presented data were obtained for two solid phase (i.e. *Pt/C*) concentrations, 0.03 and 0.1 g/l, for which the suspension can be considered as infinitely diluted. Accordingly, the data, except for a few points, turned out to be close to each other.
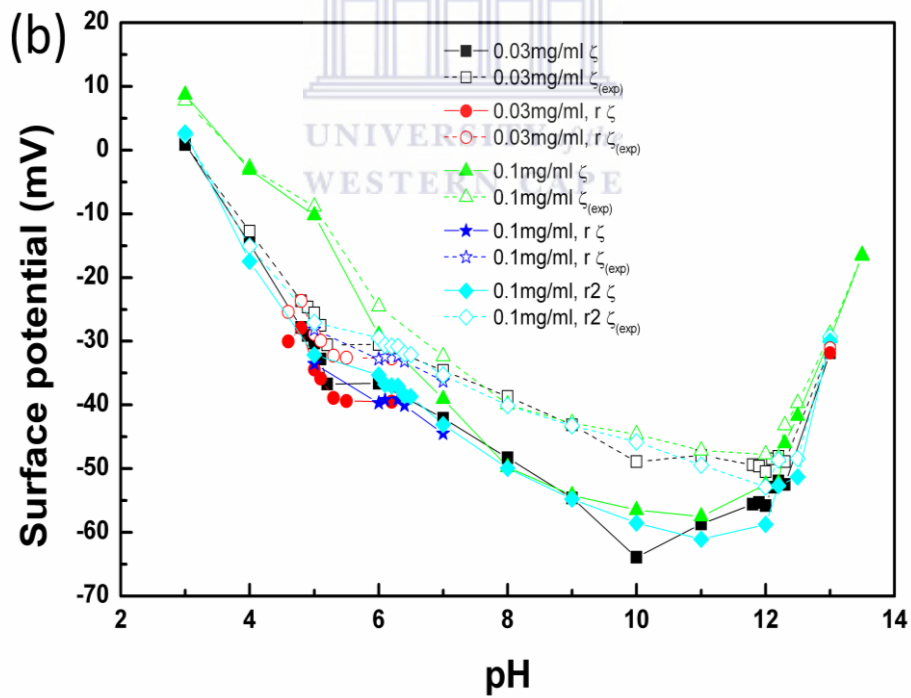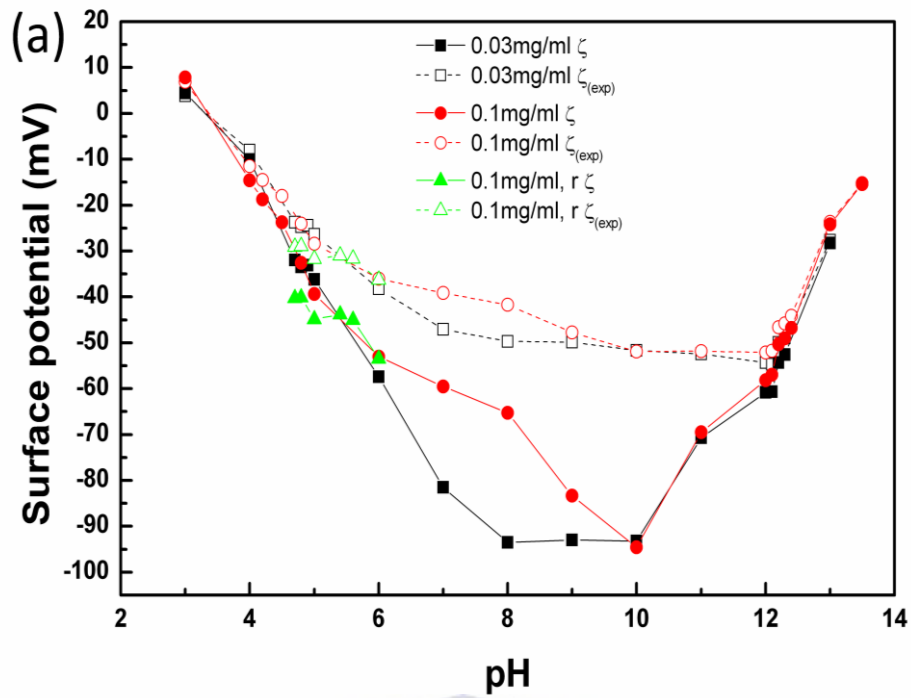
Fig. 6.4. Dependency of the surface potential of *Pt/C* on pH at salt concentrations (a) 10^{-4} M and (b) 10^{-3} M.

In both graphs while increasing the pH within the acidic region, the surface potential decreased and reached zero at rather low pH values. With the further increase of pH, the potential became negative and increased by absolute values until reaching a maximum magnitude within the basic range but close to the neutral pH values. The final decrease of potential was observed within the basic region. It is important to note that ζ_{exp} and ζ nearly coincided for acidic and basic pH values. However, within the neutral pH range the actual potential magnitude ($\left|\zeta\right|$) exceeded that of the measured value ($\left|\zeta_{exp}\right|$) by a factor of about 2 and 1.2 for the salt concentrations 10^{-4} M and 10^{-3} M respectively. The initial assumption about weakening the electrostatic interactions at high and low pH values (discussed in Section 6.1) correlates with the data of electrophoretic measurements.
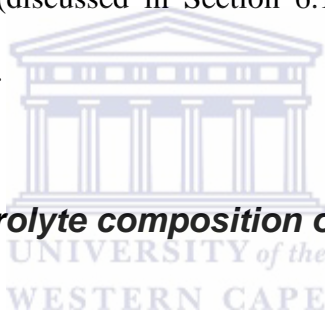
6.4.2. Influence of electrolyte composition on surface potential and charge

Two mechanisms can be suggested whose simultaneous contributions can lead to the behaviour of zeta potentials displayed in **Figs. 6.4 a** and **b**, namely (i) the changes of charge due to the binding-releasing of H^+ and OH^-, and (ii) the decrease of potential due to compressing the EDL which occurs while increasing the ionic strength and thereby decreasing the Debye length. The latter mechanism manifests itself when the base (i.e. $NaOH$) concentration becomes sufficiently high.

To understand the role of the first mechanism, the behaviour of surface charge density as a function of pH at constant salt concentrations (i.e. 10^{-4} M and 10^{-3} M in **Figs. 6.5 a** and **b**) was considered.
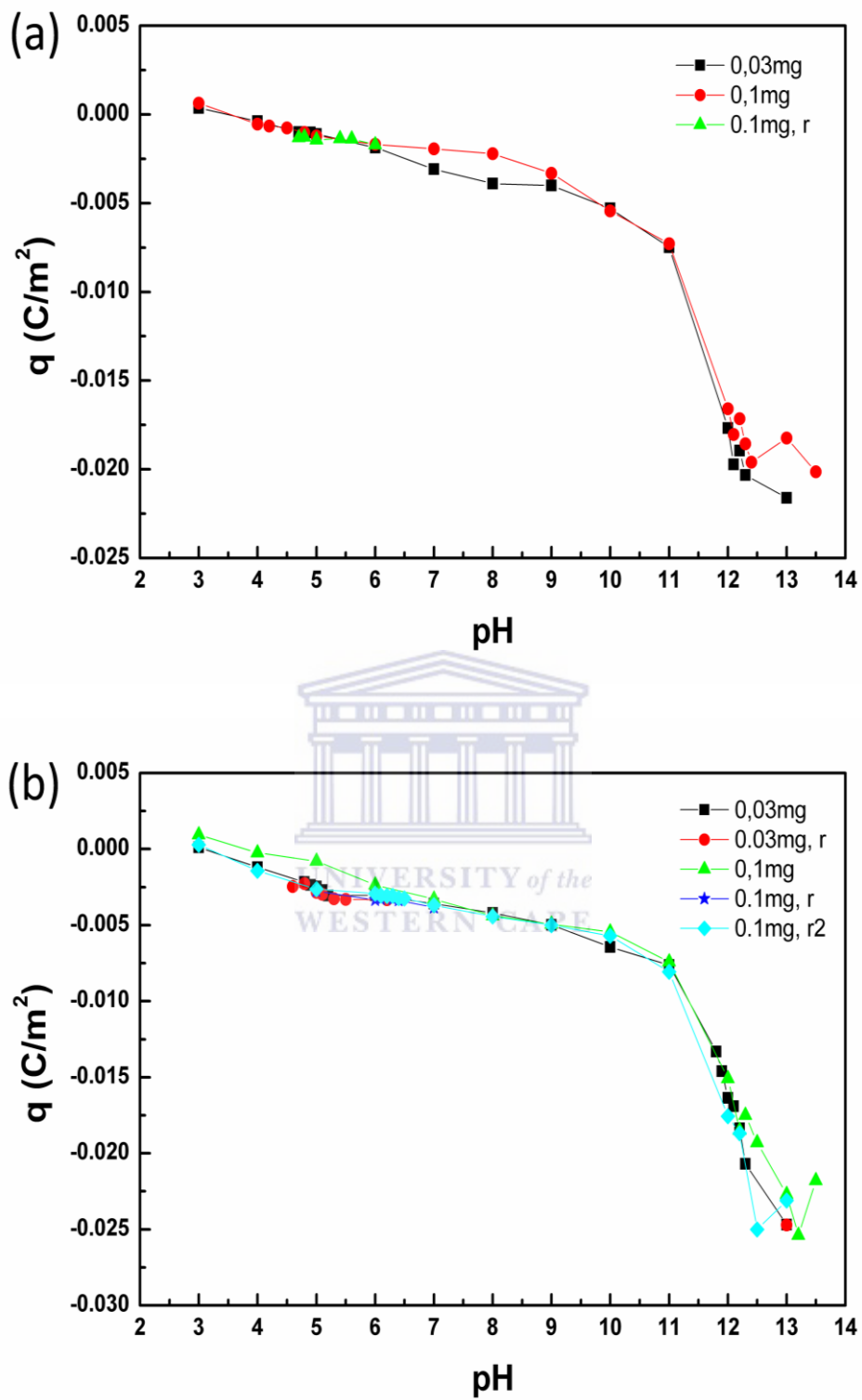
Fig. 6.5: Dependency of the surface charge density of *Pt/C* on pH at salt concentrations (a) 10^{-4}M and (b) 10^{-3}M.

At low pH values, the particle charge was negative and then increased in magnitude with the increase of pH as far as it reached a value of 0.02 C/m² in a concentrated base solution. In the basic pH range, the behaviour of the curves looks similar to the Langmuir isotherm. At neutral and acidic pH, such adsorption saturation was not observed. Instead there was a slow linear dependency on pH while the concentrations of H^+ (and OH^-) change substantially. Note that the pH value axis in **Fig. 6.5** is decimal logarithmic with respect to the OH^- concentration. Perhaps such behaviour was a result of the existence of two types of surface ionic groups with different properties. Saturation of groups that belong to one of the types can coincide at pH = ~7 with the start of ion binding (or liberating) by groups of another type.

To better understand which ions take part in formation the surface charge, all the ion concentrations in the immediate vicinity of the surface (C_k^S), was determined by using the Boltzmann distribution:

$$C_k^S = C_k \exp\left(-\tilde{\zeta} z_k\right)$$

(6.66)

These concentrations were plotted against the surface charge density (q) which is calculated for each of the points by using the electrolyte composition and the calculated value of surface potential corresponding to this point. In the general case, at a given ζ, any relation between C_k^S and q should also depend on the electrolyte composition. The set of points C_k^S vs. q, plotted for different electrolyte compositions in various experiments was spread over a certain area in the graph. While assuming that the surface charge was formed due to the interaction (dissociation or adsorption)

132

of surface groups with the kth sort of ions, only the surface charge was completely defined by the concentration (C_k^S) and the parameters of the adsorption (dissociation-binding) isotherm was independent of the electrolyte composition. In such a case, the corresponding points in the graph $C_k^S(q)$ were expected to lie on a smooth line (the isotherm) or to be close to it (taking into account the experimental error).

The positions of points plotted in the graph of **Fig. 6.6** for H^+, Na^+ and Cl^- are now considered.
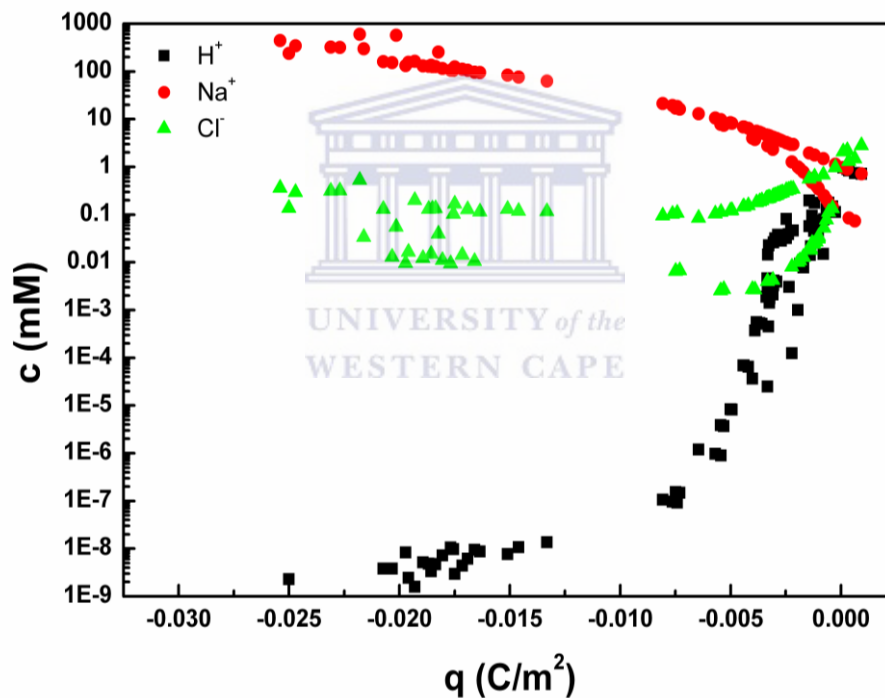
Fig. 6.6: Concentrations of H^+, Na^+ and Cl^- that correspond to given values of surface charge in various experiments.

Fig. 6.6 reveals that Na^+ and Cl^- do not form the surface charge because the points corresponding to these ions approached a smooth line only at a relatively large charge, i.e. $|\sigma| > 0.005$ C/m^2. Since the positions of points corresponding to the H^+ make up a set which can be approximated by a smooth line, it was concluded that the charge is

133

formed either by hydrogen or by hydroxyl ions. By using the present approach, it was impossible to distinguish whether the charge is formed by the binding of OH^- or releasing H^+. The charge in this region strongly depends on pH (see **Fig. 6.5 a** and **b**). Near the maximum charge (i.e. $|\sigma| > 0.02$ C/m^2), a set of points plotted for Na^+ that nearly forms a smooth line, is observed. However, it does not reveal that the Na^+ form a charge. The latter can be understood while realising that Na^+ is the only counterion (i.e. cation) in the solution. Under the conditions of a locally flat EDL which is satisfied when ζ_{exp} and ζ are close to each other and sufficiently high ζ, one can establish a relationship between the charge (q) and the concentration ($C_{Na^+}^s$):

$$q = -\frac{\varepsilon RT}{F} \cdot \frac{\partial \tilde{\Psi}}{\partial r}\bigg|_{r=a} \approx -\sqrt{2\varepsilon RT}\sqrt{C_{Na^+}^s} \tag{6.67}$$

Eq. (6.67) strictly interrelates the charge density and the concentration ($C_{Na^+}^s$) and is independent of the electrolyte composition. This interrelation however is not an adsorption isotherm.

The second set of experiments was conducted to obtain a better understanding about the mechanisms of decrease of the surface potential magnitude at high pH value (as shown in **Figs. 6.4 a** and **b).**
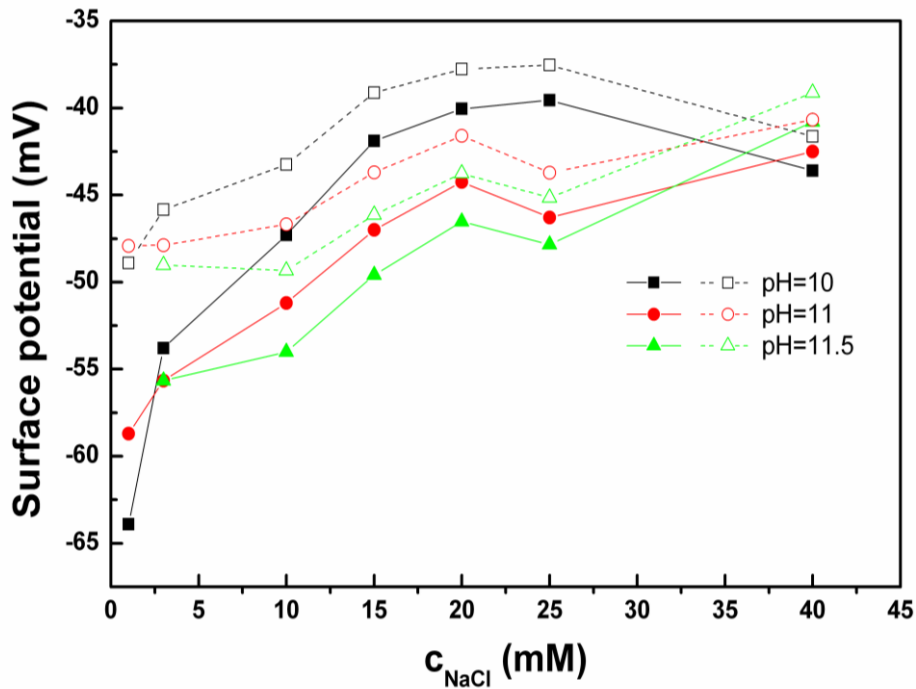
Fig. 6.7: Dependency of the surface potential on salt concentration for various pH values: ζ - solid lines ζ_{exp} - dashed lines.

The major objective of these experiments was to determine whether the decrease in surface potential was due to the compression of the EDL or changes in the ion adsorption or binding. To achieve this, the ionic strength was increased by adding a salt (i.e. *NaCl*) instead of the base (i.e. *NaOH*). The pH was constant in each of experiments. **Fig. 6.7** shows the dependency of surface potential on the salt concentration. The difference in behaviour of the curves plotted for ζ and ζ_{exp} was noticeable but less than that for the case of low salt concentrations. The absolute value of surface potential decreased except for two points in high the concentration range which deviated from the decreasing eye guide within the limits of experimental error. Obtaining the surface charge density corresponding to the surface potential (ζ) and the ion concentrations shown in **Fig. 6.7** yielded a remarkable result. Although ζ

decreased in magnitude with increasing salt concentration, the surface charge magnitude increased (see **Fig. 6.8**).
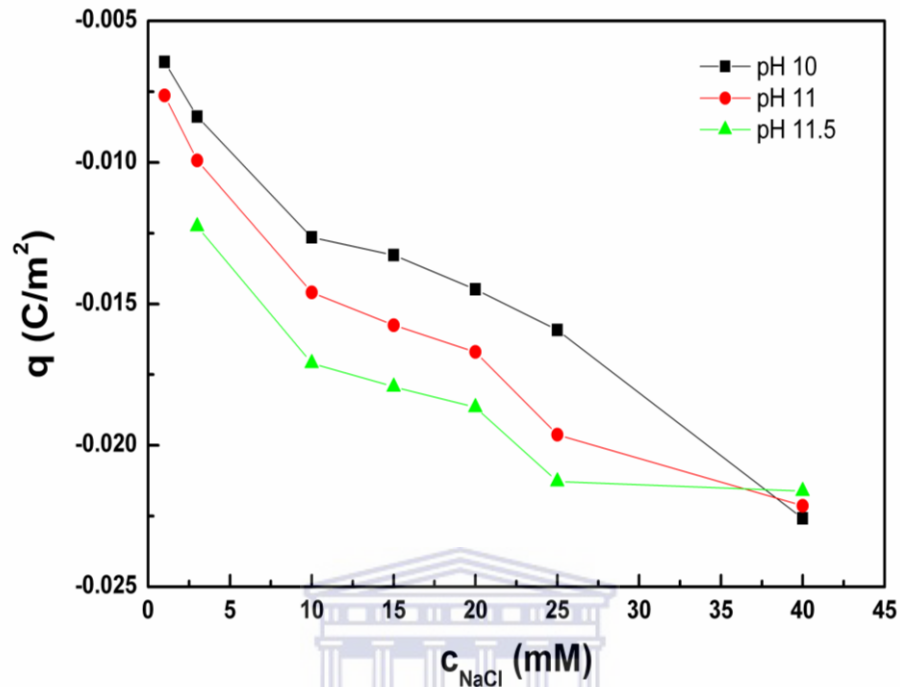
Fig. 6.8: Dependencies of the surface charge density on salt concentration for various fixed pH values.

The opposite behaviour of the potential and charge observed in **Figs. 6.7** and **6.8** is explained by the increasing of the OH^- concentration and the decreasing of the H^+ concentration in the immediate vicinity of particle surface (see Eq. (6.66)). Accordingly, the adsorption of potential defining OH^- (and/or desorption of H^+) increased. The behaviour of charge as a function of the salt concentration additionally revealed that the surface charge was formed by the adsorption or desorption of the OH^- or H^+ respectively. The charge magnitude turned out to be higher at higher pH values observed from **Fig. 6.8** by positions of the respective curves.

It can be expected that at a given ionic strength, the charge will be higher for systems having a higher pH value. To verify this, in **Fig. 6.9** a graph similar to the plot of **Fig. 6.8** was constructed, however for the horizontal axis, the ionic strength of mixed electrolyte solution (i.e. *NaCl* and *NaOH*) was used instead of the salt concentration.
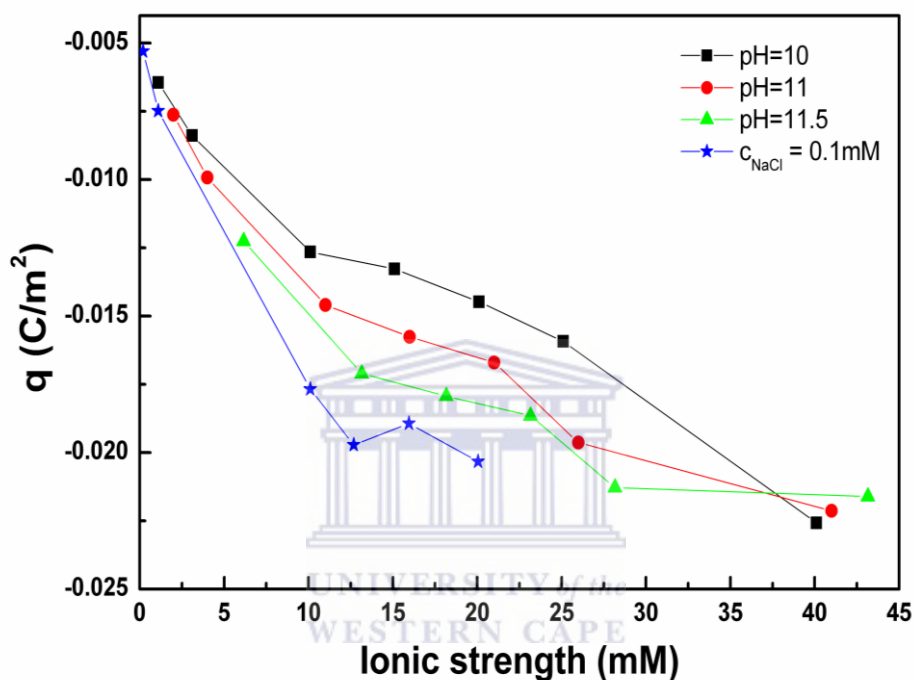
Fig. 6.9: Dependency of the surface charge density on ionic strength at various pH values.

Fig. 6.9 shows that the points corresponding to higher pH values simultaneously corresponded to higher charge magnitudes at same the ionic strength. Accordingly, the lowest curve which corresponds to the highest charge magnitude was plotted for the lowest salt concentration when almost the whole solution ionic strength was provided by the *NaOH* ions.

In summary, the binding of OH^- (and/or liberating of H^+) is the major mechanism of charging the particle surface. While increasing the electrolyte solution pH, an increase

of the negative surface charge by absolute value was observed. In spite of this, the negative surface potential magnitude decreased due to the compression of the EDL which occurred due to the increasing ionic strength.

6.4.3 Applicability of the Standard Electrokinetic Model

While considering coagulation, the particle interaction energy can be compared with the energy of thermal motion (kT) which for room temperature is about 4.10^{-21} J. Using the Hamaker constant ($\sim 10^{-20}$ J), the Van der Waals energy was estimated to be significant at distances of the order of the particle radius (Eq. (6.64)). At such distances, the Derjaguin approximation [164] is not applicable. The contribution of the electrostatic repulsion is important up to several Debye lengths. When the EDL is sufficiently thin, rapid coagulation can occur in the secondary minimum.

For all samples in the experiments, a linear dependency of aggregate size on time was observed. The latter allowed the determination of the time scale parameter of coagulation for each experiment and to obtain those values of the Hamaker parameter that corresponded to the time scale parameter and the surface potential obtained from electrophoretic measurements. To evaluate the slowing of coagulation, from which the Hamaker constant is determined, the coagulation time on the Smoluchowski time was divided which is evaluated as $\tau_{Sm} = 300$ s for 0.03 g/l weight concentration of *Pt/*C particles and $\tau_{Sm} = 100$ s for the more concentrated system with 0.1 g/l concentration of the *Pt/C* particles. The results of the calculations are presented in **Table 6.1**. If the DLVO theory would describe the aggregation in the present system accurately, the same value of the Hamaker constant would be obtained for all experiments. Unfortunately as it follows from **Table 6.1**, the calculated Hamaker

constant substantially varied. Prior to making the final conclusions from the data in **Table 6.1**, those which are characterised by coagulation time to the Smoluchowski value (τ_{Sm}) given by Eq. (6.44), were excluded. Also the cases where coagulation was so slow that the changes of aggregate size were small and comparable with the experimental error were excluded. The tabulated data where coagulation time behaved strange were also excluded. By using the remaining data, we determined the average values separately for acidic and basic ranges. In the last column of **Table 6.1**, the cases considered for the acidic and basic ranges are signified by letters *a* and *b* respectively.
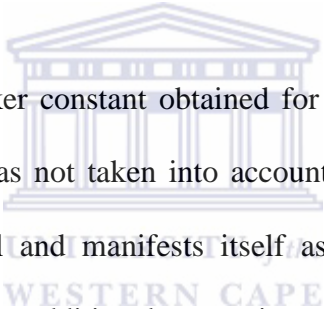
pH	$\zeta_{(exp)}$ (mV)	Coagulation time (s)	Ionic strength (mM)	ζ (mV)	σ (C/m^2)	H (J)	
0.03 mg/ml *Pt/C* in 0.1 mM *NaCl*, coagulation time without interaction $\tau0$=300s							
3	3.85	298.1	1.100	4.42	0.000357	3.095E-22	
4	-7.98	328.6	0.200	-10.07	-0.00038	5.348E-21	
4.7	-23.7	1064.3	0.120	-32.00	-0.00101	1.042E-19	a
4.8	-24.7	2003	0.116	-33.50	-0.00104	1.149E-19	a
4.9	-24.4	12801	0.113	-33.10	-0.00102	1.046E-19	a
5	-26.4	47170	0.110	-36.20	-0.00111	1.255E-19	a
6	-38.2	23673	0.101	-57.40	-0.00187	3.737E-19	
8	-49.7	88057	0.101	-93.50	-0.0039	8.311E-19	
9	-49.8	192478	0.110	-93.00	-0.00401	7.558E-19	
10	-51.7	104606	0.200	-93.25	-0.0053	4.492E-19	
11	-52.4	148052	1.100	-70.70	-0.00749	8.329E-20	
12	-54.3	39018	10.100	-60.85	-0.01768	1.682E-20	b
12.1	-54.7	11620	12.689	-60.70	-0.01972	1.478E-20	b
12.2	-49.9	2792.3	15.949	-54.30	-0.01894	1.086E-20	b
12.3	-48.9	451.3	20.053	-52.60	-0.02033	9.256E-21	
13	-27.7	171.1	100.100	-28.30	-0.02161	1.473E-19	
0.03 mg/ml *Pt/C* in 1mM *NaCl*, coagulation time without interaction $\tau0$=300s							
3	0.88	380.215136	2.000	0.98	1.05E-04		
4	-12.7	589.153291	1.100	-14.67	-0.0012	2.842E-21	
4.8	-23.7	1171.85846	1.016	-27.85	-0.00216	1.483E-20	a
4.9	-24.65	1792.53255	1.013	-29.10	-0.00237	1.610E-20	a
5	-25.6	2777.72166	1.010	-30.30	-0.00247	1.737E-20	a
5.1	-27.55	3742.66225	1.008	-32.80	-0.0027	2.062E-20	a
5.2	-30.6	28784.2432	1.006	-36.70	-0.00306	2.536E-20	
11.8	-49.4	24200.445	7.310	-55.60	-0.01332	1.728E-20	
11.9	-49.6	9979.02001	8.943	-55.30	-0.0146	1.538E-20	
12	-50.5	47019.3864	11.000	-55.80	-0.01636	1.367E-20	
12.1	-48.5	2458.15181	13.589	-52.90	-0.01691	1.134E-20	b
12.2	-48.1	1831.41644	16.849	-51.96	-0.01836	9.755E-21	b
12.3	-48.9	1387.91573	20.953	-52.50	-2.07E-02	8.838E-21	b
13	-31.0	369.968241	101.000	-31.80	-2.47E-02	1.433E-21	
0.03mg/ml *Pt/C* in 1mM *NaCl* repeats, coagulation time without interaction $\tau0$=300s							
4.6	-25.4	337.449217	1.025	-30.05	-0.00247	1.907E-20	
4.8	-23.7	315.181773	1.016	-27.90	-0.00227	1.660E-20	
5	-28.9	1134.12405	1.010	-34.45	-0.00285	2.393E-20	a
5.1	-29.9	1665.31577	1.008	-35.85	-0.00298	2.575E-20	a
5.3	-32.3	33497.6963	1.005	-38.90	-0.00327	2.844E-20	
5.5	-32.6	32355.9786	1.003	-39.40	-0.00332	2.931E-20	
6.2	-32.7	40451.8417	1.001	-39.50	-0.00333	2.937E-20	
0.1mg/ml *Pt/C* in 0.1mM *NaCl*, coagulation time without interaction $\tau0$=100s							
3	6.85	152.550966	1.100	7.87	0.000637	2.549E-22	
4	-11.5	76.866651	0.200	-14.60	-0.00055	2.273E-20	
4.2	-14.6	388.909118	0.163	-18.75	-0.00065	2.091E-20	a
4.5	-18.0	943.820157	0.132	-23.70	-0.00076	4.289E-20	a

5	-28.4	39064.9471	0.110	-39.40	-0.00123	1.490E-19	
6	-36.0	31945.8662	0.101	-53.00	-0.00169	3.103E-19	
7	-39.2	45888.024	0.100	-59.50	-0.00195	3.914E-19	
8	-41.7	60168.5818	0.101	-65.30	-0.00222	4.600E-19	
9	-47.8	45573.7537	0.110	-83.30	-0.00333	6.443E-19	
10	-51.9	33575.1656	0.200	-94.60	-0.00545	4.582E-19	
11	-51.8	18330.8826	1.100	-69.50	-0.0073	8.162E-20	
12	-52.1	17527.9879	10.100	-58.15	-0.0166	1.546E-20	
12.1	-51.7	2813.28198	12.689	-56.95	-0.01805	1.331E-20	b
12.2	-46.6	1019.51999	15.949	-50.35	-0.01715	9.420E-21	b
12.3	-45.8	146.452545	20.053	-49.05	-0.01857	8.149E-21	
12.4	-44.1	143.653295	25.219	-46.80	-0.0196	6.576E-21	
13	-23.7	721.941213	100.100	-24.20	-0.01824	6.732E-22	
13.5	-15.2	545.963125	316.328	-15.40	-0.02014	8.049E-23	
0.1mg/ml *Pt/C* in 0.1mM *NaCl* repeats, coagulation time without interaction τ0=100s							
4.7	-29.1	6018.24953	0.120	-40.30	-0.0013	1.548E-19	a
4.8	-28.9	8911.66667	0.116	-40.10	-0.00128	1.557E-19	a
5	-31.7	16686.0759	0.110	-44.90	-0.00143	2.057E-19	
5.4	-31.0	28693.617	0.104	-43.85	-0.00136	2.021E-19	
5.6	-31.6	24780.1887	0.103	-45.00	-0.00139	2.177E-19	
6	-36.3	38727.9412	0.101	-53.50	-0.00171	3.151E-19	
0.1mg/ml *Pt/C* in 1mM *NaCl*, coagulation time without interaction τ0=100s							
3	7.77	200.516072	2.000	8.70	0.000936	1.749E-22	
5	-8.88	155.378789	1.010	-10.25	-0.0008	9.985E-22	
6	-24.6	403.432586	1.001	-29.00	-0.00235	7.568E-22	a
7	-32.3	17819.2295	1.000	-39.05	-0.00328	2.846E-20	
8	-39.9	89526.9028	1.001	-49.75	-0.0044	4.618E-20	
9	-42.9	21544.9531	1.010	-54.20	-0.00494	5.539E-20	
10	-44.6	14432.6854	1.100	-56.50	-0.00544	5.686E-20	
11	-47.2	22483.3366	2.000	-57.50	-0.00742	3.972E-20	
12	-47.7	203930.992	11.000	-52.50	-0.01508	1.183E-20	
12.2	-48.3	16506.7805	16.849	-52.25	-0.01849	9.487E-21	
12.3	-43.2	1283.4414	20.953	-46.00	-0.0175	6.769E-21	b
12.5	-39.7	93.1881072	32.623	-41.70	-0.01931	4.705E-21	
13	-28.8	314.056075	101.000	-29.50	-0.02272	1.145E-21	
13.5	-16.4	299.612135	317.228	-16.60	-0.02179	1.207E-22	
0.1mg/ml *Pt/C* in 1mM *NaCl* repeats, coagulation time without interaction τ0=100s							
5	-28.2	220.668795	1.010	-33.55	-0.00277	2.314E-20	
6	-32.8	894.712644	1.001	-39.70	-0.00335	3.164E-20	a
6.1	-32.5	601.771404	1.001	-39.20	-0.0033	3.114E-20	a
6.3	-32.4	1902.24475	1.001	-39.10	-0.00329	3.009E-20	a
6.4	-33.1	5206.99029	1.000	-40.10	-0.00338	3.102E-20	a
7	-36.3	33992.2078	1.000	-44.50	-0.00383	3.727E-20	

Table 6.1: Measured quantities: zeta potential (ζ_{exp}), coagulation time (τ) and ionic strength (i).

Calculated quantities: surface potential (ζ), surface charge density (q) and Hamaker constant

(H).

For the basic range, we obtained the Hamaker constant of 1.30 x 10^{-20} J ($\pm$0.30 x 10^{-20} J) (the standard deviation is presented in the parentheses) when the salt concentration was 10^{-4} M. A Hamaker constant of -0.92 x 10^{-20} J ($\pm$0.19 x 10^{-20} J), within the standard deviation, was obtained in the same basic range however at a higher salt concentration (i.e. 10^{-3} M). In acidic medium the average Hamaker constant of -10.29 x 10^{-20} J ($\pm$4.85 x 10^{-20} J) turned out to be larger, especially for the case of the lower salt concentration (i.e. 10^{-4} M). At the salt concentration of 10^{-3} M, the increase was smaller, i.e. Hamaker constant of 2.21 x 10^{-20} J ($\pm$0.95 x 10^{-20} J) and were near the upper limit of the above result predicted for the basic region (accounting for standard deviation).

A higher value of the Hamaker constant obtained for the acidic region revealed an additional attraction which was not taken into account within the framework of the standard electrokinetic model and manifests itself as an apparent increase in the Hamaker constant. Such an additional attraction can be associated with the heterogeneity of surfaces which often leads to the appearance of an attractive mean force between the surfaces bearing mosaic charge. A more profound role of heterogeneity was expected for higher electrolyte concentrations. However, even at the lower ionic strengths, the EDL was relatively thin compared with the size of the particles ($\kappa a \approx 5$). Hence, sufficiently large regions with different charge densities can manifest themselves. Recall that the solid sample (i.e. *Pt/*C) consisted of carbon particle supports modified by metallic *Pt*. Accordingly the surface heterogeneity is quite possible.

In **Table 6.2**, the results of calculating the coagulation times and respective estimations of the Hamaker constant for the second set of experiments whose results are illustrated in **Figs. 6.7** to **6.9**, are presented. The results of the calculations that were conducted while assuming the surface potential to be independent on the distance between colliding particles are also presented.

The electrolyte concentration is the major parameter defining the coagulation rate since the electrolyte concentration defines both the ionic strength and the EDL thickness. When the salt concentration was lower than 10 mM, coagulation was nearly absent. At 15 mM, the coagulation occurred at a noticeable rate which increased at 20 mM. At salt concentrations of 25 mM and 40 mM, the electrostatic repulsion does not affect the coagulation which is characterised by the Smoluchowski rate. The mean Hamaker constant computed for the salt concentration range 15 to 20 mM (here the result was most reliable), was $H \approx 0.71 \times 10^{-10}$ J ($\pm 0.12 \times 10^{-10}$ J). This value was lower than the estimates given for the low salt concentrations which were presented before. The smaller Hamaker parameter means slower coagulation than would be obtained according to the theory.

NaCl (mM)	pH	$\zeta_{(exp)}$ (mV)	Coagulation time (s)	Ionic strength (mM)	ζ (mV)	σ (C/m^2)	H ζ = const. (J)
3	10	-45.8	22066.4	3.1	-53.8	-0.0084	2.71E-20
3	11	-47.9	38687.7	4	-55.65	-0.0099	2.46E-20
3	11.5	-49.0	27237.4	6.162278	-55.65	-0.0123	1.91E-20
10	10	-43.2	11371.7	10.1	-47.3	-0.0126	1.06E-20
10	11	-46.7	30236.4	11	-51.2	-0.0146	1.17E-20
10	11.5	-49.3	25450.2	13.16228	-54	-0.0171	1.17E-20
15	10	-39.1	1407.5	15.1	-41.9	-0.0133	6.87E-21
15	11	-43.7	1770.6	16	-47	-0.0158	8.31E-21
15	11.5	-46.1	857.2	18.16228	-49.6	-0.0179	8.67E-21
20	10	-37.8	352.2	20.1	-40.05	-0.0145	5.57E-21
20	11	-41.6	1251.7	21	-44.25	-0.0167	6.38E-21
20	11.5	-43.8	565.5	23.16228	-46.53	-0.0187	6.77E-21
25	10	-37.5	355.8	25.1	-39.55	-0.0159	4.80E-21
25	11	-43.7	681.2	26	-46.3	-0.0196	6.26E-21
25	11.5	-45.2	368.8	28.16228	-47.85	-0.0213	6.48E-21
40	10	-41.6	422.5	40.1	-43.6	-0.0226	4.46E-21
40	11	-40.7	267.9	41	-42.5	-0.0221	4.34E-21
40	11.5	-39.1	289.1	43.16228	-40.8	-0.0216	3.86E-21

Table 6.2: Initial data and results of calculating the Hamaker constants for assumptions: 0.03g/l *Pt/C* in various *NaCl* concentrations and pH values, Smoluchowski coagulation time (τ_{Sm}) = 300s.
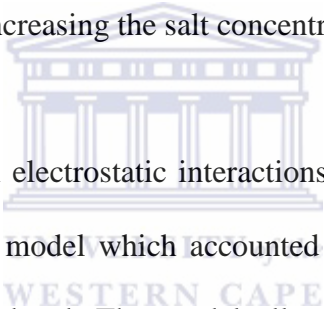
6.5 Conclusions

The influence of the electrolyte composition on the aggregative stability of a diluted suspension of *Pt/C* particles was studied and the following behaviour of the dispersed system under consideration was experimentally established. The system remained relatively stable at neutral pH and started to coagulate upon addition of an acid. While adding a base (i.e. *NaOH*), the system was stable as far as the pH reached a value of ~12.2. The system coagulated with the further increase of the pH and the coagulation was more rapid than in the aforementioned case of low pH. The coagulation threshold which was observed at high pH values turned out to be independent of the salt concentration in contrast to that observed at low pH values.

144

An attempt was made to explain the discussed behaviour through the variation of electrostatic repulsion forces that are addressed by using the DLVO theory [164, 166, 167]. For example, the observed dependency of stability on pH can occur due to the variation of surface charge density. Such a variation takes place because the changes of pH affect both OH^- and H^+ adsorption or the dissociation degree of interfacial ionogenic groups. Another mechanism manifests itself at sufficiently large deviations of pH from its neutral value (i.e. pH = 7). For such a case, the pH changes affects the ionic strength and thus the Debye screening length thereby changing the electrostatic interaction forces even at constant interfacial charge. The mechanism associated with changing the Debye length is also expected to be responsible for the decrease of electrostatic repulsion while increasing the salt concentration.

To ensure that the changes in electrostatic interactions do define the dependency of stability on pH, a theoretical model which accounted for electrostatic and Van der Waals interactions was considered. The model allowed addressing the interaction energy as a function of distance between the particles for arbitrary values of surface potentials and the ratio of the Debye to particle radius. The computed interaction energy was employed for predicting the coagulation time which was the major parameter being determined during the stability experiment.

To obtain the necessary information about the dependencies of surface potential and charge on electrolyte composition, the particle zeta potentials was measured and the obtained results was corrected using the Standard Electrokinetic Model. The calculation conducted on this basis demonstrated that, within some ranges of ion

145

concentrations, the surface potential, which is employed in the stability model, has noticeably higher magnitude than the measured zeta potential.

The correctness of the proposed model was checked by computing the Hamaker constant from different experiments conducted under various electrolyte compositions. Such calculations should give the same value of the Hamaker constant within the limits of measurement accuracy. However, the Hamaker constants obtained changed from one experiment to another. In the case of high solution pH values, the variation was not too significant and one can conclude that the model enables addressing the system behaviour at least quantitatively. For low pH values, the computed Hamaker constants varied substantially and displayed anomalously high values. Supposedly such behaviour was a manifestation of the surface heterogeneity which can be expected for the studied particles (i.e. *Pt/C*).
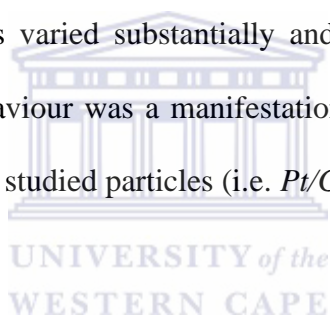
Chapter 7: Final conclusions, Recommendations, Future work and Outputs

7.1 Final conclusions

The *Pt/C* nano-particles were studied in organic and aqueous solutions under various pH conditions and salt concentrations. Optimum organic suspensions were selected to fabricate the GDEs/MEAs and tested under HT-PEMFCs conditions. To determine the feasibility of the EPD method as a suitable fabrication method, the best performing EPD MEAs were compared to MEAs fabricated *via* spraying methods. The EPD MEAs exhibited slightly higher performance (~12% increase in peak power) compared to the ultrasonically sprayed MEAs and significantly higher performance compared to the hand sprayed MEA (~73% increase in peak power). A comparison between two EPD MEAs containing the Nafion® ionomer and PTFE in its CLs, revealed significantly higher (almost double) performance when PTFE was incorporated into the CLs.

The experimentally obtained zeta potential and size data of the *Pt/C* nano-particles in aqueous solutions were used to develop a theoretical model that described the nature interactions between the *Pt/C* particles. The model allowed addressing the interaction energy as a function of distance between the particles for arbitrary values of surface potentials and the ratio of the Debye to particle radius. The correctness of the proposed model was checked by computing the Hamaker constant from various experiments conducted under different electrolyte compositions. Contrary to expected, the obtained Hamaker constants changed from one experiment to another. In the case of high solution pH values, the variation was not too significant, and it was

concluded that the model enables addressing the system behaviour, at least, quantitatively. For low pH values, the computed Hamaker constant varies substantially and takes anomalously high values. Supposedly, such behaviour was a manifestation of the surface heterogeneity which can be expected for the *Pt/C* particles.

7.2 Recommendations

While fabricating GDEs *via* EPD, better deposition of the *Pt/C*-Nafion particles compared to the *Pt/C*-PTFE particles was observed. The MEAs with CLs containing the Nafion® ionomer did not yield high MEA performances needed to reduce the expensive *Pt* catalyst requirement for reducing overall MEA cost. Due to the high reproducibility and fast deposition times observed when the *Pt/*C-Nafion® suspensions was used, the EPD method seems more suitable for fabricating GDEs for MEAs in LT-PEMFCs where lower *Pt* loadings are required and where the Nafion® ionomer performs optimally as an active component of the CL. The lower *Pt* requirements for LT-PEMFCs would result in very thin CLs which requires short deposition times and would minimise crack formation during the drying process. For HT-PEMFCs, alternative polymers and ionomers suitable for high temperature operation and that readily deposits under the influence of an externally applied electric field should be studied.

7.3 Future work

Much insight was obtained from the study of aqueous *Pt/C* suspensions which laid the foundation for future studies. Future work will focus on the deposition of the *Pt/C*

particles from aqueous solutions without the influence of an externally applied electric field. Movement of particles will be obtained *via* concentration gradients under special suspension conditions. The objective of such a study will be to eliminate the occurrence of electrochemical reactions at the electrodes when a voltage is applied. The non-conductive nature of the ABPBI membrane used in HT-PEMFCs prevents the direct EPD of the *Pt/C* particles onto the membrane. Therefore the deposition of the *Pt/C via* such an "electroless" method would provide the possibility to directly deposit the *Pt/C* particles onto the non-conductive membrane.

7.4 Outputs

7.4.1 Publications

[1] Cecil Felix, Ting-Chu Jao, Sivakumar Pasupathi, Bruno G. Pollet, *Optimisation of electrophoretic deposition parameters for gas diffusion electrodes in high temperature polymer electrolyte membrane fuel cells*, Journal of Power Sources 243 (2013) 40-47.

[2] Cecil Felix, Ting-Chu Jao, Sivakumar Pasupathi, Vladimir Linkov, Bruno G. Pollet, *Fabrication of gas diffusion electrodes (GDEs) via electrophoretic deposition for high temperature PEMFCs.*

Journal: Submitted to the Journal of Power Sources.

Manuscript number: POWER-D-13-03176R1

Status: Accepted for publication

[3] C. Felix, A. Yaroshchuk, S. Pasupathi, V.M Linkov, B.G. Pollet, M.P. Bondarenko, V.I. Koval´chuk, E.K. Zholkovskiy, *Electrophoresis and stability of Pt/C nano-catalytic suspensions*.

Intended journal: Advances in Colloid and Interface Science

Status: To be submitted

7.4.2 Conferences

[1] C. Felix, S. Pasupathi, B. G. Pollet, *Gas diffusion electrode development by an electrophoretic deposition technique for high temperature PEMFC applications* (oral presentation), International Hydrogen and Fuel Cell Conference 12-15 July 2013, Napa Valley, California.

[2] C. Felix, S. Pasupathi, V Linkov, B. G. Pollet, *Development of MEAs based on Electrophoretic Deposition (EPD) for HT-PEMFC Applications* (poster), 3rd CARISMA International Conference, 3-5 September 2012, Copenhagen, Denmark.

[3] C. Felix, S. Pasupathi, B. G. Pollet, V. Linkov, *Electrophoretic deposition of Pt/C nanocatalysts onto gas diffusion layers for MEAs in HT-PEMFC applications* (poster), 2nd International Symposium on Electrochemistry , 19-20 July 2012, Cape Town, South Africa.

[4] C. Felix, S. Pasupathi, B. G. Pollet, V. Linkov, *Electrophoretic deposition of Pt/C nanocatalysts onto gas diffusion layers for MEAs in HT-PEMFC applications* (poster), SA-Korea H_2 Fuel Cell Collaboration Workshop, 11-13 July 2012, Rustenburg, South Africa.

150

[5] S. Pasupathi, H. Su, C. Felix, P. Bujlo, T.-C. Jao, B. G. Pollet, *High performance and durable MEAs for HT-PEMFCs.* International Hydrogen and Fuel Cells Conference 2013, 12-15 July 2013, Napa Valley, California.

[6] S. Pasupathi, C. Felix, O. Barron, P. Bujlo, H. Su, B. Pollet, *HT-PEMFC components to systems – An overview of activities at HySA Systems*, 3rd CARISMA International Conference 2012, 3-5 September 2012, Copenhagen, Denmark.

[7] Sivakumar Pasupathi, Xolelwa Ralam, Cecil Felix, Fanapi Nolubabalo, Maiyalagan Thandavarayan, Ben Bladergroen, Vladimir Linkov, *Development of membrane electrode assemblies for high temperature polymer electrolyte fuel cells*, 3rd Wind Power Africa Conference and Renewable Energy exhibition, 8-11 May 2011, Cape Town, South Africa.

151
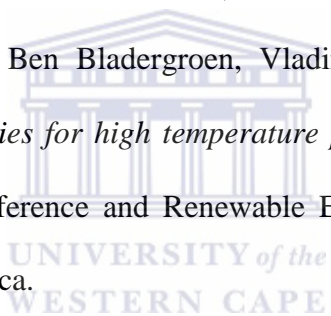
References

1. Wang, J.-T., et al., Electrochimica Acta, 1996. **41** (2): p. 193-197.

2. Zhang, L., et al., Chemical Engineering Journal, 2012. **204-206**: p. 87-97.

3. Das, S.K., Reis, A. and K.J. Berry, K.J., Journal of Power Sources, 2009. **193** (2): p. 691-698.

4. Kerres, J.A., Journal of Membrane Science, 2001. **185**: p. 3-27.

5. Antunes, R.A., et al., International Journal of Hydrogen Energy, 2010. **35** (8): p. 3632-3647.

6. Chan, K.-Y., et al., Journal of Materials Chemistry, 2004. **14** (4): p. 505-516.

7. Zhou, Y., et al., International Journal of Hydrogen Energy, 2013.

8. Divisek, J., et al., Electrochimica Acta, 1998. **43** (24): p. 3811-3815.

9. Echigo, M., et al., Journal of Power Sources, 2004. **132** (1-2): p. 29-35.

10. Krishnan, P., Park, J.-S. and Kim, C.-S., Journal of Power Sources, 2006. **159** (2): p. 817-823.

11. Jiménez, S., et al., Journal of Power Sources, 2005. **151**: p. 69-73.

12. Boaventura, M. and Mendes, A., International Journal of Hydrogen Energy, 2010. **35** (20): p. 11649-11660.

13. Fujigaya, T., Okamoto, M. and Nakashima, N., Carbon, 2009. **47** (14): p. 3227-3232.

14. Andreasen, S.J., Vang, J.R. and Kær, S.K., International Journal of Hydrogen Energy, 2011. **36** (16): p. 9815-9830.

15. Authayanun, S., et al., Applied Energy, 2013. **109**: p. 192-201.

16. Song, Y., et al., Journal of Power Sources, 2005. **141** (2): p. 250-257.

17. Shao, Y., et al., Journal of Power Sources, 2007. **167** (2): p. 235-242.

18. Baschuk, J.J. and Li, X., International Journal of Energy Resources, 2001. **25**: p. 695-713.

19. Li, Q.F., et al., Journal of Electrochemical Society, 2003. **150**: p. A1599-A1605.

20. Zhao, X., et al., International Journal of Hydrogen Energy, 2013. **38** (18): p. 7400-7406.

21. Mehta, V. and Cooper, J.S., Journal of Power Sources, 2003. **114** (1): p. 32-53.

152

22.   Louh, R.-F., et al., International Journal of Hydrogen Energy, 2008. **33** (19): p. 5199-5204.

23.   Wannek, C., Lehnert, W. and Mergel, J., Journal of Power Sources, 2009. **192** (2): p. 258-266.

24.   Li, Q., et al., Progress in Polymer Science, 2009. **34** (5): p. 449-477.

25.   Bonifácio, R.N., et al., Journal of Power Sources, 2011. **196** (10): p. 4680-4685.

26.   Corni, I., Ryan, M.P. and Boccaccini, A.R., Journal of the European Ceramic Society, 2008. **28** (7): p. 1353-1367.

27.   Boccaccini, A.R., et al., Journal of the Ceramic Society of Japan, 2006. **114** (1): p. 1-14.

28.   Chavez-Valdez, A., Shaffer, M.S,P, and Boccaccini, A.R., The Journal of Physical Chemistry B, 2013. **117** (6): p. 1502-1515.

29.   Jeng, K.-T., Huang, W.M. and Hsu, N.-Y., Materials Chemistry and Physics, 2009. **113** (2-3): p. 574-578.

30.   Munakata, H., Ishida, T. and Kanamura, K., Journal of Electrochemical Society, 2007. **154** (12): p. B1368-B1372.

31.   Louh, R.-F., Huang, H. and Tsai, F., Journal of Fuel Cell Science and Technology 2007. **4**: p. 72-78.

32.   Morikawa, H., et al., Journal of the Electrochemical Society 2004. **151**: p. A1733-A1737.

33.   Peighambardoust, S.J., Rowshanzamir, S. and Amjadi, M., International Journal of Hydrogen Energy, 2010. **35** (17): p. 9349-9384.

34.   EG & G Technical Services, I., Fuel Cell Handbook 7th edition, 2004: p. 1-2.

35.   Faghri, A. and Guo, Z.,International Journal of Heat and Mass Transfer, 2005. **48** (19-20): p. 3891-3920.

36.   Kirubakaran, A., Jain, S. and Nema, R.K., Renewable and Sustainable Energy Reviews, 2009. **13** (9): p. 2430-2440.

37.   Ewing, A., Science News, 1966. **89** (16): p. 270-271.

38.   Wang, Y., et al., Applied Energy, 2011. **88** (4): p. 981-1007.

39.   Mekhilef, S., Saidur, R. and Safari, A., Renewable and Sustainable Energy Reviews, 2012. **16** (1): p. 981-989.

40.   Cheng, X., et al., Journal of Power Sources, 2007. **165** (2): p. 739-756.

41. Zaidi, S.M.J., Rahman, S.U. and Zaidi, H.H., Desalination, 2007. **209** (1-3): p. 319-327.

42. Carrette, L., Friedrich, K.A. and Stimming, U., Fuel Cells, 2001. **1** (1): p. 5-39.

43. Appleby, A.J., Energy, 1996. **21** (7/8): p. 521-653.

44. Patil, M.B., et al., Scientific Reviews & Chemical Communications, 2011. **1** (1): p. 25-41.

45. Oono, Y., et al., Journal of Power Sources, 2010. **195** (4): p. 1007-1014.

46. Zhang, J., et al., Journal of Power Sources, 2006. **160** (2): p. 872-891.

47. Savadogo, O., Journal of Power Sources, 2004. **127** (1-2): p. 135-161.

48. Schuster, M.F.H. and Meyer, W.H., Annual Review of Materials Research, 2003. **33** (1): p. 233-261.

49. Korsgaard, A.R., et al., Journal of Power Sources, 2006. **162** (1): p. 239-245.

50. Chutichai, B., et al., Energy, 2013. **55**: p. 98-106.

51. Linares, J.J., et al., International Journal of Hydrogen Energy, 2012. **37** (8): p. 7212-7220.

52. Scott, K., Pilditch, S. and Mamlouk, M., Journal of Applied Electrochemistry, 2007. **37** (11): p. 1245-1259.

53. Li, Q., et al., Chemistry of Materials, 2003. **15**: p. 4896-4915.

54. Scholta, J., et al., Journal of Power Sources, 2009. **190** (1): p. 83-85.

55. Shao, Y., Yin, G. and Gao, Y., Journal of Power Sources, 2007. **171** (2): p. 558-566.

56. Suzuki, A., et al., International Journal of Hydrogen Energy, 2012. **37** (23): p. 18272-18289.

57. Oh, H.-S., Lee, J.H. and Kim, H., International Journal of Hydrogen Energy, 2012. **37** (14): p. 10844-10849.

58. Zhang, J., et al., Journal of Power Sources, 2007. **172** (1): p. 163-171.

59. Kondratenko, M.S., Gallyamov, M.O. and Khokhlov, A.R., International Journal of Hydrogen Energy, 2012. **37** (3): p. 2596-2602.

60. Ong, A.-L., et al., International Journal of Hydrogen Energy, 2010. **35** (15): p. 7866-7873.

61. Choi, S.-W., et al., Polymers, 2013. **5** (1): p. 77-111.

62. Diaz, L.A., Abuin, G.C. and Corti, H.R., Journal of Power Sources, 2009. **188** (1): p. 45-50.

63. Asensio, J.A. and Gomez-Romero, O., Fuel Cells, 2005. **5** (3): p. 336-343.

64. Asensio, J., Journal of Membrane Science, 2004. **241** (1): p. 89-93.

65. Hasiotis, C., Deimede, V. and Kontoyannis, C., Electrochimica Acta, 2001. **46**: p. 2401-2406.

66. Jung, G.-B., et al., International Journal of Hydrogen Energy, 2012. **37** (18): p. 13645-13651.

67. Wannek, C., et al., International Journal of Hydrogen Energy, 2009. **34** (23): p. 9479-9485.

68. de Bruijn, F.A., Dam, V.A.T. and Janssen, G.J.M., Fuel Cells, 2008. **8** (1): p. 3-22.

69. Zheng, H., Petrik, L. and Mathe, M., International Journal of Hydrogen Energy, 2010. **35** (8): p. 3745-3750.

70. Yu, S., et al., Energy Conversion and Management, 2013. **76**: p. 301-306.

71. Reshetenko, T.V., St-Pierre, J. and Rocheleau, R., Journal of Power Sources, 2013. **241**: p. 597-607.

72. Park, S., Lee, J.W. and Popov, B.N., International Journal of Hydrogen Energy, 2012. **37** (7): p. 5850-5865.

73. Biyikoglu, A., International Journal of Hydrogen Energy, 2005. **30** (11): p. 1181-1212.

74. Wang, X., et al., Journal of Power Sources, 2006. **158** (1): p. 154-159.

75. Chen, J., et al., Journal of The Electrochemical Society, 2011. **158** (9): p. B1164.

76. Shen, J., et al., Journal of Power Sources, 2011. **196** (2): p. 674-678.

77. Dhanushkodi, S.R., et al., Journal of Power Sources, 2013. **240**: p. 114-121.

78. Aricò, A.S., et al., Journal of Power Sources, 2008. **178** (2): p. 525-536.

79. Shen, P.K. and Tian, Z., Electrochimica Acta, 2004. **49** (19): p. 3107-3111.

80. Olson, T.S., Chapman, K. and Atanassov, P., Journal of Power Sources, 2008. **183** (2): p. 557-563.

81. Parrondo, J., Mijangos, F. and Rambabu, B., Journal of Power Sources, 2010. **195** (13): p. 3977-3983.

82.   Aindow, T.T., Haug, A.T. and Jayne, D., Journal of Power Sources, 2011. **196** (10): p. 4506-4514.

83.   Lobato, J., et al., Electrochimica Acta, 2007. **52** (12): p. 3910-3920.

84.   Zhai, Y., et al., Journal of Power Sources, 2007. **164** (1): p. 126-133.

85.   Li, X. and Sabir, I., International Journal of Hydrogen Energy, 2005. **30** (4): p. 359-371.

86.   Derieth, T., et al., Journal of New Materials for Electrochemical Systems, 2008. **11**: p. 21-29.

87.   Hung, Y., Tawfik, H. and Mahajan, D., Smart Grid and Renewable Energy, 2013. **4**: p. 43-47

88.   Karimi, S., et al., Advances in Materials Science and Engineering, 2012. p. 1-22.

89.   Park, H.-S., et al., Electrochimica Acta, 2007. **53** (2): p. 763-767.

90.   Holdcroft, S., Chemistry of Materials, 2014. **26** p. 381-393.

91.   Shin, S.-J., et al., Journal of Power Sources, 2002. **106**: p. 146-152.

92.   Huang, D.-C., et al., International Journal of Electrochemical Science, 2011. **6**: p. 2551-2565.

93.   Chun, Y.-G., et al., Journal of Power Sources, 1998. **71**: p. 174 - 178.

94.   Millington, B., Whipple, V. and Pollet, B.G., Journal of Power Sources, 2011. **196** (20): p. 8500-8508.

95.   Song, W., et al., Solid State Ionics, 2010. **181** (8-10): p. 453-458.

96.   Van der Biest, O.O. and Vandeperre, L.J., Annual Review of Materials Science, 1999. **29**: p. 327 - 352.

97.   Litster, S. and McLean, G., Journal of Power Sources, 2004. **130** (1-2): p. 61-76.

98.   Sheng, W., Gasteiger, H.A. and Shao-Horn, Y., Journal of The Electrochemical Society, 2010. **157** (11): p. B1529.

99.   Ramaswamy, N. and Mukerjee, S., Advances in Physical Chemistry, 2012. p. 1-17.

100.   Chandan, A., et al., Journal of Power Sources, 2013. **231**: p. 264-278.

101.   Beyrdbey, B., Corbacioglu, B. and Altin, Z., G.U. Journal of Science, 2009. **22** (4): p. 351-357.

102. Scott, K. and Mamlouk, M., International Journal of Hydrogen Energy, 2009. **34** (22): p. 9195-9202.

103. Neyerlin, K.C., Singh, A. and Chu, D., Journal of Power Sources, 2008. **176** (1): p. 112-117.

104. Kwon, K., et al., Journal of Power Sources, 2009. **188** (2): p. 463-467.

105. Xu, H., Shapiro, I.P. and Xiao, P., Journal of the European Ceramic Society, 2010. **30** (5): p. 1105-1114.

106. Fazio, S., et al., Journal of the European Ceramic Society, 2008. **28** (11): p. 2171-2176.

107. Besra, L. and Liu, M., Progress in Materials Science, 2007. **52** (1): p. 1-61.

108. Hackley, V.A., et al., Colloids and Surfaces A: Physicochemical and Engineering Aspects, 1995. **98**: p. 209-224.

109. Ma, J., Wang, C. and Liang, C.H., Materials Science and Engineering: C, 2007. **27** (4): p. 886-889.

110. Ofir, E., Oren, Y. and Adin, A., Desalination, 2007. **204** (1-3): p. 33-38.

111. Singh, B.P., et al., Journal of Colloid and Interface Science, 2005. **291** (1): p. 181-186.

112. Sakka, Y. and Uchikoshi, T., KONA Powder and Particle Journal, 2010. **28**: p. 74-90.

113. Sarkar, P. and Nicholson, P.S., Journal of American Ceramic Society, 1996. **79** (8): p. 1987 - 2002.

114. Ammam, M., RSC Advances, 2012. **2** (20): p. 7633.

115. Ouedraogo, B. and Savadogo, O., Journal of Scientific Research & Reports, 2013. **2** (1): p. 190-205.

116. Radice, S., et al., Journal of the European Ceramic Society, 2010. **30** (5): p. 1079-1088.

117. Hosomi, T., Matsuda, M. and Miyake, M., Journal of the European Ceramic Society, 2007. **27** (1): p. 173-178.

118. Yamaji, K., et al., Fuel Cells Bulletin, 2004. **2004** (12): p. 12-15.

119. Talebi, T., et al., International Journal of Hydrogen Energy, 2010. **35** (17): p. 9405-9410.

120. Cherng, J.S., Sau, J.R. and Chung, C.C., Journal of Solid State Electrochemistry, 2007. **12** (7-8): p. 925-933.

121. Besra, L., Compson, C. and Liu, M., Journal of Power Sources, 2007. **173** (1): p. 130-136.

122. Basu, R.N., Randall, C.A. and Mayo, M.J., Journal of American Ceramic Society, 2001. **84** (1): p. 33-40.

123. Hsu, Y.-K., et al., Diamond and Related Materials, 2009. **18** (2-3): p. 557-562.

124. Sarkar, A. and Daniels-Race, T., Nanomaterials, 2013. **3** (2): p. 272-288.

125. Ithurbide, A., et al., Thin Solid Films, 2010. **518** (10): p. 2644-2648.

126. Abdullah, H.Z. and Sorrell, C.C., Journal of the Australian Ceramic Society Volume 2008. **44** (2): p. 12-16.

127. Fukada, Y., et al., Journal of Materials Science, 2004. **39**: p. 787-801.

128. Nicholson, P.S., Sarkar, P. and Haung, X., Journal of Material Science, 1993. **28**: p. 6274-6278.

129. Ferrari, B. and Moreno, R., Journal of the European Ceramic Society, 2010. **30** (5): p. 1069-1078.

130. Fraczek-Szczypta, A., et al., Journal of Molecular Structure, 2013. **1040**: p. 238-245.

131. Baldisserri, C., Gardini, D. and Galassi, C., Journal of Colloid and Interface Science, 2010. **347** (1): p. 102-111.

132. Ferrari, B. and Moreno, R., Journal of the European Ceramic Society, 1997. **17:** p. 549-556.

133. Cihlar, J., et al., Journal of the European Ceramic Society, 2013. **33** (10): p. 1885-1892.

134. Van Tassel, J.J. and Randall, C.A., Key Engineering Materials, 2006. **314**: p. 167-174.

135. Joung, Y.S. and Buie, C.R., Langmuir, 2011. **27** (7): p. 4156-4163.

136. Lau, K.-T. and Sorrell, C.C., Materials Science and Engineering: B, 2011. **176** (5): p. 369-381.

137. Lo'pez-Garcia, J.J., Grosse, C. and Horno, J., Journal of Physical Chemistry B, 2007. **111**: p. 8985-8992.

138. Aranda-Rascón, M.J., et al., Journal of Colloid and Interface Science, 2009. **335** (2): p. 250-256.

139. Zukoski, C.F. and Saville, D.A., Journal of Colloid and Interface Science, 1985. **107**: p. 322-333.

140. Dhukin, S.S., Zimmermann, R. and Werner, C., Colloids and Surfaces A: Physicochemical and Engineering Aspects, 2001. **195**: p. 103-112.

141. Dukhin, S.S., Advances in Colloid and Interface Science, 1995. **61**: p. 17-49.

142. Wells-Gray, E.M., Kirkpatrick, S.J. and Sakaguchi, R.L., Dental Materials, 2010. **26** (7): p. 634-642.

143. Brenner, T., Johannsson, R. and Nicolai, T., Food Hydrocolloids, 2009. **23** (2): p. 296-305.

144. Bard, A.J. and Faulkner, L.R., Electrochemical Methods: Fundamentals and Applications 2nd Edition. 2001: p. 239.

145. Monk, P., Fundamentals of Electro-analytical Chemistry 2001: p. 156.

146. Curnick, O.J., Pollet, B.G. and Mendes, P.M., RSC Advances, 2012. **2** (22): p. 8368.

147. Du, S., Millington, B. and Pollet, B.G., International Journal of Hydrogen Energy, 2011. **36** (7): p. 4386-4393.

148. Lee, J.-H., et al., Journal of Physical Chemistry C, 2007. **111**: p. 2477-2483

149. Ye, X., et al., Physical Review E, 1996. **54** (6).

150. Fritz, G., et al., Langmuir, 2002. **18**: p. 6381-6390.

151. Thanasilp, S. and Hunsom, M., Fuel, 2010. **89** (12): p. 3847-3852.

152. Wicks, Z.W., et al., Organic Coatings Science and Technology 3rd Edition. 2007: p. 541.

153. Huang, T.-H., et al., International Journal of Hydrogen Energy, 2012. **37** (18): p. 13872-13879.

154. Yuan, X., et al., International Journal of Hydrogen Energy 2007. **32**: p. 4365-4380.

155. Park, S., Lee, J.W. and Popov, B.N., Journal of Power Sources, 2008. **177** (2): p. 457-463.

156. Li, A., et al., Electrochimica Acta, 2010. **55** (8): p. 2706-2711.

157. Boccaccini, A.R., et al., Carbon, 2006. **44** (15): p. 3149-3160.

158. Ali, S.T., et al., International Journal of Hydrogen Energy, 2011. **36** (2): p. 1628-1636.

159. Li, M. and Scott, K., Electrochimica Acta, 2010. **55** (6): p. 2123-2128.

160. Yang, C., Journal of Membrane Science, 2004. **237** (1-2): p. 145-161.

161. Jao, T.-C., et al., Journal of Power Sources, 2011. **196** (4): p. 1818-1825.

162. Yaseen, H., Baltianski, S. and Tsur, Y., Journal of Materials Science, 2007. **42** (23): p. 9679-9683.

163. Workie, B., McCandless, B.E. and Gebeyehu, Z., Journal of Chemistry, 2013. **2013**: p. 1-7.

164. Derjaguin, B.V., Churaev, N.V. and Muller, V.M., Plenum Press: Consultants Bureau, New York,, 1987: p. 440.

165. Israelachvili, J.N., London: Academic Press, 1992: p. 450.

166. Cosgrove, T., Oxford: Blackwell, 2005: p. 304.

167. Derjaguin, B.V. and Landau, L., Acta Physico Chemica URSS, 1941. **14** (6): p. 632-662.

168. Verwey, E.J.W. and Overbeek, J.T.G., Amsterdam: Elsevier, 1948: p. 205.

169. Smoluchowski, M., Hundbuch der Eletrizitat und des Magnetismus, 1914. **2**: p. 366.

170. Von Smoluchowski, M.Z., Physical Chemistry, 1918. **92**: p. 129.

171. Henry, D.C., Proceedings of the Royal Society A, 1931. **133** (821): p. 106-129.

172. Lyklema, J., Fundamentals of Interface and Colloid Science, 1995. **2**: p. 3.208.

173. Debye, P.J.W. and Hückel, E., Physikalische Zeitschrift, 1923. **24** (9): p. 185-206.

174. Rutgers, A.J. and Overbeek, J.T.G., Zeitschrift für Physikalische Chemie, A, 1936. **177**: p. 29.

175. Overbeek, J.T.G., Kolloidchemie Beihefte, 1943. **54**: p. 287.

176. Overbeek, J.T.G., Philips Research Reports, 1946. **1**: p. 315.

177. Booth, F., Proceedings of the Royal Society A, 1950. **203**: p. 514.

178. Wiersema, P.H., Loeb, A.L. and Overbeek, J.T.G., Journal of Colloid and Interface Science, 1966. **22**: p. 78.

179. Dukhin, S.S. and Derjaguin, B.V., Surface and Colloid Science, Matijevic, E., (Ed.), John Willey & Sons, New York, 1974.

180. Semenikhin, N.M. and Dukhin, S.S., Colloid Journal of the USSR, (English translation), 1975. **37**: p. 1013.

181. O'Brien, R.W. and White, L.R., Journal of the Chemical Society, Faraday Transactions 2, 1978. **74**: p. 1607.

182. Ohshima, H.J., Healy, T.W. and White, L.R., Journal of the Chemical Society, Faraday Transactions 2, 1983. **79**: p. 1613.

183. Borkovskaya, Y.B., Zharkikh, N.I. and Shilov, V.N., Colloid Journal of the USSR, (English translation), 1983. **45**: p. 1072.

184. Ohshima, H.J., et al., Journal of the Chemical Society, Faraday Transactions 2, 1984. **80**: p. 1299.

185. Shilov, V.N., Zharkikh, N.I. and Borkovskaya, Y.B., Colloid Journal of the USSR, (English translation), 1985. **47**: p. 645.

186. Shilov, V.N., Zharkikh, N.I. and Borkovskaya, Y.B., Colloid Journal of the USSR, (English translation), 1985. **47**: p. 795.

187. Zholkovskij, E.K., et al., Advances in Colloid Interface Science, 2007. **134 - 135** p. 279.

188. Zholkovskij, E.K., et al., Canadian Journal of Chemical Engineering 2007. **85**: p. 701.

189. Carnie, S.L., Chan, D.Y.C. and Stankovich, J., Journal of Colloid and Interface Science, 1994. **165**: p. 116.

190. Parsegian, V.A., Van der Waals Forces, Cambridge University Press: New York, 2006.